

## REPORT DOCUMENTATION PAGE

AFRL-SR-AR-TR-02-

Public reporting burden for this collection of information is estimated to average 1 hour per response, including and maintaining the data needed, and completing and reviewing the collection of information. Send comments, information, including suggestions for reducing this burden, to Washington Headquarters Services, Directorate, 1204, Arlington, VA 22202-4302, and to the Office of Management and Budget, Paperwork Reduction Project (0704-0188), Washington, DC 20503.

gathering  
ection of  
ay, Suite

Q382

1. AGENCY USE ONLY (Leave blank)		2. REPORT DATE	3. REPORT TYPE AND DATES COVERED
		September 30, 2002	Final Report (01 APR 00 to 30 JUN 02)
4. TITLE AND SUBTITLE		5. FUNDING NUMBERS	
Computational Issues in Analysis and Design of Chemical-Laser Flow-Fields		F49620-00-C-0011	
6. AUTHOR(S)		8. PERFORMING ORGANIZATION REPORT NUMBER	
W. Marc Eppard and Eugene M. Cliff			
7. PERFORMING ORGANIZATION NAME(S) AND ADDRESS(ES)		9. SPONSORING/MONITORING AGENCY NAME(S) AND ADDRESS(ES)	
AeroSoft, Inc. 1872 Pratt Drive Suite 1275 Blacksburg, VA 24060-6363		AFOSR Air Force Office of Scientific Research Attn: Major William Hilbun 801 North Randolph Street, Room 732 Arlington, VA 22203-1977	
10. SPONSORING/MONITORING AGENCY REPORT NUMBER		0002AD	
11. SUPPLEMENTARY NOTES		Software Data Restricted	
12a. DISTRIBUTION AVAILABILITY STATEMENT		12b. DISTRIBUTION CODE	
Approved for public release, distribution unlimited			
13. ABSTRACT (Maximum 200 words)		In support of the Air Force's airborne laser (ABL) development program, state-of-the-art CFD analysis and design methods have been extended to include the physical models important in chemical oxygen-iodine laser (COIL) systems. The three-dimensional COIL simulation model is based on the CFD flow solver GASP v4 which solves the conservative, finite-volume formulation of the Navier-Stokes equations with general thermo-chemistry. The COIL design software is based on the continuous sensitivity equation method (CSEM) and AeroSoft's flow-field sensitivity solver, SENSE. Extensions to GASP and SENSE include a COIL chemistry mechanism, a multicomponent diffusion model with pressure terms, and coupling with a laser optics resonator module based on the geometric ray-tracing method. In addition, GASP has been modified to include a water-vapor condensation model and a COIL surface catalysis model. Simulations have been performed for the RADICL research laser for both power-on and power-off conditions.	
14. SUBJECT TERMS		15. NUMBER OF PAGES	
		65	
17. SECURITY CLASSIFICATION OF REPORT		18. SECURITY CLASSIFICATION OF THIS PAGE	
19. SECURITY CLASSIFICATION OF ABSTRACT		20. LIMITATION OF ABSTRACT	

Computational Issues in Analysis and Design  
of  
Chemical-Laser Flow-Fields

A Final Report Submitted to the  
Air Force Office of Scientific Research

Principal Investigator:

*W. M. Eppard*  
*AeroSoft, Inc.*  
*1872 Pratt Drive, Ste. 1275*  
*Blacksburg, VA 24060*  
*(540) 557-1900*  
*(540) 557-1919 FAX*  
*eppard@aerosft.com*

and

*E. M. Cliff*  
*Interdisciplinary Center for Applied Mathematics*  
*Virginia Tech*  
*Blacksburg, VA 24061*

20021122 128

## 1 Introduction

Chemical lasers represent an important component in many advanced weapons systems of interest to the Air Force, *e.g.*, the airborne laser program (ABL). The chemical oxygen-iodine laser, or COIL, is a short wavelength, high-power chemical laser that operates on an atomic iodine laser transition. COIL was invented in 1977 at the Air Force Weapons Laboratory, now a part of the Air Force Research Laboratory at Kirtland Air Force Base, New Mexico. AFRL/DE continues to develop COIL technology using as a primary test apparatus the 10 kilowatt-class device called RADICL (Research and Development Iodine Chemical Laser)

Research and development programs for COIL typically employ numerical analysis techniques such as computational fluid dynamics (CFD) to provide insight into laser performance and design. A common goal shared by these programs is the need to more thoroughly understand the underlying physical processes of chemical lasers so that performance may be optimized. Enhanced CFD analysis tools can play an essential role in this regard. High-resolution CFD simulations can aid in interpreting and explaining measured data, make predictions for operating conditions beyond the test database, and provide accurate estimates of laser power output. Beyond predicting the performance of a given laser configuration, new design tools are required to aid scientists in tuning, scaling and shaping a practical system. AeroSoft's research and development program has focused on the following three goals:

- 1. To develop accurate and efficient CFD analysis tools for modeling COIL lasers.**  
State-of-the-art CFD methods have been extended to include new capabilities and physical models important in COIL-type laser systems such as the RADICL.
- 2. To develop high-level software tools tailored for the design and optimization of COIL lasers.**  
The continuous sensitivity equation method (CSEM) for CFD-based design has been extended to include new capabilities and physical models important in COIL-type laser systems.
- 3. To develop a framework for coupling discipline-specific sensitivity analyses.**  
Work specific to this contract has led to new sensitivity-analysis tools for the coupled fluid-dynamic/power-extraction systems in COIL-laser designs.

The Phase-II COIL effort has focused on extending AeroSoft's GASP and SENSE software for COIL lasers. GASP is a multi-zone, upwind, characteristic-based code, which solves the integral form of the Reynolds-Averaged Navier-Stokes equations. GASP models the fluid continuum with a finite number of control volumes and incorporates general thermo-chemistry modeling with an extensive thermo-chemical database. The latest version, GASP v4, has more efficient time-integration schemes including implicit treatment of zonal boundaries. GASP v4 uses a distributed-memory parallel architecture in order to exploit a wide variety of platforms. These schemes greatly improve the efficiency of the code, reducing the amount of time needed to perform a computation. AeroSoft's SENSE software is based on the continuous sensitivity equation method and provides flow-field sensitivities to a wide array of flow and geometric design variables. SENSE is available as a commercial package and has been used in a variety of applications of aerospace interest [5, 6].

The initial modeling effort included modifications to GASP's thermo-chemical database, improvements to the species diffusion model, and modifications to account for laser power extraction. The thermo-chemical database manager has been modified to allow chemical species to be present at multiple energy states, *e.g.*,  $I(^2P_{1/2})$  and  $I(^2P_{3/2})$ ; a feature characteristic of COIL chemistry models. A 20-reaction, 10-species COIL chemistry model has also been added to the thermo-chemical database. The species diffusion model in GASP v4 has been extended to account for effective diffusion coefficients as well as the pressure-driven diffusion effects that are important in COIL lasers. The diffusion models have been tested for injection problems involving helium and iodine at conditions similar to the RADICL injector. Software modifications have also been made to GASP v4 to account for laser power extraction in the optical cavity. This task involved adding lasing source terms to the iodine species continuity equations and the global energy equation, implementing a geometric optics resonator model, and including conservative interpolation methods between the flow-solver grid and the optics grid. Power-On results have been obtained for the RADICL device.

Numerical studies [10] have shown that water-vapor condensation in the COIL configuration may have a significant impact on power output. A homogeneous water-vapor condensation model similar to that described in Ref [10] has been developed and implemented into GASP v4, and results have been obtained for the RADICL device. Wall catalysis effects also reduce COIL efficiency, as excited species contact the nozzle wall and become deactivated. A wall catalysis model similar to that described in Ref [8] has been developed and implemented into GASP v4. The model includes wall deactivation and recombination reactions and is consistent with both the 10-specie COIL chemistry model and the effective diffusion model. Results with wall catalysis effects have been obtained for the RADICL system.

Work toward the second goal, *i.e.*, (2) above, has focused on extending the capability of SENSE to include models important for COIL systems. Modeling enhancements to SENSE include the addition of the COIL chemistry model, the multicomponent diffusion model, LeRC thermodynamic curve fits, and modules to compute the gain and gain sensitivity. The capability to compute flow sensitivities to Arrhenius reaction rates has also been implemented into SENSE. A sensitivity analysis module has also been developed for the laser optics resonator and is based on differentiation of the geometric ray-tracing algorithm.

Work toward the third goal, *i.e.*, (3) above, has been focused on developing the software to couple the flow-field sensitivity module, SENSE, and the laser optics resonator sensitivity module. Numerical studies indicate that a Gauss-Seidel blocking of the sensitivity equations permits the re-use of single-discipline sensitivity procedures in such problems with multi-disciplinary physics. The COIL sensitivity package has been tested on simple geometries, for both cold flow and flow with the laser on.

## 2 Modifications to the Thermo-Chemical Database

The COIL laser operates on the  $^2(P_{1/2}) \rightarrow ^2(P_{3/2})$  transition between the spin orbit components of atomic iodine. This transition is “pumped” through energy transfer from the excited  $O_2(^1\Delta)$  state of molecular oxygen. Continuous wave operation is achieved by injecting molecular iodine into a primary flow containing the excited states,  $O_2(^1\Delta)$  and  $O_2(^1\Sigma)$ , and the ground state,  $O_2(^3\Sigma)$ , of molecular oxygen. Once the molecular iodine has been injected into the flow, energy pooling processes involving the excited states of oxygen result in the dissociation of molecular iodine,  $I_2$ , into atoms. This is followed by rapid energy transfer and the establishment of a population inversion in atomic iodine according to the “pumping” reaction



and the various competing mechanisms that work to reduce  $I^*$ . Note that in Eq (1)  $I$  and  $I^*$  denote the  $^2(P_{3/2})$  and  $^2(P_{1/2})$  states of atomic iodine respectively. During the lasing process, it is the excited  $I^*$  state of iodine that is stimulated to emit photons, while the energy in this system is stored in the  $O_2(^1\Delta)$  state. Because of the relatively large concentration of  $O_2(^1\Delta)$ , each iodine atom can be repumped and cycled many times before leaving the lasing cavity.

No.	Reaction	Mechanism	$K_f (Kg - mole, m^3, s)$
1	$O_2(^1\Delta) + O_2(^1\Delta) \rightarrow O_2(^1\Sigma) + O_2(^3\Sigma)$	$I_2$ Dissociation (+ $O_2(^1\Sigma)$ )	$1.626 \times 10^4$
2	$O_2(^1\Sigma) + H_2O \rightarrow O_2(^1\Delta) + H_2O$	$I_2$ Dissociation (- $O_2(^1\Sigma)$ )	$4.035 \times 10^9$
3	$O_2(^1\Delta) + O_2(^3\Sigma) \rightarrow O_2(^3\Sigma) + O_2(^3\Sigma)$	Competing (- $O_2(^1\Delta)$ )	$9.635 \times 10^2$
4	$O_2(^1\Delta) + H_2O \rightarrow O_2(^3\Sigma) + H_2O$	Competing (- $O_2(^1\Delta)$ )	$2.409 \times 10^3$
5	$O_2(^1\Delta) + Cl_2 \rightarrow O_2(^3\Sigma) + Cl_2$	Competing (- $O_2(^1\Delta)$ )	$3.613 \times 10^3$
6	$O_2(^1\Delta) + He \rightarrow O_2(^3\Sigma) + He$	Competing (- $O_2(^1\Delta)$ )	$4.818 \times 10^0$
7	$I_2 + O_2(^1\Sigma) \rightarrow 2I + O_2(^3\Sigma)$	$I_2$ Dissociation (+ $I$ )	$2.409 \times 10^9$
8	$I_2 + O_2(^1\Sigma) \rightarrow I_2 + O_2(^3\Sigma)$	$I_2$ Dissociation (- $O_2(^1\Sigma)$ )	$9.635 \times 10^9$
9	$I_2 + O_2(^1\Delta) \rightarrow I_2^* + O_2(^3\Sigma)$	$I_2$ Dissociation (+ $I_2^*$ )	$4.215 \times 10^6$
10	$I_2 + I^* \rightarrow I_2^* + I$	Competing (- $I^*$ )	$2.288 \times 10^{10}$
11	$I_2^* + O_2(^1\Delta) \rightarrow 2I + O_2(^3\Sigma)$	$I_2$ Dissociation (+ $I$ )	$1.807 \times 10^{11}$
12	$I_2^* + O_2(^3\Sigma) \rightarrow I_2 + O_2(^3\Sigma)$	$I_2$ Dissociation (- $I_2^*$ )	$3.011 \times 10^{10}$
13	$I_2^* + H_2O \rightarrow I_2 + H_2O$	$I_2$ Dissociation (- $I_2^*$ )	$1.807 \times 10^{11}$
14	$I_2^* + He \rightarrow I_2 + He$	$I_2$ Dissociation (- $I_2^*$ )	$2.409 \times 10^9$
15	$I + O_2(^1\Delta) \rightarrow I^* + O_2(^3\Sigma)$	Pumping (+ $I^*$ )	$4.697 \times 10^{10}$
16	$I + O_2(^1\Delta) \rightarrow I + O_2(^3\Sigma)$	Competing (- $O_2(^1\Delta)$ )	$6.022 \times 10^5$
17	$I^* + O_2(^1\Delta) \rightarrow I + O_2(^1\Sigma)$	Competing (- $I^*$ )	$6.022 \times 10^7$
18	$I^* + O_2(^1\Delta) \rightarrow I + O_2(^1\Delta)$	Competing (- $I^*$ )	$6.624 \times 10^7$
19	$I^* + I \rightarrow 2I$	Competing (- $I^*$ )	$9.635 \times 10^6$
20	$I^* + H_2O \rightarrow I + H_2O$	Competing (- $I^*$ )	$1.204 \times 10^9$

Table 1: 10-specie, 20-reaction COIL chemistry model

Species	Database Name
$O_2(^3\Sigma)$	0_2
$O_2(^1\Delta)$	(0_2)_-[sd]
$O_2(^1\Sigma)$	(0_2)_-[ss]
$I_2$	I_2
$I_2^*$	(I_2)_-[star]
$I(^2P_{3/2})$	I
$I(^2P_{1/2})$	(I)_-[star]

Table 2: Thermo-chemical database species naming convention.

During this Phase-I effort the COIL chemistry model in Table 1 has been added to GASP's thermo-chemical database. The  $I_2$  dissociation mechanism consists of the two separate reaction paths described by reactions 7 and 11. Reactions 1, 2, 8, 9, and 12 – 14 affect the  $I_2$  dissociation process through the production (or destruction) of  $O_2(^1\Sigma)$  and  $I_2^*$ . Reaction 15 is the pumping reaction, and reactions 3 – 6, 10, and 16 – 20 work to deactivate the system by reducing either  $O_2(^1\Delta)$  or  $I^*$ . The forward reaction rates for each reaction are constant and given in Table 1. The backward rates are computed using the forward rates and the equilibrium constant which is determined through the LeRC curve fits and the minimization of Gibb's free energy.

As indicated in the above discussion, the COIL chemistry mechanism is used (in part) to model transitions in the internal energy states of the oxygen and iodine species. As a result, the various energy states of a given molecule or atom must be represented as a separate species in the thermo-chemical database. To accommodate this feature, a tagging convention has been added to the thermo-chemical database manager which allows a chemical species to be present at multiple energy states. The various energy levels of oxygen and iodine have been entered into the database as shown in Table 2. Figures 1 and 2 illustrate the new naming convention as shown in the species and model windows of the database manager for the COIL mechanism.

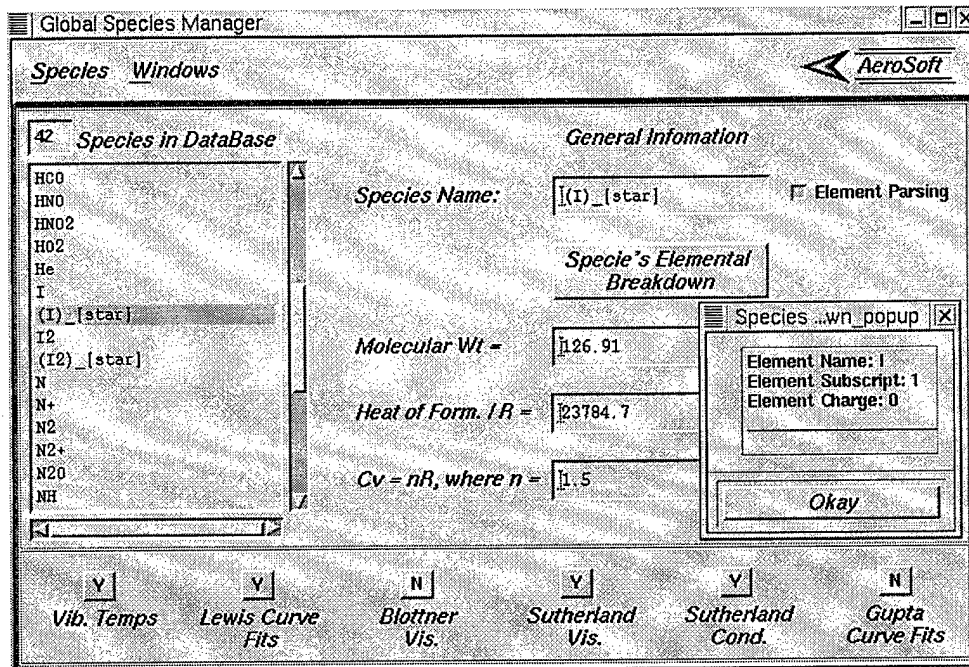


Figure 1: Species window illustrating new species naming convention and species parsing

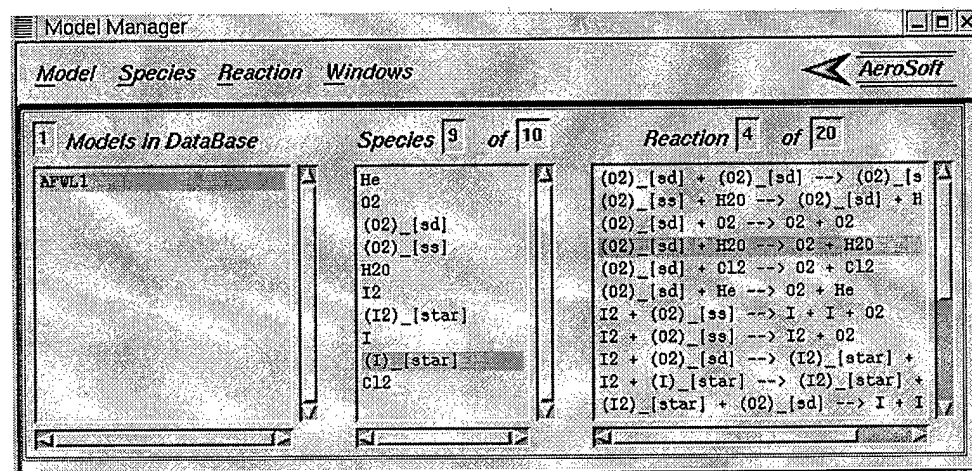


Figure 2: Model window illustrating the new COIL chemistry model

### 3 Effective Diffusion Model

Pressure diffusion terms have been shown to be important in the injector region of the COIL where a 2:1 or greater pressure ratio must exist for sonic injection to be achieved. During Phase-I an effective diffusion model with pressure-gradient terms has been added to the viscous formulation in GASP v4. The diffusion terms appear in the species continuity equations as well as the global energy equation. The continuity equation for species  $s$  is given by

$$\frac{\partial}{\partial t} \iiint \rho_s dV + \oint_A (\rho_s \mathbf{V} \cdot \hat{\mathbf{n}}) dA = \oint_A (-\rho_s \vec{V}_s \cdot \hat{\mathbf{n}}) dA + \iiint \omega_s dV. \quad (2)$$

where  $\rho_s$  is the density of species  $s$ ,  $\mathbf{V}$  is the velocity vector,  $\omega_s$  represents the chemistry production term for species  $s$ , and  $\vec{V}_s$  is the diffusion velocity vector for species  $s$ . Prior to this contract the species diffusion velocity was given by Fick's law

$$\rho_s \vec{V}_s = -\rho D_s \nabla(\rho_s / \rho), \quad (3)$$

with a species diffusion coefficient determined using a constant Schmidt number as

$$D_s = \frac{\mu}{\rho Sc}. \quad (4)$$

The effective diffusion model represents a modeling improvement in that it accounts for individual species diffusion coefficients as well as pressure-driven diffusion effects. The effective diffusion model for species  $s$  is given by

$$\rho_s \vec{V}_s = -\gamma_t \hat{M}_s D_{sm} \left[ \bar{\nabla} \chi_s + \left( \chi_s - \frac{\rho_s}{\rho} \right) \frac{\bar{\nabla} p}{p} \right] + \gamma_t \frac{\rho_s}{\rho} \sum_{j=1}^N \hat{M}_j D_{jm} \left[ \bar{\nabla} \chi_j + \left( \chi_j - \frac{\rho_j}{\rho} \right) \frac{\bar{\nabla} p}{p} \right], \quad (5)$$

where  $\hat{M}_s$  is the species molecular weight,  $D_{sm}$  is the species effective diffusion coefficient,  $\gamma_t$  is the mixture concentration, and  $\chi_s$  is the species mole fraction. Definitions for the species concentration,  $\gamma_s$ , the mixture concentration, and the species mole fraction are given respectively as

$$\gamma_s = \frac{\rho_s}{\hat{M}_s}, \quad \gamma_t = \sum_{s=1}^N \gamma_s, \quad \chi_s = \frac{\gamma_s}{\gamma_t}. \quad (6)$$

The species effective diffusion coefficients are given in terms of a mixture summation of the binary diffusion coefficients,  $\mathcal{D}_{ij}$ , as follows

$$D_{sm} = \frac{1 - \chi_s}{\sum_{j=1, j \neq s}^N \chi_j / \mathcal{D}_{sj}}, \quad (7)$$

and satisfy the mass conservation constraint that

$$\sum_{s=1}^N \rho_s \vec{V}_s = 0. \quad (8)$$

Closure of this system of equations requires relations for the binary diffusion coefficients,  $\mathcal{D}_{ij}$ , which have been determined by Hirschfelder [7] using appropriate collision integrals. The resulting equations are

$$\mathcal{D}_{ij} = 0.018828 T^{3/2} \frac{\sqrt{\left( \frac{1}{\hat{M}_i} + \frac{1}{\hat{M}_j} \right)}}{p \sigma_{ij}^2 \Omega_{ij}}, \quad (9)$$

where

$$\sigma_{ij} = \frac{\sigma_i + \sigma_j}{2}, \quad (10)$$

$$\Omega_{ij} = \left[ \frac{0.75571}{T^{*0.08742}} + \frac{0.68191}{T^{*0.84910}} \right], \quad (11)$$

$$T^* = \frac{T}{\epsilon_{ij}}, \quad (12)$$

and

$$\epsilon_{ij} = \sqrt{\epsilon_i \epsilon_j}. \quad (13)$$

Actual implementation of the effective diffusion model has been performed by separating the effects of mole-fraction gradients and pressure gradients. This feature allows the option to run with or without the pressure diffusion terms. Separating these effects in Eq (5) yields

$$\rho_s \vec{\mathcal{V}}_s^\chi = -\gamma_t \hat{M}_s D_{sm} \bar{\nabla} \chi_s + \gamma_t \frac{\rho_s}{\rho} \sum_{j=1}^N \hat{M}_j D_{jm} \bar{\nabla} \chi_j, \quad (14)$$

and

$$\rho_s \vec{\mathcal{V}}_s^p = -\gamma_t \hat{M}_s D_{sm} \left( \chi_s - \frac{\rho_s}{\rho} \right) \frac{\bar{\nabla} p}{p} + \gamma_t \frac{\rho_s}{\rho} \sum_{j=1}^N \hat{M}_j D_{jm} \left( \chi_j - \frac{\rho_j}{\rho} \right) \frac{\bar{\nabla} p}{p}, \quad (15)$$

such that

$$\rho_s \vec{\mathcal{V}}_s = \rho_s \vec{\mathcal{V}}_s^\chi + \rho_s \vec{\mathcal{V}}_s^p. \quad (16)$$

Also to facilitate ease of implementation, the following variables have been defined

$$\mathbf{G}_s^\chi \equiv \hat{M}_s D_{sm} \bar{\nabla} \chi_s, \quad (17)$$

and

$$\mathbf{G}_s^p \equiv \hat{M}_s D_{sm} \left( \chi_s - \frac{\rho_s}{\rho} \right). \quad (18)$$

Utilizing these definitions, Eqs (14) and (15) become

$$\rho_s \vec{\mathcal{V}}_s^\chi = -\gamma_t \left[ \mathbf{G}_s^\chi - \frac{\rho_s}{\rho} \sum_{j=1}^N \mathbf{G}_j^\chi \right], \quad (19)$$

and

$$\rho_s \vec{\mathcal{V}}_s^p = -\gamma_t \left[ \mathbf{G}_s^p - \frac{\rho_s}{\rho} \sum_{j=1}^N \mathbf{G}_j^p \right] \frac{\bar{\nabla} p}{p}. \quad (20)$$

The diffusion term resulting from mole-fraction gradients, Eq (19), behaves in a similar fashion to Fick's law and results in molecular diffusion away from mole-fraction gradients. The pressure diffusion term, Eq (20), results in molecular diffusion of "lighter" species away from pressure gradients and "heavier" species toward pressure gradients. To see this we consider a mixture of helium and iodine with molecular weights  $\hat{M}_{He} = 4.003$  and  $\hat{M}_{I_2} = 253.82$  respectively. The species densities, pressure and temperature are taken as  $\rho_{He} = 0.010395 \text{ Kg/m}^3$ ,  $\rho_{I_2} = 0.007605 \text{ Kg/m}^3$ ,  $p = 9576 \text{ N/m}^2$  and  $T = 438.5 \text{ K}$ . These conditions results in mass fractions of  $\rho_{He}/\rho = 0.5775$  and  $\rho_{I_2}/\rho = 0.4225$  and mole fractions of  $\chi_{He} = 0.988564$  and of  $\chi_{I_2} = 0.011406$ . Note that the term  $(\chi_s - \rho_s/\rho)$  in Eq (18) will be positive for a species whose mole fraction is greater than its mass fraction, indicating a relatively "light" species. This same term will be negative for a species whose

mole fraction is less than its mass fraction, indicating a relatively “heavy” species. Evaluating the terms in Eq (20) for the specified conditions yields

$$\rho_{He} \vec{V}_{He}^p = -1.2456 \times 10^{-4} \frac{\bar{\nabla} p}{p}, \quad (21)$$

and

$$\rho_{I_2} \vec{V}_{I_2}^p = +1.2456 \times 10^{-4} \frac{\bar{\nabla} p}{p}. \quad (22)$$

These results show that the lighter helium molecules diffuse in a direction opposite the pressure-gradient vector, while the heavier iodine molecules diffuse in the same direction as the pressure-gradient vector. The net effect is for light and heavy particles to tend to separate in regions of large pressure gradients.

### 3.1 Helium-Iodine Injection into an Infinite Chamber

As a first test problem for the new diffusion model, we considered the two-dimensional, supersonic injection of helium and iodine into an infinite chamber. Figure 3(a) shows the  $81 \times 161$  computational mesh used for this case. The injector face extends from  $y = 0.0 m$  to  $y = \pm 0.0005 m$  with flow entering the domain from left to right. Solid chamber walls extend above and below the injector face. Grid points are clustered in the horizontal direction near the wall and injector face and in the vertical direction near the injector side walls. The jet Mach number was  $M = 1.3$ , the temperature was  $T = 288 K$ , and the pressure was  $p = 28728 N/m^2$ . The species densities were  $\rho_{He} = 0.047480 Kg/m^3$  and  $\rho_{I_2} = 0.034737 Kg/m^3$ . Initial conditions in the chamber consisted of pure helium at Mach number of  $M = 0.01$ , a temperature of  $T = 300 K$ , and a pressure of  $p = 9576 N/m^2$ . The initial species density for helium was  $\rho_{He} = 0.015368 Kg/m^3$ . The jet conditions were imposed using a split-flux free-stream boundary condition and the chamber wall was treated using a no-slip wall boundary condition. All other boundaries were treated using first-order extrapolation from the interior.

Figures 3(b), 3(c), and 3(d) show the resulting Mach number contours partially superimposed with streamtraces, pressure contours, and iodine mass fraction contours. Figures 3(b) and 3(c) indicate that the helium-iodine mixture undergoes a strong expansion as it leaves the injector, resulting in the lower pressures and higher Mach numbers shown by the contours plots. The very strong pressure gradients near the injector side walls, *i.e.*,  $y = \pm 0.0005 m$ , result in large pressure-diffusion effects which work to separate the helium from the iodine. This can be seen in Fig 3(d), where the iodine concentrations in the near-wall region are essentially zero. Comparison of the streamlines in Fig 3(b) and the iodine mass fraction contours in Fig 3(d) indicate that the diffusion process occurs in a direction transverse to the mean flow velocity. Figure 4 shows the normalized pressure profile and helium and iodine mass-fraction profiles for the vertical,  $i = 10$  grid line. This grid line is very close in proximity to the injector face and chamber walls. The normalized pressure profile shows a large pressure gradient at  $y = +0.0005 m$  near the injector side wall. The iodine mass fraction profile shows a maxima in the high pressure-gradient region, while the helium mass fraction profile shows a minima. These results are consistent with the pressure-diffusion effects previously described. As helium molecules encounter the pressure gradient they tend to diffuse in the  $+y$  direction away from the pressure gradient, resulting in a minima. Iodine molecules tend to diffuse in the  $-y$  direction toward the pressure gradient resulting in the observed maxima.

### 3.2 Transverse Helium-Iodine Injection

As a second test problem we considered the two-dimensional, transverse injection of helium and iodine into a pure helium free stream. Figure 5(a) shows the  $113 \times 81$  computational mesh used for this case. The lower surface is composed of a solid wall with the injector face located between  $x = 0.0075 m$  and  $x = 0.0077 m$ . Grid points are clustered in the vertical direction near the wall and injector face and in the horizontal direction near the injector side walls. The jet conditions

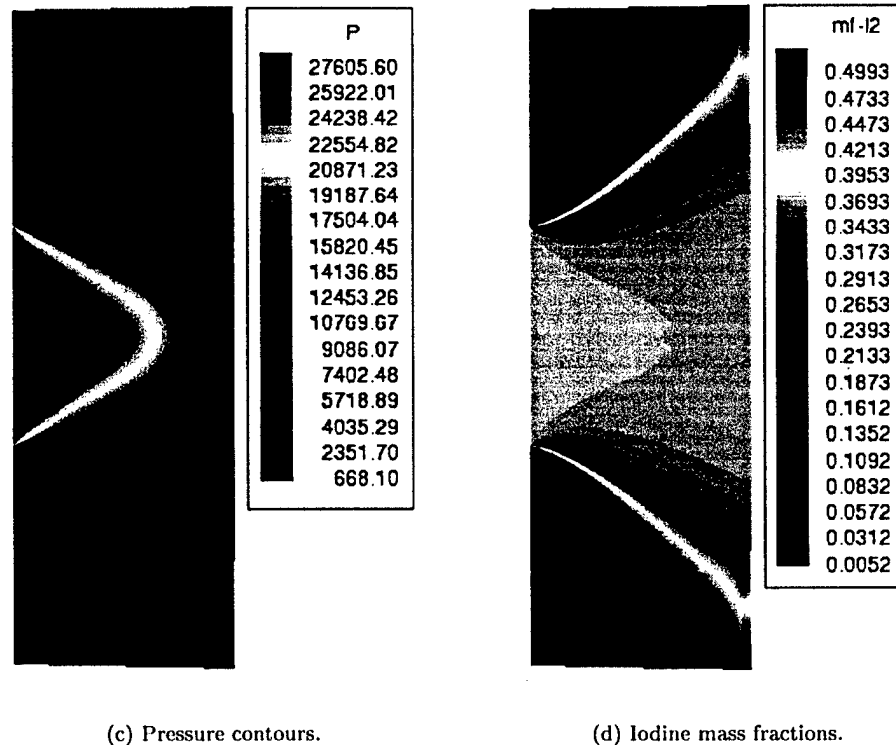
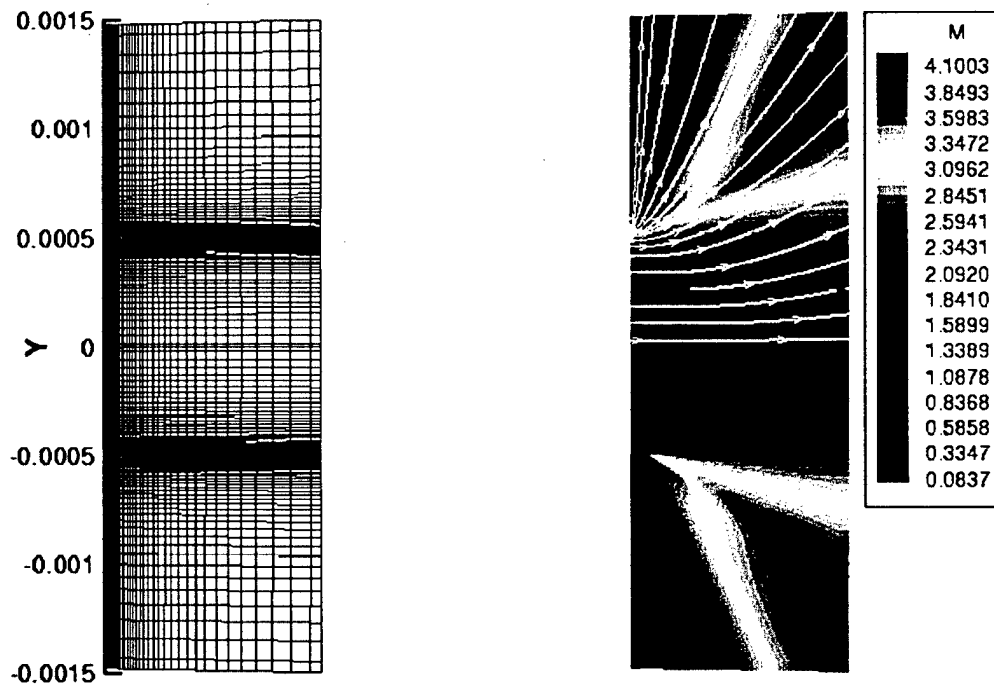


Figure 3: Helium-Iodine injection.

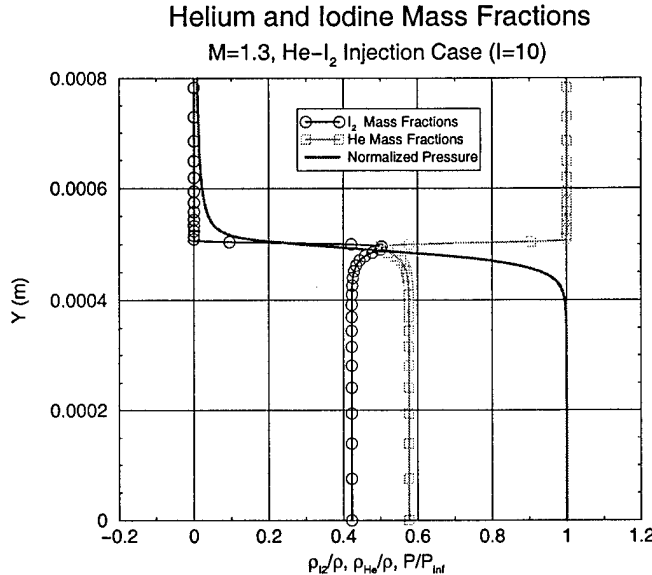


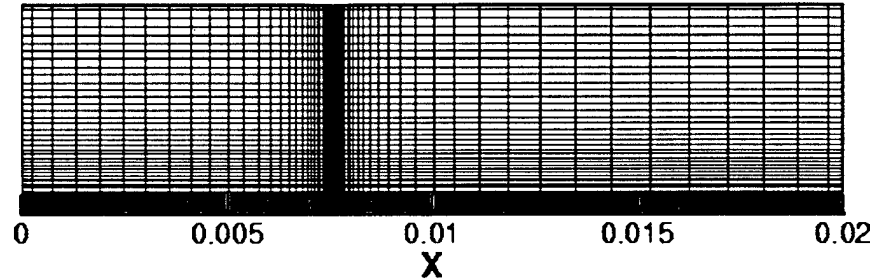
Figure 4: Helium and iodine mass fractions (station I=10)

are identical to those in Section 3.1. The free-stream conditions are identical to the initial chamber conditions in Section 3.1, except the Mach number is  $M = 0.8$  with the flow direction being left to right. As before, the jet conditions were imposed using a split-flux free-stream boundary condition and the lower wall was treated using a no-slip wall boundary condition. The subsonic inflow boundary was treated by fixing all the flow variables except pressure to the free-stream values. The pressure at the inflow boundary was extrapolated from the interior. All other boundaries were treated using first-order extrapolation from the interior.

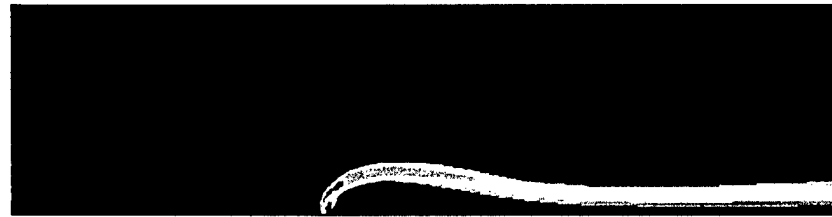
Figure 5(b) shows the iodine mass fraction contours for the complete domain. Figure 6(a) shows a close-up view of the pressure contours and streamtraces in the injector region. Comparison of these figures shows three distinct flow regions; the primary flow of helium which expands around the jet to supersonic speeds, the jet flow which contains regions of iodine concentrations that are slightly higher than jet free-stream values, and a recirculation region just to the right of the injector with lower than jet free-stream concentrations of iodine. The variation in iodine concentrations between the jet flow region and the recirculation region is caused by the pressure diffusion effects that tend to separate iodine and helium. Figure 6(b) shows the normalized pressure profile and iodine mass fraction profiles for the  $j = 2$  grid line in the injector region. The normalized pressure profile shows two large pressure-gradient regions in the vicinity of the injector side walls. The iodine mass fraction profile (for the effective diffusion model) shows peaks at these locations, indicating that the iodine molecules are diffusing in the direction of the pressure-gradient. This causes the jet flow to have slightly higher concentrations of iodine than expected. At the same time helium molecules are diffusing away from the pressure gradient causing the recirculation region to be composed of primarily helium. Figure 6(b) also shows the iodine mass fraction profile for a simulation using Fick's law, which has no pressure terms. In this case both the jet and recirculation region have helium and iodine concentrations consistent with the jet free-stream conditions. Figures 7(a) and 7(b) show iodine mass fraction contours in the vicinity of the injector for both the effective diffusion model and Fick's law.

## 4 Coupling GASP with a Laser Optics Resonator Model

COIL analysis codes currently in use at AFRL/DE can be viewed as coupled fluid dynamics and Laser Optics Resonator (LOR) codes. The *MINT* implementation [1] of the COIL simulation couples a pde-based model of the mechanics for compressible, viscous, chemically reacting flow with a ray-



(a) 2-Dimensional,  $113 \times 81$  grid.



(b) Iodine mass fraction contours.

Figure 5: Helium-iodine transverse injection case.

tracing model [2] for the optics resonator. The GASP implementation described in this section follows the same construct.

#### 4.1 Lasing Source Terms

The CFD/LOR coupling occurs through laser power extraction terms. Power extraction in the lasing cavity manifests itself in the form of source terms in the iodine species continuity equations, and in the global energy equation. The species continuity equations are affected because components at different energy states are represented as separate species. In a COIL laser, iodine in the excited,  $I(^2P_{1/2})$ , energy state is stimulated to emit photons (*i.e.*, stimulated emission). Upon emission of the photon, the iodine atom assumes the lower,  $I(^2P_{3/2})$ , energy state. As a result, power extraction affects the concentration of these two states. Power extraction also accounts for a net energy loss (through emission of photons) to the flow. The modified species continuity equation is given as

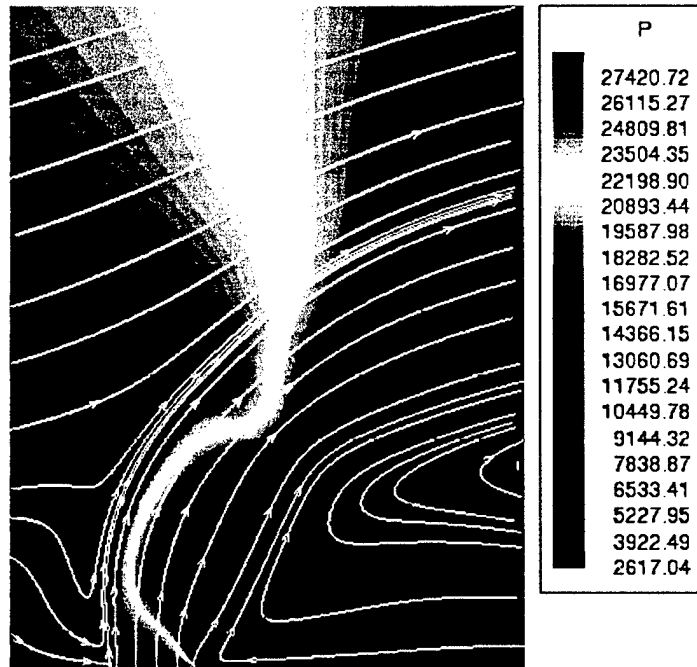
$$\frac{\partial}{\partial t} \iiint \rho_s dV + \oint_A (\rho_s \mathbf{V} \cdot \hat{\mathbf{n}}) dA = \oint_A (-\rho_s \vec{V}_s \cdot \hat{\mathbf{n}}) dA + \iiint \omega_s dV \pm \iiint \frac{\alpha \hat{I} \hat{M}_s}{h\nu} dV, \quad (23)$$

where the last term on the right-hand side of Eq (23) is the power-extraction source term. The source term is composed of the gain,  $\alpha$ , the *two-way* average intensity,  $\hat{I}$ , the molecular weight,  $\hat{M}_s$ , and the energy of a photon,  $h\nu = 90956 \text{ J/g-mole}$ . The field variable,  $\alpha$ , represents the gain and is defined as

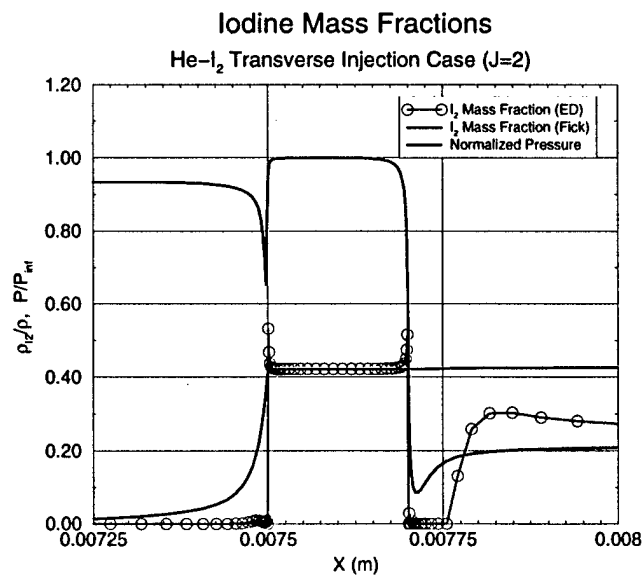
$$\alpha = \frac{7}{12} \left( \frac{A\lambda^2}{8\pi} \right) \phi(v) \left( \hat{N}_{I^*} - \frac{1}{2} \hat{N}_I \right), \quad (24)$$

where

$$\phi(v) = \frac{2}{\Delta v_D} \left( \frac{\ln 2}{\pi} \right)^{1/2} [1 - \text{erf}(\theta)] e^{\theta^2}, \quad (25)$$

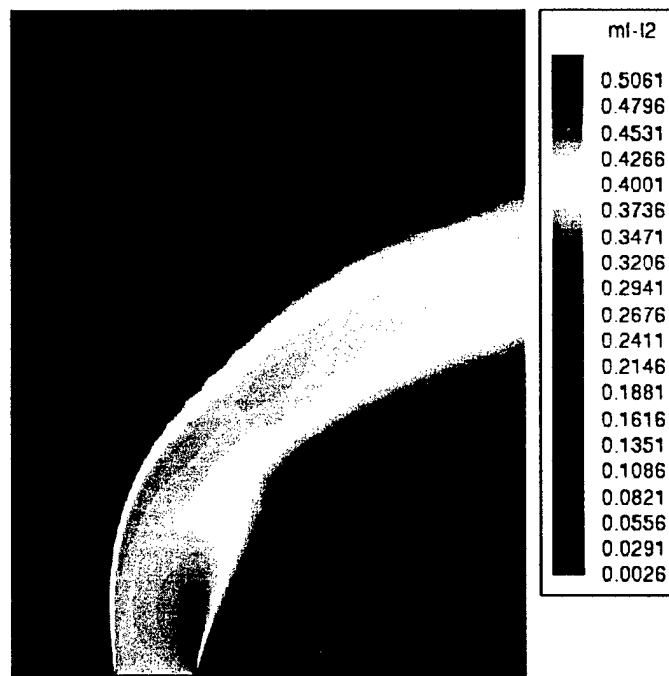


(a) Pressure contours and streamtraces.

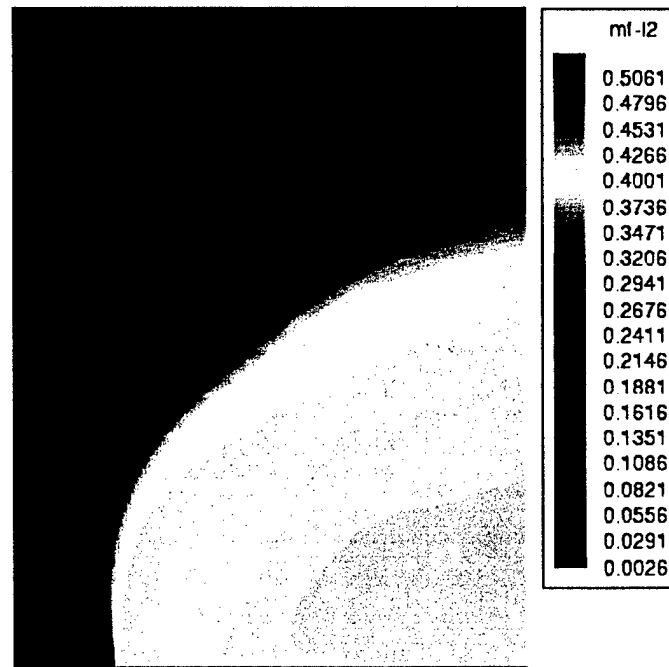


(b) Normalized pressure and iodine mass fractions.

Figure 6: Helium-iodine transverse injection case (close-up of injector).



(a) Iodine mass fractions for effective diffusion model.



(b) Iodine mass fractions for Fick's law.

Figure 7: Helium-iodine transverse injection case (close-up of injector).

and

$$\theta = \frac{\Delta v_L}{\Delta v_D} \sqrt{\ln 2}, \quad (26)$$

$$\Delta v_D = \frac{2}{\lambda} \sqrt{\frac{2RT \ln 2}{m_I}}, \quad (27)$$

$$\Delta v_L = \frac{T_{ref}}{T} p \sum_{i=1}^N \alpha_s \chi_s. \quad (28)$$

Here  $\hat{N}_{I*}$  and  $\hat{N}_I$  represent number densities for the excited and ground states of atomic iodine and  $\phi(v)$  is the Voight line-shape function. The constants  $A$  and  $\lambda$  are taken as  $A = 5.0 \text{ sec}^{-1}$  and  $\lambda = 1.31527 \times 10^{-4} \text{ cm}$ . The plus sign for the lasing source term in Eq (23) is used for the ground state of iodine and the minus sign is used for the excited state. No other species in the model has a source term contribution from power extraction. The global energy equation has a similar source term,  $-\alpha \hat{I}$ , to account for the energy removed from the flow.

The *two-way* average intensity,  $\hat{I}$ , is provided as output from the LOR model (in this work, the ray-trace model of Ref [2]), and is a function of the gain, the mirror radii and reflectivities, the geometry of the optical cavity, and various transmission and diffractive losses.

## 4.2 The Coupled CFD/LOR Model

In the coupled CFD/LOR model we have two systems, a fluid-dynamic system denoted by  $\mathcal{R}_f$  and a laser optics resonator system denoted by  $\mathcal{R}_p$

$$\mathcal{R}_f(u_f, u_p) = 0 \quad (29)$$

$$\mathcal{R}_p(u_f, u_p) = 0. \quad (30)$$

Here, the variable  $u_f$  describes the fluid-dynamic *state* and the variable  $u_p$  describes laser-power *state*. An overview of the coupled CFD/LOR analysis procedure is as follows:

1. The CFD flow solver uses a pseudo-time iteration to drive the flow residual (*i.e.*  $\mathcal{R}_f$ ) to zero. The state-variable from the laser-power extraction model, generically  $u_p$ , represents the *two-way* average intensity,  $\hat{I}$ . The intensity appears in the fluid-dynamic system in the continuity source terms for the iodine species and in the global energy equation as described above.
2. For a fixed intensity field  $\hat{I}$  the flow iteration proceeds to reduce the flow-residual. The flow-state variable, generically  $u_f$ , includes the flow velocities, thermodynamic variables and species densities. From these known quantities we compute a gain field,  $\alpha$ , using Eq (24). Values in the gain field are computed pointwise from the flow-field values.
3. The gain field is passed to the ray-tracing module for the calculation of an updated intensity field. There are several steps in this linking process that arise from modeling choices. In particular, reduced flow simulations are typically based on a *unit-cell* approximation that imposes a periodic variation of the flow-variables in the direction of the optical-axis. As a result, the gain field is averaged in the direction of the optical axis across the active region. The average gain field from the flow-solver mesh is then interpolated to a two-dimensional polar mesh consistent with the ray-trace algorithm. This interpolated gain is then passed to the ray-trace algorithm.
4. Steady-state lasing occurs for the ray-trace algorithm when the round-trip gain-equals-loss condition is satisfied. Such a steady field is achieved only when gain production and laser extraction are in equilibrium. As a result, the flow and power models must be solved simultaneously. In order to make sense of a sequential iteration procedure one must define a unique

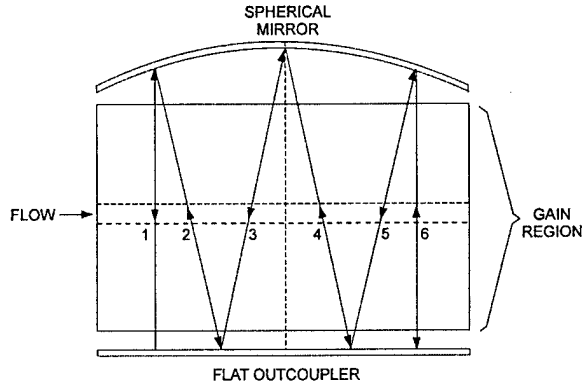


Figure 8: Schematic of the geometric optical model.

intensity field that is associated with the given gain field. The power extraction module based on [2] does this by calculating a *return* intensity and using an under-relaxation update. This process is described in more detail in the following section.

5. The updated intensity field from the power extraction module is communicated back to the flow model. These intensities are then interpolated from the polar optics mesh to the flow-solver mesh where they are used to compute updated lasing source terms.

#### 4.3 Geometric Optics Ray-Tracing Model

The main work of the laser optics resonator model is done within the ray-tracing algorithm [2]. A significant code fragment is reproduced here.

```

1000 continue
c
c      calculation of intensity on subsequent iterations, i.e., iopt = 0
c
sdifmax = 0.0
do 1500 i = 1,ntheta1
    do 1200 j = 1,nrmax
        rod(j,i) = RABS(rmaxls(i) * (xdist - xa(j)) / distm)
        sum = storg(j,i) - scripl
        alphaq(1) = storg(j,i)
        do 1100 iq = 2,m
            alam = SQRT(1.0 + (rod(j,i) * af1(iq))**2)
            alphaq(iq) = xratio(j,iq) * (storg(iset(j,iq)-1,i) -
1               storg(iset(j,iq),i)) + storg(iset(j,iq),i)
            sum = sum + alam * (alphaq(iq) - scripl)
        1100 continue
        s(j) = 2.0 * glength * sum
        exps = EXP(RMIN(expmin,s(j)))
c      ensure that stori(j,i) is not changed on restart
        if(ifirst .eq. 1) then
            iret(j) = inot(j,i)
        else
            iret(j) = inot(j,i) * r1r2m * exps * prodj(j)
        endif
        inot(j,i) = coninot * iret(j) + (1.0 - coninot) * inot(j,i)
        exp1 = EXP(RMIN(expmin,glength * (alphaq(1) - scripl)))
        term1 = (exp1 - 1.0) / (glength * (alphaq(1) - scripl))

```

```

        term2 = 1.0 + prodj(j) * (r1r2m * exps / (rm1 * exp1)) /
1           (1.0 - del(j))
      stori(j,i) = inot(j,i) * term1 * term2
c
      (several lines omitted)
1200  continue
c
      (several lines omitted)
1500  continue

```

The *i* and *j* loops are stepped through the gain region using polar coordinates to span the  $(x, y)$ -plane in a coordinate system that is convenient for the geometry of the optical cavity. Each (*i*, *j*) pair labels a point on the out-coupling mirror and the calculations within the loop implement Eq (7) in [2, page 5]. Figure 8 shows a top-view schematic of the optical cavity. Each grid point on the polar optics mesh labels a point on the out-coupling mirror. A ray of *initial* intensity,  $\hat{I}_O$ , leaving a point on the flat out-coupling mirror in an orthogonal direction will return (orthogonally) to the same point after  $2m$  passages through the gain medium. After each passage there is a specular reflection from the opposite mirror. The *return* intensity,  $\hat{I}_R$ , is given by:

$$\hat{I}_R(J) = \hat{I}_O(J)(R_1 R_2)^m e^s \prod_{p=1}^m (1 - \delta_p)s \equiv 2L_g \sum_{p=1}^m (\bar{\alpha}_p - \mathcal{L})\lambda, \quad (31)$$

where  $R_1$  and  $R_2$  are the reflectivities for the flat outcoupler and spherical mirror, and  $\bar{\alpha}_p$  is the average gain along the *p*-th ray segment. The *initial* intensity field,  $\hat{I}_O$ , for the next invocation of this routine is computed in the line:

$$\hat{I}_0 = \omega \hat{I}_R + (1 - \omega) \hat{I}_0, \quad (32)$$

or

```
inot(j,i) = coninot * iret(j) + (1.0 - coninot) * inot(j,i)
```

Note that this code fragment is embedded in an *i*-loop so the *i* variable does not appear explicitly in *iret()*. In the present version we have  $\omega = 0.5$  (*coninot* = 0.5), so that the scheme under-relaxes the intensity field. When the coupled system converges the *initial* and *return* intensity values will agree, so that, in effect, the relaxation calculation is identical to  $\hat{I}_O = \hat{I}_R$ .

Finally, the average *two-way* intensity is computed from

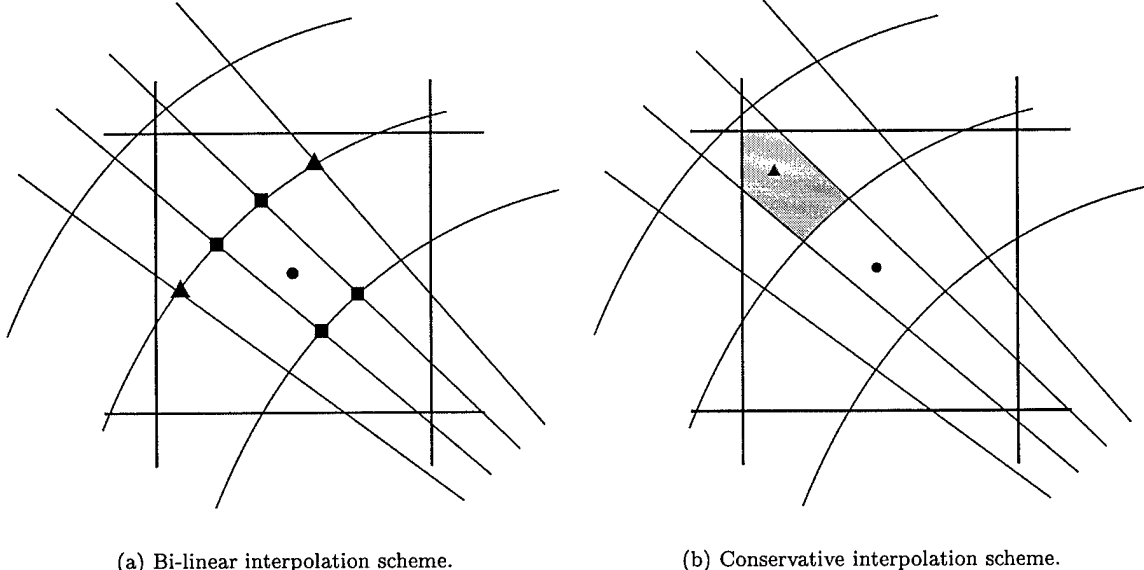
$$\hat{I} = \frac{\hat{I}_O(J) [\exp [(\alpha(J) - \mathcal{L}) L_g] - 1]}{[\alpha(J) - \mathcal{L}] L_g} \times \left[ 1 + \frac{\exp [-(\alpha(J) - \mathcal{L}) L_g]}{R_1 [1 - \delta(J)]} \right], \quad (33)$$

and passed to the CFD flow solver.

#### 4.4 Software Modifications

AeroSoft has performed modifications to GASP v4 to facilitate the power-extraction model. The new additions to GASP include:

1. Memory allocation for the gain and intensity fields.
2. Gain computation routine.
3. Lasing source term and Jacobian routines.
4. Parallel logic to gather the gain from zones (within the lasing cavity) on distributed processors.
5. Parallel logic to scatter the intensity to zones (within the lasing cavity) on distributed processors.



(a) Bi-linear interpolation scheme.

(b) Conservative interpolation scheme.

Figure 9: Schematic of mapping between flow-solver and polar optics mesh.

6. Routines to define the optics parameters and generate the polar mesh.
7. Implementation of the `stable.F` routine for the ray-tracing algorithm.
8. Interpolation routines between the flow-solver mesh and the polar optics mesh.
9. Iteration strategy for updating intensity.
10. Flow visualization capability for gain.

## 5 Fully-Coupled COIL Simulations

Initial attempts to perform a fully-coupled, power-on, RADICL simulation yielded solutions with divergent lasing power. The resulting flow fields exhibited localized regions within the lasing cavity where the intensity continued to grow unbounded. We hypothesized that this instability resulted from an “uncoupling” of grid points caused by the bi-linear interpolation method used to transfer the gain and intensity between the flow-solver and polar optics mesh. Figure 9(a) depicts the superimposed flow-solver and polar optics meshes. Notice for the particular case shown, the flow-solver mesh is very coarse relative to the optics mesh. As an example, we consider the step of transferring the intensity from the optics mesh points to the flow-solver cell center (denoted by the solid black circle). To perform this step, the bi-linear scheme finds the four closest surrounding cells in the optics mesh (*i.e.*, the squares). These four points are then used in a bi-linear interpolation to determine the cell-center value for the intensity. For the case shown in Figure 9(a) there are additional mesh points (the triangles) inside the flow-solver cell that are never used in the interpolation procedure. The intensity at these “uncoupled” points has no influence on the flow-field. Points similar to these, in our initial RADICL simulations, coincided with locations where the intensity was allowed to grow unchecked.

In order to eliminate this problem, a new conservative interpolation scheme has been developed to transfer the gain and intensity between the flow solver and optics meshes. In this scheme, a pseudo-cell is constructed around each optics grid point. The intensity at a flow-solver cell center

would then be influenced by each of the overlapping optics cells as follows

$$\hat{I}_i = \frac{\sum_j \hat{I}_j \Delta A_{ji}}{\sum_j \Delta A_{ji}}. \quad (34)$$

Here, the index  $i$  represents cells in the flow-solver mesh and the index  $j$  represents cells in the optics mesh. The area term  $A_{ji}$  represents the area of overlap for cell  $j$  (of the optics mesh) onto cell  $i$  (of the flow-solver mesh). The greyed cell in Figure 9(b) depicts the area of overlap for one of the optics cells onto a flow-solver cell. Using this method, all optics mesh points would be included in the interpolation stencil.

### 5.1 Simple Test Case

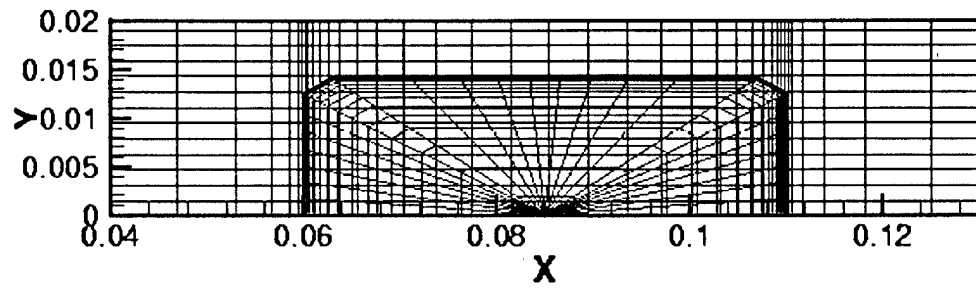
Power-on simulations have been performed for a simplified flow geometry, but with flow conditions and optical parameters consistent with the RADICL laser. This test problem reduced the debugging effort and served to demonstrate the coupled processes involved in the new power-extraction model. Figure 10(a) shows the grid topology for the  $151 \times 51$  flow-solver mesh and the  $101 \times 51$  polar optics mesh. The number of grid points shown in this figure has been reduced to facilitate viewing. Notice that the  $x$ -direction stretching at the leading and trailing edges of the optics mesh is nearly identical to the flow solver mesh. The start of the aperture is at  $x = .06\text{ m}$  and the aperture length is  $L_a = .05\text{ m}$ . The aperture height is  $H_a = .028\text{ m}$ . The distance between the curved mirror and the flat out-coupling mirror is  $D_m = 0.8\text{ m}$  and the radius of curvature of the curved mirror is  $r_2 = 10.0\text{ m}$ . The coefficients of reflectivity for the mirrors are  $R_1 = 0.90$  and  $R_2 = 0.99$  for the out-coupler and curved mirrors respectively. The gain length was taken as  $L_g = 0.25\text{ m}$ . Distributed losses in the gain medium and diffractive losses at the aperture were neglected. The inflow boundary was split into two portions; with the lower stream having a high concentration of  $I^*$  (high-gain region), and an upper stream with very little  $I^*$  and  $O_2(^1\Delta)$  (low-gain region). The low-gain region was designed to account for the region of low gain observed near the upper wall in the power-off RADICL simulations. The inflow conditions for the test case were chosen from actual conditions (upstream of the lasing cavity) for the power-off RADICL simulation, and are listed in Table 3.

For this test case the uncoupling problem did not occur and the power-on solution produced a converged value for the lasing power. The solid line in Figure 11 shows the convergence history for the lasing power in this case. Figures 10(b) and 10(c) show the gain and intensity contours for this simulation. Values for the inflow gain in the high and low-gain regions are approximately  $\alpha = 1.065\text{ 1/m}$  and  $\alpha = 0.00751\text{ 1/m}$  respectively. The maximum gain occurs in the high-gain region just before the start of the aperture and has a value of  $\alpha_{max} = 1.308\text{ 1/m}$ . Past the start of the aperture, the gain is dramatically reduced through interaction with the lasing source terms. The maximum intensity occurs at the aperture leading and trailing edges with a value of  $I_{max} = 3.6 \times 10^9\text{ W/m}^2$ . The power output for this case converged after approximately 1000 iterations and was  $P = 13.1\text{ KW}$ .

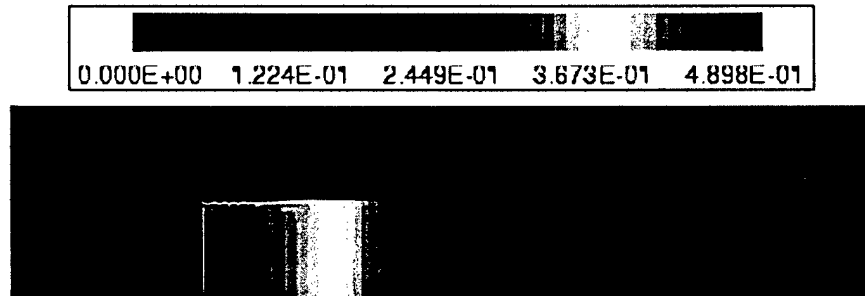
In a second test, the same case was run but with a coarsened flow-solver mesh. The coarse flow-solver mesh was obtained by sequencing five levels in both the  $x$  and  $y$  directions, yielding a  $31 \times 11$  grid. The  $101 \times 51$  optics mesh from the previous test above was used. The grid mismatch in this case should increase the possibility that grid-point uncoupling similar that shown in Fig 9 will occur. As expected, the lasing power for this case did not converge. The dashed line in Fig 11 shows the lasing power history for this case.

### 5.2 RADICL Simulation

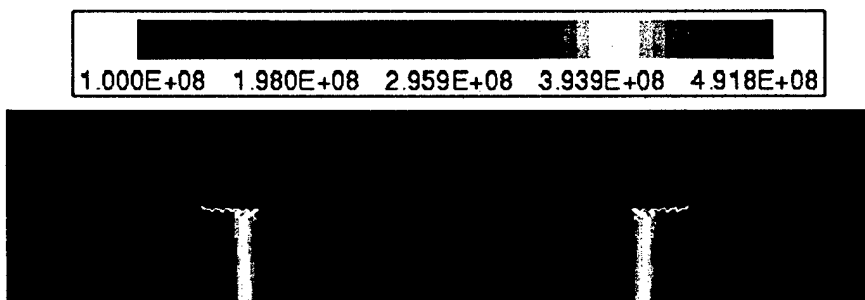
Using the new conservative interpolation scheme, a power-on simulation has been performed for the RADICL device. The physical domain of the RADICL simulation is depicted in the coarsened view of the computational mesh shown in Figure 13. Figure 14(a) shows a close-up view of injector region. Our simulation considered only the upper half of this domain, and employed symmetry conditions about the centerline of the nozzle. In the lateral direction (*i.e.*, into the page), the RADICL device



(a) Coarsened flow-solver mesh and polar optics mesh.



(b) Gain contours ( $1/m$ ).



(c) Intensity contours ( $Watts/m^2$ ).

Figure 10: Test laser configuration and results.

Variable	High-Gain Region	Low-Gain Region
$\rho_{He}$	$0.00260088 \text{ Kg/m}^3$	$0.000860848 \text{ Kg/m}^3$
$\rho_{O_2}$	$0.00208539 \text{ Kg/m}^3$	$0.000811512 \text{ Kg/m}^3$
$\rho_{O_2(^1\Delta)}$	$0.00161352 \text{ Kg/m}^3$	$0.000831930 \text{ Kg/m}^3$
$\rho_{O_2(^3\Sigma)}$	$2.29196 \times 10^{-6} \text{ Kg/m}^3$	$8.38014 \times 10^{-8} \text{ Kg/m}^3$
$\rho_{H_2O}$	$0.000247298 \text{ Kg/m}^3$	$0.000110298 \text{ Kg/m}^3$
$\rho_{I_2}$	$0.000235656 \text{ Kg/m}^3$	$7.09078 \times 10^{-5} \text{ Kg/m}^3$
$\rho_{I_2^*}$	$8.97101 \times 10^{-7} \text{ Kg/m}^3$	$8.90463 \times 10^{-9} \text{ Kg/m}^3$
$\rho_I$	$4.74918 \times 10^{-5} \text{ Kg/m}^3$	$1.79366 \times 10^{-6} \text{ Kg/m}^3$
$\rho_{I^*}$	$0.000319047 \text{ Kg/m}^3$	$4.33212 \times 10^{-6} \text{ Kg/m}^3$
$\rho_{Cl_2}$	$0.00122394 \text{ Kg/m}^3$	$0.000545616 \text{ Kg/m}^3$
$u$	$881.8 \text{ m/s}$	$990.9 \text{ m/s}$
$v$	$0.0 \text{ m/s}$	$0.0 \text{ m/s}$
$w$	$0.0 \text{ m/s}$	$0.0 \text{ m/s}$
$p$	$1124.6 \text{ N/m}^2$	$1200.0 \text{ N/m}^2$

Table 3: Inflow conditions for laser test case.

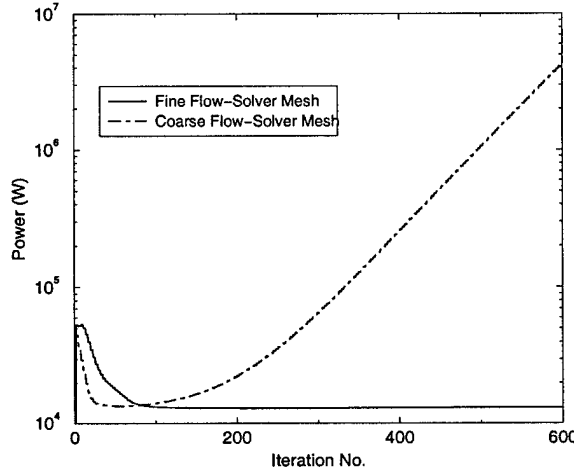


Figure 11: Lasing power vs. iteration number.

consists of 115 sets of injector orifices (on both the upper and lower walls), each set consisting of one large and two small injector orifices. Figure 12 shows three such sets of injectors. Each injector set is symmetric about the centerline plane of the large injector orifice. The large orifices have a diameter of  $D_L = 0.08128 \text{ cm}$  and the small orifices have a diameter of  $D_S = 0.04064 \text{ cm}$ . We now make a key assumption that the bulk effect of all the injector sets and nozzle side walls has a minimal influence on a single chosen injector set. With this assumption a single injector set can be isolated for simulation and the lateral extent of the domain can be reduced by employing symmetry. Our simulation was performed on the representative sub-domain of the COIL flow field termed the “unit cell” and depicted by the dashed line in Figure 12. The unit cell consists of half of a large orifice and one small orifice. While the ramifications of this approximation are not fully understood, our goal was to model the flow field with a sufficient level of detail so as to capture the physical processes necessary to test our coupling procedures. This would have been impossible for the complete physical domain because a prohibitive number of grid points would be required.

The RADICL grid system consisted of four zones; a  $6 \times 21 \times 9$  mesh for the large injector, a  $5 \times 21 \times 9$  mesh for the small injector, a  $147 \times 77 \times 25$  mesh that includes the upstream portion of the mixing nozzle and throat, and a  $145 \times 77 \times 25$  mesh for the downstream portion of the nozzle that contains the optical cavity. Grid points were clustered in the  $x$ -direction near the leading and

trailing edges of the aperture as depicted in Figure 13. A total of 564,179 grid points were used.

Nozzle inflow conditions are specified using a subsonic inflow boundary condition with fixed total pressure and temperature. The total conditions were consistent with the measured static values for pressure and temperature of  $p = 9961.7 \text{ N/m}^2$  and  $T = 315 \text{ K}$ . The chemical composition at the inflow was consistent with measured molar flow rates and an  $O_2(^1\Delta)$  yield of  $Y = 0.41$ . The species inflow densities were specified as

$$\begin{aligned}\rho_{He} &= 0.01117200 \text{ Kg/m}^3 \\ \rho_{O_2(^3\Sigma)} &= 0.01544990 \text{ Kg/m}^3 \\ \rho_{O_2(^1\Delta)} &= 0.01073640 \text{ Kg/m}^3 \\ \rho_{O_2(^1\Sigma)} &= 0.00000019 \text{ Kg/m}^3 \\ \rho_{H_2O} &= 0.00139578 \text{ Kg/m}^3 \\ \rho_{CI_2} &= 0.00828914 \text{ Kg/m}^3.\end{aligned}$$

The inflow velocity was  $V = 84.028 \text{ m/s}$ . The injector inflow conditions were specified using the same subsonic inflow boundary condition. The total temperature was taken to be  $T_t = 400 \text{ K}$ , and the species densities were specified to match measured molar flow rates of  $He$  and  $I_2$  and are given as follows

$$\begin{aligned}\rho_{He} &= 0.0246814 \text{ Kg/m}^3 \\ \rho_{I_2} &= 0.0132298 \text{ Kg/m}^3.\end{aligned}$$

The nozzle wall is treated as a  $T = 315 \text{ K}$ , no-slip wall.

The aperture (and associated mirror system) was located between  $x = 0.08578 \text{ m}$  and  $x = 0.14578 \text{ m}$ . The length of the aperture was  $L_a = 0.06 \text{ m}$ . The distance between the spherical mirror and the flat out-coupling mirror is  $D_m = 0.8 \text{ m}$  and the radius of curvature of the spherical mirror is  $r_2 = 10.0 \text{ m}$ . The coefficients of reflectivity are  $R_1 = 0.927$  and  $R_2 = 0.995$  for the flat out-coupler and spherical mirrors respectively. The gain length was taken as  $L_g = 0.254 \text{ m}$  (the lateral width of the nozzle). Distributed losses in the gain medium and diffractive losses at the aperture were neglected. The polar mesh size for the ray-tracing algorithm was  $101 \times 41$  and laser optics resonator model was called on every third flow-solver iteration.

The solution procedure utilized four mesh sequences and required approximately 50 hours on a 32 processor SGI Origin. The fine-grid solution required 1000 iterations to reduce the  $l_2$ -norm of the residual approximately 2.5 orders of magnitude. GASP v4 required 10 GB of memory to execute on the fine mesh utilizing fully-implicit zonal boundaries.

Figure 14(b) shows the Mach number contours in the vicinity of the injector region for the  $k = 9$  nodal plane. The Mach number contours provide some indication of the jet penetration into the primary flow. The flow from the large injector reaches the nozzle centerline just upstream of the throat. Figure 15(a) shows the averaged gain contours for the downstream section of the nozzle including the optical cavity. Gain values are the highest just before the start of the aperture, with a maximum of  $\alpha_{max} = 1.0621/\text{m}$ . Past the start of the aperture, the gain is dramatically reduced through interaction with the lasing source terms. The experimentally measured gain 1 cm upstream of the aperture leading edge and on the nozzle centerline was  $\alpha = 0.801/\text{m}$ . The COIL simulation predicted a gain at this location of  $\alpha = 0.79941/\text{m}$ . Figure 15(b) shows the intensity contours predicted by the ray-tracing algorithm in the lasing cavity. The maximum value of intensity occurs at the aperture leading and trailing edges with a value of  $I_{max} = 3.6 \times 10^9 \text{ W/m}^2$ . The laser power output predicted for this simulation was  $P = 7.524 \text{ KW}$ . The experimentally measured value of power was  $P = 5.8 \text{ KW}$ . This is reasonable agreement, since no loss terms were included. Similar studies (e.g., Buggeln [1]) have used non-zero values for mirror scattering and diffractive losses to give corrected output powers that are up to 20% lower than the zero-loss power. Assuming similar behavior for this case, our power results are in very good agreement with the measured value. The results of this study were presented in Eppard [4].

## 6 Water-Vapor Condensation Model

Water vapor is produced as a by-product in the COIL's singlet-delta oxygen generator. Since water vapor is very efficient at deactivating the excited state of iodine, it is removed before the singlet oxygen is mixed with iodine. Unfortunately, a small portion of water vapor escapes the removal system, mixes with the iodine and expands through the nozzle. The rapid decrease in temperature in the diverging section of the nozzle results in the nucleation and subsequent growth of water droplets. The positive aspect of condensation is that it reduces the amount of water vapor in the mixture, and therefore suppresses the deactivation of excited iodine. Unfortunately, as the water vapor condenses the latent heat release into the flow raises the temperature considerably in the lasing cavity. This increase in temperature causes a significant reduction in the gain and therefore power output.

To model this effect, we have implemented into GASP v4 a homogeneous water-vapor condensation model similar to that described by Masuda [10]. The model includes the latent heat in the global energy equation and accounts for inter-phase mass transfer through source terms in the water vapor and droplet continuity equations. The model assumes that the water droplets have the same velocity as the gas phase, and does not require particle tracking. This assumption is reasonable since the droplet size within the COIL is very small. Finally, we assume that the water droplets are in thermal equilibrium with the carrier gas, *i.e.*, the droplet temperature is identical to the gas-phase temperature. These assumptions are consistent with the previous COIL analysis of Masuda [10].

The condensation model considers the liquid phase using a number of droplet classes, or partitions. Each class contains only droplets within a certain range of sizes, which are approximated as one average size. The continuity equation for droplets of class  $k$  is very similar to that for the gaseous species and is solved in a fully-coupled approach with the fluid dynamics. The class- $k$  droplet continuity equation is implemented in GASP v4 as:

$$\frac{\partial}{\partial t} \iiint \rho_k dV + \oint_A \rho_k (\mathbf{V} \cdot \hat{\mathbf{n}}) dA = \iiint \dot{\rho}_k dV.$$

Here  $\rho_k$  is the density of droplet class  $k$  in the two-phase fluid. The droplet source term,  $\dot{\rho}_k$ , is modeled as three separate components

$$\dot{\rho}_k = \dot{\rho}_{k,1} + \dot{\rho}_{k,2} + \dot{\rho}_{k,3}, \quad (35)$$

which represent nucleation, growth, and transport of droplets between the classes respectively.

### 6.1 Nucleation

The nucleation source term,  $\dot{\rho}_{k,1}$ , is given as

$$\dot{\rho}_{k,1} = \begin{cases} \rho_L V^* J : \text{for class } k \text{ where } r_{k-1/2} < r^* < r_{k+1/2} \\ 0 : \text{all other classes,} \end{cases} \quad (36)$$

where  $\rho_L$  is the density of the liquid water,  $V^*$  ( $= 4/3\pi r^*{}^3$ ) is the volume of a nucleating droplet,  $J$  is the nucleation rate per unit time and volume, and  $r^*$  is the critical radius of a nucleating droplet. The nucleation rate is given as

$$J = \sqrt{\frac{2\sigma_0}{\pi}} \hat{m}_{H_2O}^{-3/2} \frac{\rho_v^2}{\rho_L} \exp\left(\frac{-\Delta G}{kT}\right), \quad (37)$$

where  $\sigma_0$  is the surface tension for a plane surface, computed as

$$\sigma_0 = \begin{cases} 0.0761 + 0.000155(273.15 - T) : T \leq 764 K \\ 0.0 : T > 764 K, \end{cases}$$

$\hat{m}_{H_2O}$  is the mass of a water molecule,  $\rho_v$  is the density of the water vapor,  $k$  is Boltzmann's constant and  $\Delta G$  is given as

$$\Delta G = \frac{16}{3} \pi \left( \frac{\hat{m}_{H_2O}}{\rho_L \ln s k T} \right)^2 \sigma_0^3. \quad (38)$$

Here,  $s$  ( $= p_v/p_{so}$ ) is the supersaturation ratio where  $p_v$  is the partial pressure of the water vapor and  $p_{so}$  is the saturation pressure of a plane liquid surface given as

$$p_{so} = \exp(-1187.5658 + 529.80132 \ln T - 78.600891 \ln^2 T + 3.9393576 \ln^3 T). \quad (39)$$

The critical radius is given by

$$r^* = \frac{2 \sigma_0}{\rho_L R_v T \ln(s)}, \quad (40)$$

where  $R_v$  is the gas constant of the water vapor.

## 6.2 Growth

Following the onset of nucleation, the radii of existing droplets increase due to further condensation and evaporation. The source term for droplet class  $k$  due to growth is given as

$$\dot{\rho}_{k,2} = n_k \left( \frac{\partial \rho_L V}{\partial t} \right)_k = \frac{3 \rho_k}{r_k} \left( \frac{\partial r}{\partial t} \right)_k, \quad (41)$$

where  $n_k (= \rho_k / \rho_L V_k)$  is the number density of class- $k$  droplets. The rate of change in droplet radius in Eq (41) is modeled as

$$\frac{\partial r}{\partial t} = \frac{\theta (p_v - p_{sr})}{\rho_L (2 \pi R_v T)^{1/2}}, \quad (42)$$

where  $\theta$  is the condensation coefficient given as

$$\theta = \begin{cases} 0.5 : T > 270 K \\ 1.0 - 0.0125 (T - 230) : 230 K < T < 270 K \\ 1.0 : T < 230 K, \end{cases} \quad (43)$$

and  $p_{sr}$  is the saturation pressure of a droplet of radius  $r$ , given as

$$p_{sr} = p_{so} \exp \left( \frac{2 \sigma}{\rho_L R_v T r} \right). \quad (44)$$

Here  $\sigma (= \xi \sigma_0)$  is the surface tension of the droplet and  $\xi$  is the coefficient of surface tension. Note that in our calculations  $\xi = 1.0$ .

## 6.3 Transport

Droplet growth also produces a transport of droplets (*i.e.*, a droplet flux) across the partition boundaries. For example, when droplets at the  $k + 1/2$  partition boundary grow they leave class  $k$  and become part of the  $k + 1$  class. In order to model the number density distribution within a class, we introduce a distribution function of the number density,  $\nu_r$ , such that the number of droplets with radii between  $r$  and  $r + dr$  is given by  $dn = \nu_r dr$ . Utilizing the distribution function, the source term for class  $k$  due to transport is given as

$$\dot{\rho}_{k,3} = (\rho_L V \nu_r)_{k-1/2} \left( \frac{\partial r}{\partial t} \right)_{k-1/2} - (\rho_L V \nu_r)_{k+1/2} \left( \frac{\partial r}{\partial t} \right)_{k+1/2}. \quad (45)$$

Notice that growth at the  $k - 1/2$  partition boundary gives a positive contribution to the source term while growth at the  $k + 1/2$  boundary gives a negative contribution. Utilizing a linear reconstruction for the grouping  $(\rho_L V \nu_r)_{k \pm 1/2}$  and further assuming that  $\nu_r$  is a piecewise linear function yields

$$(\rho_L V \nu_r)_{k-1/2} = \frac{1}{\Delta r_{k-1} + \Delta r_k} \left[ \Delta r_k \frac{\rho_{k-1}}{\Delta r_{k-1}} + \Delta r_{k-1} \frac{\rho_k}{\Delta r_k} \right], \quad (46)$$

$$(\rho_L V \nu_r)_{k+1/2} = \frac{1}{\Delta r_k + \Delta r_{k+1}} \left[ \Delta r_{k+1} \frac{\rho_k}{\Delta r_k} + \Delta r_k \frac{\rho_{k+1}}{\Delta r_{k+1}} \right], \quad (47)$$

where  $\Delta r_k = r_{k+1/2} - r_{k-1/2}$ .

## 6.4 Coupling Issues

The liquid-phase species are treated in a nearly identical fashion to the gas-phase species. The mixture density for the two-phase fluid is determined as the sum of the specie densities for both the gas and liquid-phase species as follows

$$\rho = \sum_{i=1}^{N_s} \rho_i + \sum_{k=1}^{N_k} \rho_k. \quad (48)$$

Here,  $N_s$  is the total number of gaseous species and  $N_k$  is the total number of liquid species. The mixture pressure is determined as the sum of the partial pressures of only the gaseous species

$$p = \sum_{i=1}^{N_s} p_i = \sum_{i=1}^{N_s} \rho_i R_i T = \rho \tilde{R} T, \quad (49)$$

where the mixture gas constant,  $\tilde{R}$ , is given as

$$\tilde{R} = \sum_{i=1}^{N_s} \frac{\rho_i}{\rho} R_i. \quad (50)$$

The energy for the liquid-phase species is given as

$$e_k = \int_{T_{ref}}^T \tilde{C}_{vL} d\tau + h_{fH_2O(g)}^0 + \mathcal{L} \quad k = 1, 2, \dots, N_k, \quad (51)$$

where  $\mathcal{L}$  is the latent heat.

The liquid-phase species' continuity equations do not include viscous diffusion terms and the liquid species do not contribute to the mixture viscosity, mixture thermal conductivity, or effective diffusion coefficients. To account for the interphase mass transport, the chemical-production source term for water vapor is modified to include the effects of condensation or evaporation, *i.e.*,  $\dot{\rho}_v = -\sum_{i=1}^{N_k} \dot{\rho}_k$ .

## 6.5 Power-Off RADICL Simulation with Condensation

Two additional RADICL simulations have been performed using GASP v4 to study the effects of water-vapor condensation. These simulations were both obtained for power-off conditions and include a “baseline” case without water-vapor condensation and a “condensation-on” case that includes condensation effects. Both calculations were performed using the same flow conditions and grid system as the previously-described RADICL simulation (see Section 5.2).

The condensation calculation utilized 5 water classes with average droplet radii of

$$\begin{aligned}
 r_1 &= 7 \times 10^{-10} m \\
 r_2 &= 2 \times 10^{-9} m \\
 r_3 &= 1 \times 10^{-8} m \\
 r_4 &= 1 \times 10^{-7} m \\
 r_5 &= 1 \times 10^{-6} m .
 \end{aligned} \tag{52}$$

Condensation occurs in the diverging section of the nozzle, where the rapid decrease in temperature results in the nucleation and subsequent growth of water droplets. Figure 16 shows contours of the log of the number density, *i.e.*,  $\text{Log}_{10}(n_k)$ , for each of the droplet classes in the  $k = 5$  vertical plane. Nucleation begins just downstream of the throat, and occurs entirely in the  $7.0 \times 10^{-10} m$  class. Droplet growth and transport occurs rapidly, and significant number densities occur in the larger droplet classes. This process occurs progressively further down stream for each class due to the finite time scale for droplet growth and transport. The largest  $1.0 \times 10^{-6} m$  class only has significant number densities further down stream near the optical cavity.

Figure 17 shows the  $\text{Log}_{10}(n_k)$  profile for each of the water droplet classes at  $x = 0.11578 m$  (*i.e.*, the optical axis) in the  $k = 5$  vertical plane. The vertical axis represents the  $y$  coordinate and starts at the symmetry plane (*i.e.*,  $y = 0.0$ ) and ends at the upper nozzle wall. Notice that practically no water droplets form in the boundary layer near the upper wall. The GASP v4 simulation predicted maximum number densities of  $n_1 \simeq 10^{19.5}$ ,  $n_2 \simeq 10^{17.6}$ ,  $n_3 \simeq 10^{14.3}$ ,  $n_4 \simeq 10^{8.9}$ , and  $n_5 \simeq 10^{2.6}$  particles/ $m^3$ . These number densities are very similar to those predicted by Masuda [10] for the S-Coil system.

Figure 19 shows gain contours for the condensation-on case and the baseline case. The gain contours are very similar in the upstream region, however, as condensation begins to become significant, the gain is reduced for the condensation-on case. This fact is evident by the diminished extent of the high-gain (*i.e.*, red) contours for the condensation-on case. As the water vapor condenses, the latent heat release into the flow raises the temperature. This increase in temperature causes a significant reduction in the concentration of excited iodine,  $I^*$ , and therefore reduces the gain. To illustrate this effect, consider the pumping reaction which controls the production of excited iodine:



where

$$k_f = 4.697 \times 10^{10} \quad (m^3/\text{Kg-mol/s}) \tag{54}$$

$$k_b = 6.323 \times 10^{10} \exp^{-401.4/T} \quad (m^3/\text{Kg-mol/s}) . \tag{55}$$

The backward rate increases with increasing temperature, and leads to the reduction in excited iodine. [Note: In GASP the backward reactions are computed using the LeRC curve fits coupled with the minimization of Gibb's free energy. However, the backward Arrhenius rate in Eq (55) represents an equivalent formulation.] Figure 18 shows the gain and temperature profiles at the  $x = 0.11578 m$  station for both the baseline and condensation-on case. The gain is about 4% lower in the core flow region for the condensation-on case compared to the baseline case. The temperature in the core flow region for the condensation-on case is approximately 7K higher than for the baseline case. Because the gain is a measure of the flow's photon extraction potential, we would expect a reduction in the output power for the condensation-on case.

Initial attempts at running the RADICL configuration with condensation yielded much less liquid water than was experienced by Masuda [10] for similar conditions. Examination of the results indicated that the solution could be greatly affected by the droplet sizes chosen. Initially we chose droplet radii of  $r_1 = 1 \times 10^{-10} m$  and  $r_2 = 1 \times 10^{-9} m$  for the first two classes. The remaining three classes had the same radii as described in Eq (52). For this case, the first droplet class had partition boundaries of  $5.5 \times 10^{-11} m$  on the lower boundary and  $5.5 \times 10^{-10} m$  on the upper boundary. It turned out for this droplet discretization, most of the nucleating droplets evaporated before they

could grow and transport. To see this, we rewrite Eq (42) in terms of the supersaturation ratio,  $s$ , and the critical radius,  $r^*$

$$\frac{\partial r}{\partial t} = \frac{\theta p_v (1 - s^{r^*/r-1})}{\rho_L (2\pi R_v T)^{1/2}}. \quad (56)$$

The sign of  $\partial r/\partial t$  depends on the size of the droplet in relation to the critical radius as follows:

$$\begin{aligned} r = r^* &\rightarrow r^*/r - 1 = 0 \rightarrow \partial r/\partial t = 0 \\ r < r^* ; s > 1 &\rightarrow r^*/r - 1 > 0 \rightarrow \partial r/\partial t < 0 \\ r > r^* ; s > 1 &\rightarrow r^*/r - 1 < 0 \rightarrow \partial r/\partial t > 0 \end{aligned}$$

Note that when  $s > 0$  the vapor pressure is greater than the saturation pressure and condensation should occur. For the RADICL conditions, the critical radius at which droplets nucleate was within the range of  $1.69 \times 10^{-10} m \leq r^* \leq 6.5 \times 10^{-10} m$ . For the initial droplet discretization, this range of critical radii occurred almost entirely between the average droplet size of the first class (*i.e.*,  $1 \times 10^{-10} m$ ) and the right partition boundary (*i.e.*,  $5.5 \times 10^{-10} m$ ). For this case  $r_1 < r^*$  and  $\partial r_1/\partial t < 0$ . Hence the droplets that nucleate into the first class begin immediately to evaporate. The rate at which the droplets evaporate depends on the magnitude of the supersaturation ratio. For the RADICL conditions under consideration, the supersaturation ratio is large and on the order of  $s = 10^6$ , causing rapid evaporation of nucleating droplets. For the modified set of droplet radii described in Eq (52), nucleation occurs entirely between the left partition boundary (*i.e.*,  $1 \times 10^{-10} m$ ) and the average droplet size for the first class (*i.e.*,  $7 \times 10^{-10} m$ ). For this case  $r_1 > r^*$  and  $\partial r_1/\partial t > 0$ . Hence the droplets that nucleate into the first class begin immediately to grow. Increasing the number of droplet partitions can help alleviate this discretization problem, however, future research must be conducted to determine a logical way to select droplet sizes and partition boundaries.

## 7 Wall Catalysis Model

COIL efficiency can also be adversely affected by wall-catalysis reactions. These reactions promote the deactivation of excited species that collide with the nozzle wall. Wall catalysis effects on the gas-phase chemical composition are modeled in GASP v4 using a surface mass-balance boundary condition coupled with specified wall deactivation and recombination reactions. The wall mass balance equation for the  $i$ th specie is given as

$$\rho_i \vec{v}_i \cdot \hat{n} = \sum_{r=1}^{N_r} \omega_i^r \quad i = 1, 2, \dots, N_s, \quad (57)$$

where  $\vec{v}_i$  is the  $i$ th-specie's diffusional velocity and  $\omega_i^r$  represents chemical production of the  $i$ th specie due to surface reaction  $r$ . Equation (57) states that the diffusional mass flux of specie  $i$  leaving the wall must equal the rate of production of specie  $i$  through wall catalysis reactions. To be consistent, the wall diffusion model utilized in Eq (57) should be the same as that used in the interior flow, *i.e.*, the effective diffusion model.

### 7.1 Surface Mass Balance

The surface mass balance equation has been implemented within the framework of a fixed-temperature, no-slip, wall boundary condition. The no-slip, wall boundary condition utilizes a zero-pressure-gradient condition normal to the wall to determine the wall pressure. As a result of this assumption, the pressure diffusion terms in Eq (16) can be neglected, and substitution of the effective diffusional mass flux into Eq (57) yields

$$\left[ \frac{\rho_i}{\rho} \sum_{j=1}^{N_s} \mathbf{G}_j^X - \mathbf{G}_i^X \right] \cdot \hat{n} = \frac{1}{\eta_t} \sum_{r=1}^{N_r} \omega_i^r \quad i = 1, 2, \dots, N_s. \quad (58)$$

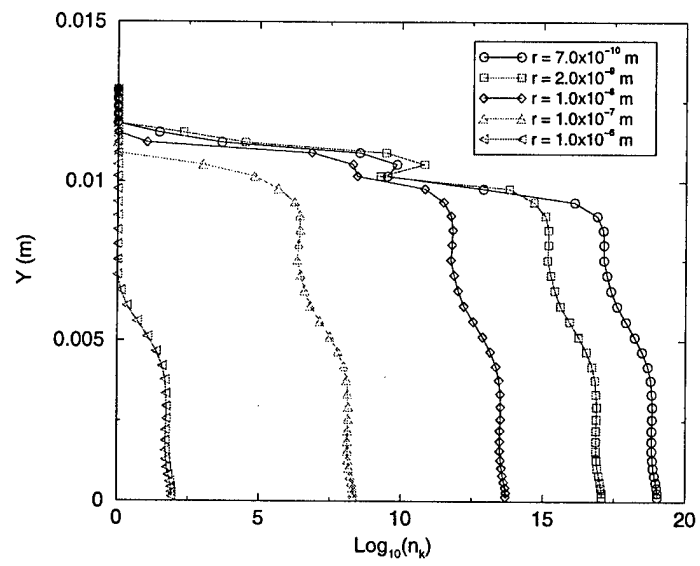


Figure 17: Water droplet number density profile,  $\text{Log}_{10}(n_k)$ , profiles at the RADICL optical axis ( $x = 0.11578\text{m}$ ).

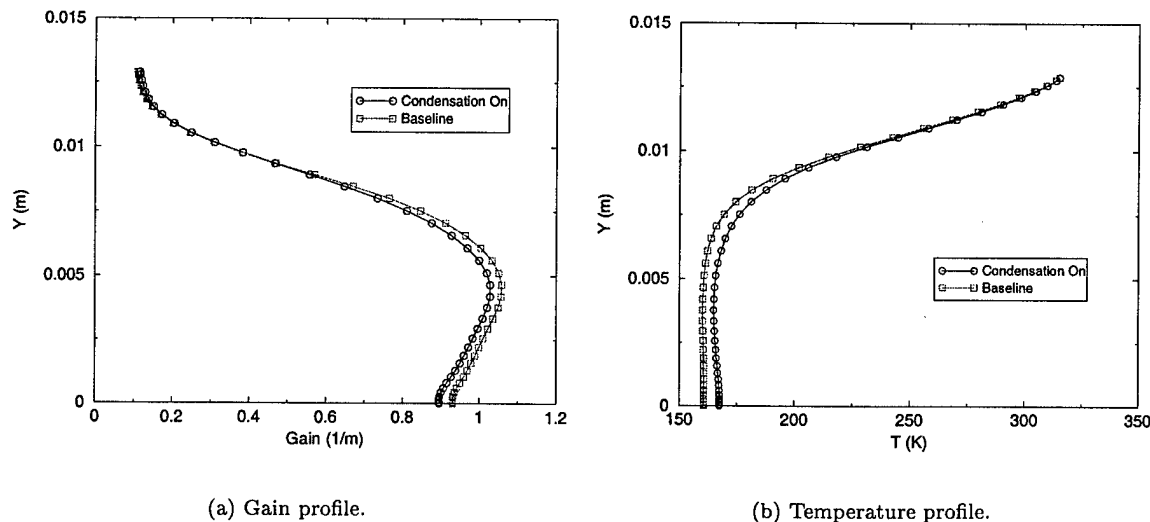


Figure 18: Gain ( $1/\text{m}$ ) and temperature ( $K$ ) profiles at the RADICL optical axis ( $x = 0.11578\text{m}$ ).

r	Reaction	$\beta_i^r$ (FC)	$\beta_i^r$ (Mod)
1	$O_2(^1\Sigma) + \text{wall} \rightarrow O_2(^1\Delta) + \text{wall}$	1.0	0.0
2	$O_2(^1\Sigma) + \text{wall} \rightarrow O_2(^3\Sigma) + \text{wall}$	0.0	$1.6e^{-2}$
3	$O_2(^1\Delta) + \text{wall} \rightarrow O_2(^3\Sigma) + \text{wall}$	1.0	$1.3e^{-5}$
4	$I(^2P_{1/2}) + \text{wall} \rightarrow I(^2P_{3/2}) + \text{wall}$	1.0	1.0
5	$I_2^* + \text{wall} \rightarrow I_2 + \text{wall}$	1.0	1.0
6	$2I(^2P_{1/2}) + \text{wall} \rightarrow I_2 + \text{wall}$	0.0	0.0
7	$2I(^2P_{3/2}) + \text{wall} \rightarrow I_2 + \text{wall}$	1.0	1.0

Table 4: Catalytic wall reactions with fully-catalytic (FC) efficiencies as used by Hishida [8], and modified efficiencies (Mod) as suggested by Madden [9].

Utilizing Eq (61), the catalytic production terms on the right-hand side of Eq (58) in  $Kg/m^2/s$  are:

$$\begin{aligned} \sum_{r=1}^{N_r} \omega_{O_2(^3\Sigma)}^r &= \hat{M}_{O_2(^3\Sigma)} \left( \dot{\eta}_{O_2(^1\Sigma)}^2 + \dot{\eta}_{O_2(^1\Delta)}^3 \right) \\ \sum_{r=1}^{N_r} \omega_{O_2(^1\Delta)}^r &= \hat{M}_{O_2(^1\Delta)} \left( \dot{\eta}_{O_2(^1\Sigma)}^1 - \dot{\eta}_{O_2(^1\Delta)}^3 \right) \\ \sum_{r=1}^{N_r} \omega_{O_2(^1\Sigma)}^r &= \hat{M}_{O_2(^1\Sigma)} \left( -\dot{\eta}_{O_2(^1\Sigma)}^1 - \dot{\eta}_{O_2(^1\Sigma)}^2 \right) \\ \sum_{r=1}^{N_r} \omega_{I(^2P_{3/2})}^r &= \hat{M}_{I(^2P_{3/2})} \left( \dot{\eta}_{I(^2P_{1/2})}^4 - \dot{\eta}_{I(^2P_{3/2})}^7 \right) \\ \sum_{r=1}^{N_r} \omega_{I(^2P_{1/2})}^r &= \hat{M}_{I(^2P_{1/2})} \left( -\dot{\eta}_{I(^2P_{1/2})}^4 - \dot{\eta}_{I(^2P_{3/2})}^6 \right) \\ \sum_{r=1}^{N_r} \omega_{I_2}^r &= \hat{M}_{I_2} \left( \dot{\eta}_{I_2^*}^5 + \frac{1}{2} \dot{\eta}_{I(^2P_{1/2})}^6 + \frac{1}{2} \dot{\eta}_{I(^2P_{3/2})}^7 \right) \\ \sum_{r=1}^{N_r} \omega_{I_2^*}^r &= -\hat{M}_{I_2^*} \dot{\eta}_{I_2^*}^5. \end{aligned}$$

The source terms for the non-catalytic species, *i.e.*,  $He$ ,  $H_2O$ , and  $Cl_2$ , are zero. The species' source terms above are substituted into their corresponding mass balance equation, *i.e.*, Eq (58), and division through by the mixture concentration,  $\eta_t$ , yields a right-hand side in terms of mole fractions at the wall.

In the most general procedure Eq (58) is discretized using finite differences and solved in a coupled fashion for the  $N_s$  species' mole fractions at each point on the surface. First-order discretization of the mole-fraction gradients in Eq (58) yields

$$\frac{\chi_i^{(w)} \hat{M}_i}{\sum_{l=1}^{N_s} \chi_l^{(w)} \hat{M}_l} \sum_{j=1}^{N_s} \hat{M}_j D_{jm} \left( \chi_j^{(1)} - \chi_j^{(w)} \right) - \hat{M}_i D_{im} \left( \chi_i^{(1)} - \chi_i^{(w)} \right) - \frac{\Delta h/2}{\eta_t} \sum_{r=1}^{N_r} \omega_i^r = 0 \quad (62)$$

$$i = 1, 2, \dots, N_s,$$

where the superscript ( $w$ ) indicates evaluation at the wall, the superscript (1) indicates evaluation at the first cell center off the wall, and  $\Delta h/2$  is the distance between the wall boundary location and the first cell center. Here we have also substituted the relation

$$\frac{\rho_i}{\rho} = \frac{\chi_i \hat{M}_i}{\sum_{l=1}^{N_s} \chi_l \hat{M}_l}. \quad (63)$$

For fixed temperature and pressure, Eq (62) represents a  $N_s \times N_s$  nonlinear system of equations in terms of the wall mole fractions,  $\chi_i^{(w)}$ . The resulting system of equations is solved using Newton's method with an LU decomposition and forward/backward substitution that vectorizes over all points on the surface.

An overview of the catalytic wall boundary condition is as follows:

1. The wall temperature is fixed to  $T_w$ .
2. The wall pressure is computed from  $(\bar{\nabla} p)_w = 0$ .
3. For a fixed temperature and pressure, the nonlinear system given by Eq (62) is solved for the wall species' mole fractions,  $\chi_i^{(w)}$ . Starting values for the mole fractions are taken from the previous iteration's converged values.
4. The total number of moles at the wall,  $\eta_t^{(w)}$ , is computed from the thermally-perfect gas law,  $p = \eta_t \hat{R} T$ .
5. The wall species' concentrations are determined using  $\eta_i = \chi_i \eta_t$ .
6. The wall species' densities are determined using  $\rho_i = \eta_i \hat{M}_i$ .
7. The wall velocity components are set to zero, *i.e.*,  $u, v, w = 0$ .

Initial attempts to solve Eq (62) revealed that this system was ill-behaved. When solutions to the mass-balance system could be obtained, there was no mechanism to ensure that the sum of the mole fractions at the wall would be unity, *i.e.*,  $\sum \chi_i^{(w)} = 1$ . To satisfy this constraint, we introduced a penalty function to each mass balance equation of the form

$$\begin{aligned} & \text{minimize } \phi_i(\chi) = F_i(\chi) + r h^2(\chi) \\ & \text{such that } h(\chi) = 0 \\ & \text{where } h(\chi) = \sum \chi_i^{(w)} - 1. \end{aligned} \quad (64)$$

The penalty function associates a penalty with a violation of the constraint. Solutions of the augmented system appears to be well-behaved, satisfying both the initial system as well as the mole-fraction constraint. Note that  $r$  is a multiplier which, in the true sense of a penalty function method, is systematically increased from zero to some significant value during the iteration process. In our case we have successfully used  $r = 1$  during the entire iteration process.

## 7.2 Power-Off RADICL Simulations with Wall Catalysis

Two additional power-off RADICL simulations have been performed using GASP v4. These calculations utilized the surface catalysis reactions for the nozzle wall boundary conditions. The first calculation used the fully catalytic efficiencies used by Hishida [8]. The second calculation used the more realistic catalytic efficiencies suggested by Madden [9]. Both calculations were performed using the same flow conditions and grid system as the previously-described RADICL simulation (see Section 5.2).

Figure 20 shows the oxygen species' mass-fraction profiles at the start of the constant-area section upstream of the injectors (*i.e.*,  $x = 0.0$  in Figure 13) in the  $k = 5$  vertical plane. The vertical axis represents the  $y$  coordinate and starts at the symmetry plane (*i.e.*,  $y = 0.0$ ) and ends at the upper nozzle wall. Results are shown for the fully-catalytic efficiencies, the modified efficiencies, and the baseline case. At this location there is no iodine in the flow and the chemical composition is affected only by surface reactions 1 – 3.

Figures 20(a) and 20(b) show the mass-fraction profiles for the ground state of oxygen,  $O_2(^3\Sigma)$ . Figure 20(b) shows a close-up of the modified-efficiency case. Both catalytic cases predict higher

near-wall concentrations of  $O_2(^3\Sigma)$  compared to the baseline case. The mass-fraction gradient of  $O_2(^3\Sigma)$  at the wall for the catalytic cases indicates a diffusional flux away from the wall. This flux balances with the production of  $O_2(^3\Sigma)$  through surface deactivation reactions 2 and 3. As expected, the fully-catalytic efficiencies have a much greater impact on the near-wall concentration of  $O_2(^3\Sigma)$  compared to the modified-efficiency case.

Figures 20(c) and 20(d) show the mass-fraction profiles of the  $O_2(^1\Delta)$  state of oxygen. Figure 20(d) shows a close-up of the modified-efficiency case. Both catalytic cases predict lower near-wall concentrations of  $O_2(^1\Delta)$  compared to the baseline case. The diffusional flux of  $O_2(^1\Delta)$  toward the wall balances with the production and destruction of  $O_2(^1\Delta)$  through surface deactivation reactions 1 and 3. Although  $O_2(^1\Delta)$  is produced in surface reaction 1, this process is outweighed by reaction 3 and the net effect is to destroy  $O_2(^1\Delta)$  at the wall. Again, the fully-catalytic efficiencies have a much greater impact on the near-wall concentration of  $O_2(^1\Delta)$  compared to the modified-efficiency case.

Figures 20(e) and 20(f) show similar mass-fraction profiles of the  $O_2(^1\Sigma)$  state of oxygen. Both catalytic cases predict lower near-wall concentrations of  $O_2(^1\Sigma)$  compared to the baseline case, resulting from the fact that  $O_2(^1\Sigma)$  is destroyed through surface deactivation reactions 1 and 2.

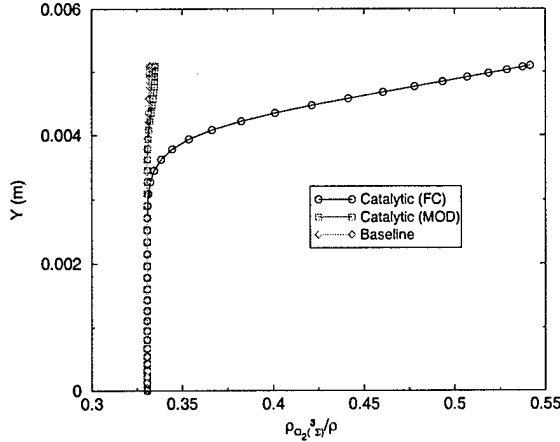
Figure 21 shows mass fraction profiles for each of the iodine species at the optical axis (*i.e.*,  $x = 0.11578m$  in Figure 13) in the  $k = 5$  vertical plane. Again, results are shown for the fully-catalytic efficiencies, the modified efficiencies, and the baseline case.

Figures 21(a) shows the mass-fraction profiles for the ground state of diatomic iodine,  $I_2$ . Both catalytic cases predict higher near-wall concentrations of  $I_2$  compared to the baseline case. The mass-fraction gradient of  $I_2$  at the wall for the catalytic cases indicates a diffusional flux away from the wall. This flux balances with the production of  $I_2$  through surface deactivation reaction 5 and recombination reactions 6 and 7. The core-flow concentration of  $I_2$  is significantly higher for the fully-catalytic case compared to the baseline and modified-efficiency calculations. In this case the very strong upstream catalytic effects have propagated into the core flow and altered the gas-phase chemical mechanisms. The lower upstream concentrations of  $O_2(^1\Sigma)$  and  $O_2(^1\Delta)$  lead to a reduction in the dissociation of  $I_2$  that occurs through gas-phase reactions 7 and 11. The net effect is to have more  $I_2$  in the core flow. Differences between the modified-efficiency and the baseline case are confined to the near-wall region.

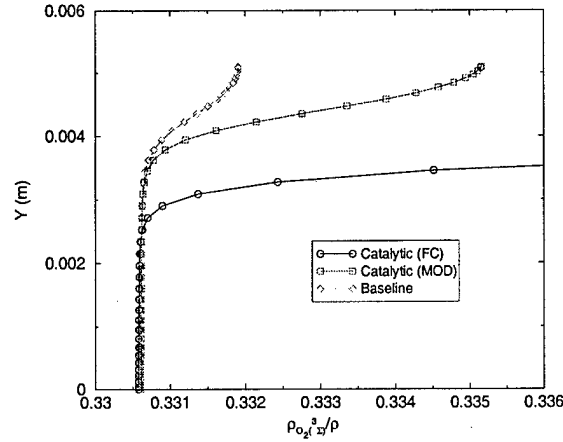
Figure 21(b) shows the mass-fraction profiles for the excited state of diatomic iodine,  $I_2^*$ . Both catalytic cases predict lower near-wall concentrations of  $I_2^*$  compared to the baseline case. The diffusional flux of  $I_2^*$  toward the wall balances with the destruction of  $I_2^*$  through surface deactivation reaction 5. Again, the core-flow concentration of  $I_2^*$  is significantly higher for the fully-catalytic case compared to the baseline and modified-efficiency calculations. The reason for the increased concentration of  $I_2^*$  is the reduction in amount of  $I_2$  dissociation (as described above) and therefore the overall increase in the amount of  $I_2$  available to become excited. Again, differences between the modified-efficiency and the baseline case are confined to the near-wall region.

Figure 21(c) shows the mass-fraction profiles for the ground state of monatomic iodine,  $I(^2P_{3/2})$ . Both catalytic cases predict lower near-wall concentrations of  $I(^2P_{3/2})$  compared to the baseline case. The mass-fraction gradient of  $I(^2P_{3/2})$  at the wall for the catalytic cases indicates a diffusional flux toward the wall. This flux balances with the production of  $I(^2P_{3/2})$  through surface deactivation reaction 4 and the destruction of  $I(^2P_{3/2})$  through surface recombination reaction 7. Note that surface reaction 7 dominates reaction 4 so that the net effect is to destroy  $I(^2P_{3/2})$  at the wall. The core-flow concentration of  $I(^2P_{3/2})$  is significantly lower for the fully-catalytic case compared to the baseline and modified-efficiency calculations. The reason for the reduced concentration of  $I(^2P_{3/2})$  is again the reduction in amount of  $I_2$  dissociation. Differences between the modified-efficiency and the baseline case are confined to the near-wall region.

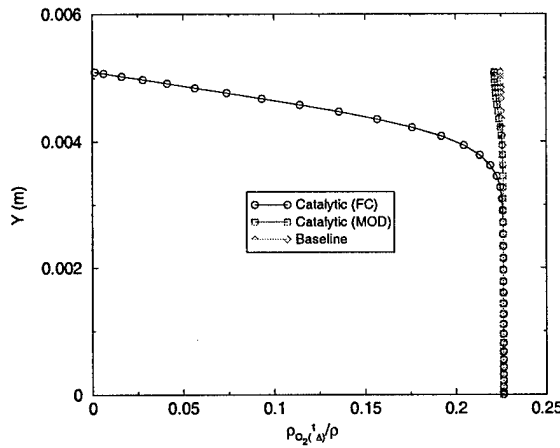
Figure 21(d) shows the mass-fraction profiles for the excited state of monatomic iodine,  $I(^2P_{1/2})$ . Both catalytic cases predict lower near-wall concentrations of  $I(^2P_{1/2})$  compared to the baseline case. The diffusional flux of  $I(^2P_{1/2})$  toward the wall balances with the destruction of  $I(^2P_{1/2})$  through surface deactivation reaction 4 and surface recombination reaction 6. The core-flow concentration of  $I(^2P_{1/2})$  is significantly lower for the fully-catalytic case because of the reduction in the amount of  $I_2$  dissociation. Again, differences between the modified-efficiency and the baseline case are confined



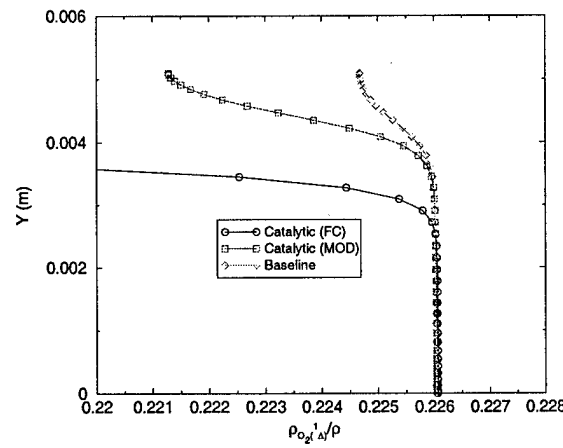
(a)  $O_2(3\Sigma)$  mass fractions.



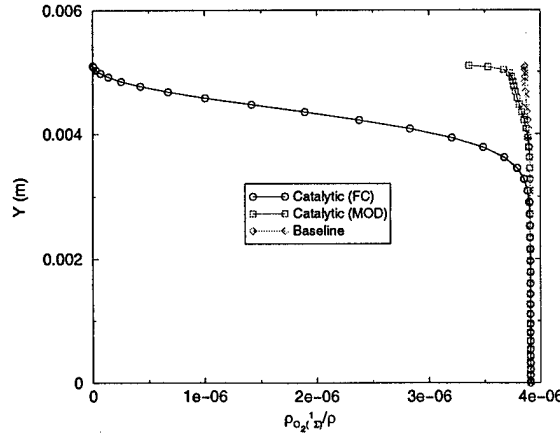
(b) Close-up of  $O_2(3\Sigma)$  mass fractions.



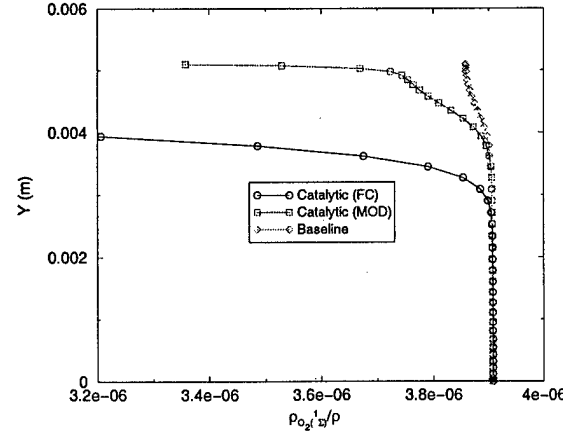
(c)  $O_2(1\Delta)$  mass fractions.



(d) Close-up of  $O_2(1\Delta)$  mass fractions.



(e)  $O_2(1\Sigma)$  mass fractions.



(f) Close-up of  $O_2(1\Sigma)$  mass fractions.

Figure 20: Oxygen species' mass fraction distributions at the start of the constant area section upstream of the RADICL injectors ( $x = 0.0\text{ m}$ ).

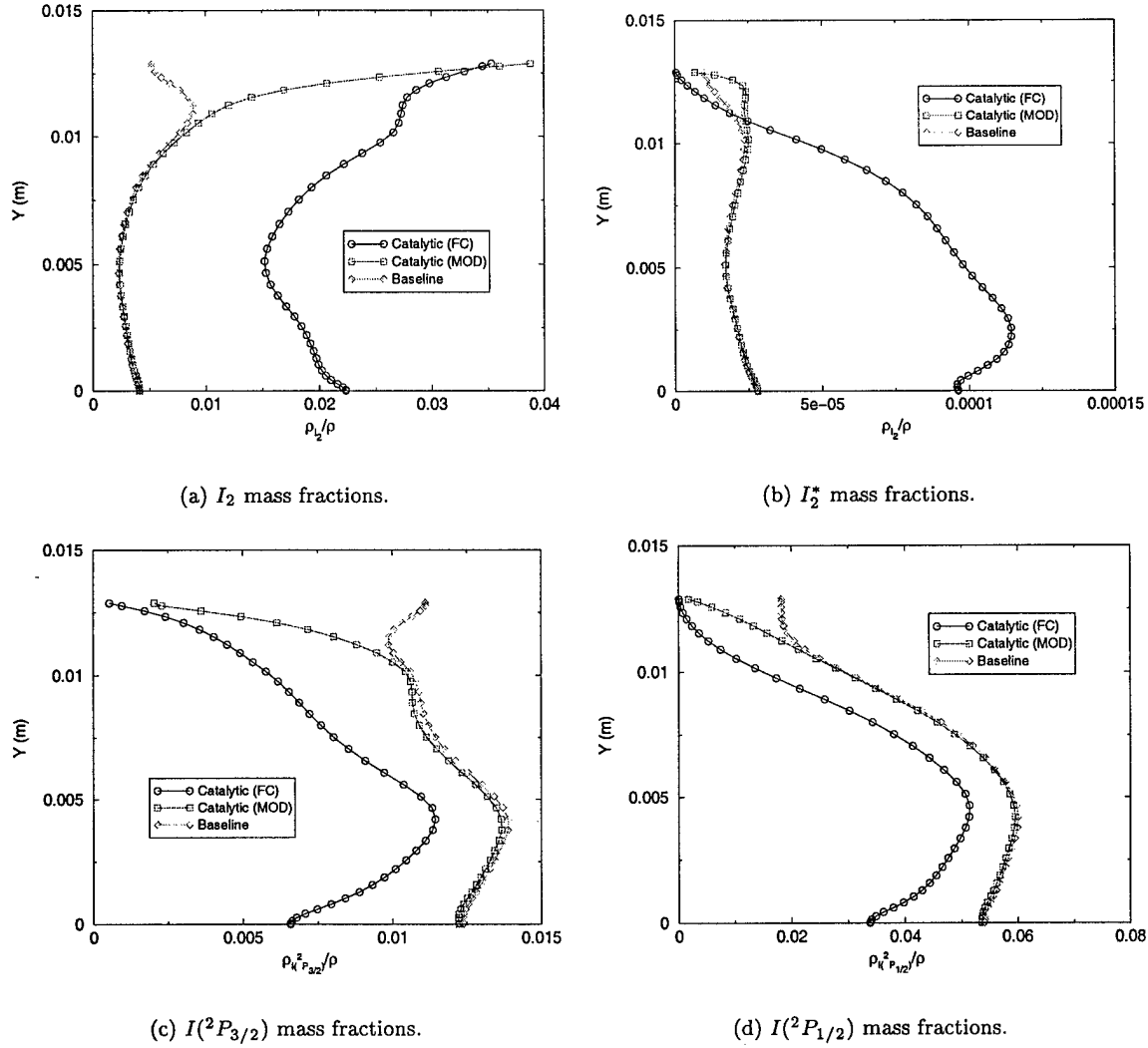


Figure 21: Iodine species' mass fraction distributions at the RADIICL optical axis ( $x = 0.11578m$ ).

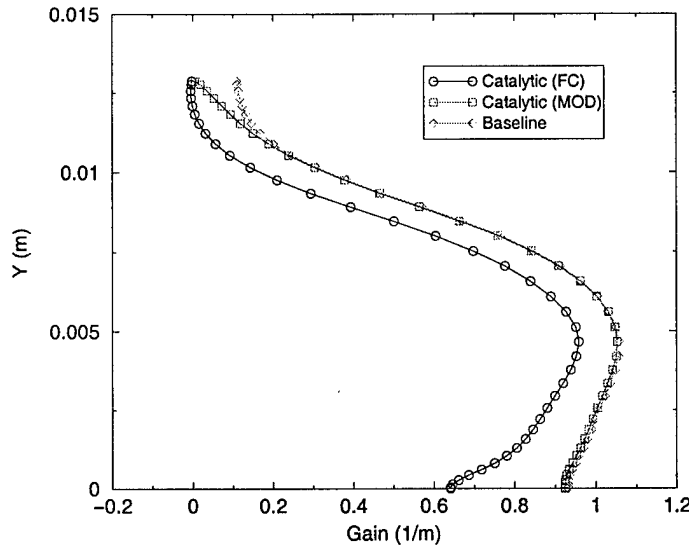


Figure 22: Gain distribution ( $1/m$ ) at the RADICL optical axis ( $x = 0.11578m$ ).

more to the near-wall region.

Figure 22 shows the gain profiles at the optical axis ( $x = 0.11578m$ ) in the  $k = 5$  vertical plane. Both catalytic cases predict lower values of gain compared to the baseline case. The differences between the modified-efficiency and the baseline case is confined to the near-wall region while the fully-catalytic case effects the gain in the core flow. Because the gain is a measure of the flow's photon extraction potential, we would expect a reduction in the output power for the wall-catalysis cases. This effect will be much larger for the fully-catalytic case.

### 7.3 Power-On RADICL Simulation with Water-Vapor Condensation and Wall Catalysis

A power-on RADICL simulation has been performed with both water-vapor condensation and surface catalysis. The simulation considered the same 5 droplet classes as described in the previous power-off condensation case and the modified efficiencies were utilized for the surface catalysis reactions. Nozzle and injector inflow conditions were the same as the previous cases. The unit-cell approximation was again employed with the same grid topology.

The aperture (and associated mirror system) was located between  $x = 0.08578m$  and  $x = 0.14578m$ . The length of the aperture was  $L_a = 0.06m$ . The distance between the spherical mirror and the flat out-coupling mirror is  $D_m = 0.8m$  and the radius of curvature of the spherical mirror is  $r_2 = 10.0m$ . The coefficients of reflectivity are  $R_1 = 0.927$  and  $R_2 = 0.995$  for the flat out-coupler and spherical mirrors respectively. The gain length was taken as  $L_g = 0.254m$  (the lateral width of the nozzle). Distributed losses in the gain medium and diffractive losses at the aperture were neglected. The polar mesh size for the ray-tracing algorithm was  $101 \times 41$  and the laser optics resonator model was called on every third flow-solver iteration. A baseline power-on solution has been run for this case without condensation and surface catalysis and results have been presented in Eppard [4] (see Section 5.2).

The laser power output predicted for the baseline simulation was  $P = 7.524\text{ KW}$ . With condensation and surface catalysis the simulated power output was  $P = 6.538\text{ KW}$ ; a 13% reduction in power due to the combined effects of condensation and surface catalysis. The experimentally measured value of power was  $P = 5.8\text{ KW}$ . Our results are in reasonable agreement with experiment, since no optical loss terms were included. Similar studies (*e.g.*, Buggeln [1]) have used non-zero values for mirror scattering and diffractive losses to give corrected output powers that are up to 20%

lower than the zero-loss power. Assuming similar behavior for this case, our power results are in good agreement with the measured value. The results of this study were presented in Eppard [3].

## 8 COIL Sensitivity Analysis

The sensitivity implementation in SENSE is fundamentally based on implicit-differentiation applied to the boundary-value problem describing the fluid mechanics. That is, one envisions an implicit equation

$$\mathcal{R}(\mathbf{Q}, \beta) = 0, \quad (65)$$

where  $\mathbf{Q}$  denotes the distributed dependent variables (*e.g.* density, momentum, energy) and  $\beta$  denotes a design variable. In common terminology  $\mathbf{Q}$  is known as the state and  $\beta$  as the design parameter. For fixed  $\beta$ , Eq (65) is solved for  $\mathbf{Q}$ . This defines a map

$$\beta \rightarrow \mathbf{Q},$$

which associates a flow solution with the specified design parameter(s). The sensitivity is the derivative of this map; it provides a linear approximation for how the flow solution will change under a small change in the design parameter. One proceeds by formally differentiating Eq (65) to produce

$$\frac{\partial \mathcal{R}}{\partial \mathbf{Q}} \frac{\partial \mathbf{Q}}{\partial \beta} + \frac{\partial \mathcal{R}}{\partial \beta} = 0. \quad (66)$$

The SENSE code implements a numerical approximation to Eq (66) for situations wherein  $\mathcal{R}$  models Reynolds-Averaged Navier-Stokes flows with finite-rate chemistry.

The integral equations for the fluid dynamic system are written as

$$\frac{\partial}{\partial t} \iiint \mathbf{Q} dV + \oint_A (\mathbf{F}(\mathbf{Q}) \cdot \hat{\mathbf{n}}) dA = \oint_A (\mathbf{F}_v(\mathbf{Q}) \cdot \hat{\mathbf{n}}) dA + \iiint \mathbf{S} dV, \quad (67)$$

where  $\mathbf{Q} = \mathbf{Q}(x, y, z, t; \beta)$  represents the vector of state variables resulting from conservation of mass, momentum and energy. The surface integrals represent the inviscid and viscous fluxes ( $\mathbf{F}$  and  $\mathbf{F}_v$ ). Changes in chemical composition are governed by the species production terms in the source term  $\mathbf{S}$ . Formal differentiation of Eq (67) with respect to the generic design parameter,  $\beta$ , results in the sensitivity equations. These equations are linear in the sensitivities. Presented in integral form, they are

$$\frac{\partial}{\partial t} \iiint \mathbf{Q}' dV + \oint_A (\mathbf{F}'(\mathbf{Q}) \cdot \hat{\mathbf{n}}) dA = \oint_A (\mathbf{F}'_v(\mathbf{Q}) \cdot \hat{\mathbf{n}}) dA + \iiint \mathbf{S}' dV, \quad (68)$$

where  $\mathbf{Q}'$  is the flow sensitivity, *i.e.*,  $\partial \mathbf{Q} / \partial \beta$ . The inviscid and viscous flux sensitivities,  $\mathbf{F}'$  and  $\mathbf{F}'_v$ , and the source term sensitivity,  $\mathbf{S}'$ , are formally given as

$$\mathbf{F}' = \frac{\partial \mathbf{F}}{\partial \mathbf{Q}} \frac{\partial \mathbf{Q}}{\partial \beta}, \quad \mathbf{F}'_v = \frac{\partial \mathbf{F}_v}{\partial \mathbf{Q}} \frac{\partial \mathbf{Q}}{\partial \beta}, \quad \mathbf{S}' = \frac{\partial \mathbf{S}}{\partial \mathbf{Q}} \frac{\partial \mathbf{Q}}{\partial \beta}. \quad (69)$$

SENSE solves Eq (68) using an upwind characteristic-based formulation.

### 8.1 Sensitivities for the Effective Diffusion Model

As a first step toward tailoring SENSE for COIL-laser applications, AeroSoft has extended the viscous sensitivity formulation to include the effective diffusion model. This task required modifying the species diffusive flux sensitivity terms which are given as

$$\mathbf{F}'_v = -\frac{\partial}{\partial \beta} \left( \rho_s \vec{v}_s \cdot \mathbf{n} \right), \quad (70)$$

where the diffusion velocity is determined by Eqs (16) (19) and (20). The sensitivity formulation proceeds by formally differentiating Eqs (19) and (20) with respect to the design variable, yielding

$$\left(\rho_s \vec{V}_s^\chi\right)' = -\gamma_t' \left[ \mathbf{G}_s^\chi - \frac{\rho_s}{\rho} \sum_{j=1}^N \mathbf{G}_j^\chi \right] - \gamma_t \left[ \mathbf{G}_s^{\chi'} - \frac{1}{\rho} \left( \rho'_s - \frac{\rho_s}{\rho} \rho' \right) \sum_{j=1}^N \mathbf{G}_j^\chi - \frac{\rho_s}{\rho} \rho' \sum_{j=1}^N \mathbf{G}_j^{\chi'} \right], \quad (71)$$

and

$$\begin{aligned} \left(\rho_s \vec{V}_s^p\right)' &= -\gamma_t' \left[ \mathbf{G}_s^p - \frac{\rho_s}{\rho} \sum_{j=1}^N \mathbf{G}_j^p \right] \frac{\bar{\nabla} p}{p} - \gamma_t \left[ \mathbf{G}_s^{p'} - \frac{1}{\rho} \left( \rho'_s - \frac{\rho_s}{\rho} \rho' \right) \sum_{j=1}^N \mathbf{G}_j^p - \frac{\rho_s}{\rho} \rho' \sum_{j=1}^N \mathbf{G}_j^{p'} \right] \frac{\bar{\nabla} p}{p} \\ &\quad - \gamma_t \left[ \mathbf{G}_s^p - \frac{\rho_s}{\rho} \sum_{j=1}^N \mathbf{G}_j^p \right] \left( -\frac{\bar{\nabla} p}{p^2} p' + \frac{\bar{\nabla} p'}{p} \right), \end{aligned} \quad (72)$$

where

$$\left(\rho_s \vec{V}_s\right)' = \left(\rho_s \vec{V}_s^\chi\right)' + \left(\rho_s \vec{V}_s^p\right)'. \quad (73)$$

The individual sensitivity terms for the species concentration, the mixture concentration, and the species mole fraction are given as

$$\gamma'_s = \frac{\rho'_s}{\hat{M}_s}, \quad \gamma'_t = \sum_{s=1}^N \gamma'_s, \quad \chi'_s = \frac{1}{\gamma_t} \left( \frac{\rho'_s}{\hat{M}_s} - \chi_s \cdot \gamma'_t \right). \quad (74)$$

The sensitivities of  $\mathbf{G}_s^\chi$ ,  $\mathbf{G}_s^p$ , and  $D_{sm}$  are

$$\mathbf{G}_s^{\chi'} = \hat{M}_s D'_{sm} \bar{\nabla} \chi_s + \hat{M}_s D_{sm} \bar{\nabla} \chi'_s, \quad (75)$$

$$\mathbf{G}_s^{p'} = \hat{M}_s D'_{sm} \left( \chi_s - \frac{\rho_s}{\rho} \right) + \hat{M}_s D_{sm} \left( \chi'_s - \frac{\rho'_s}{\rho} + \frac{\rho_s}{\rho^2} \rho' \right), \quad (76)$$

and

$$D'_{sm} = -\frac{D_{sm}}{1 - \chi_s} \left[ \chi'_s + D_{sm} \sum_{j=1, j \neq s}^N \left( \frac{\chi_j}{D_{sj}} - \frac{\chi_j}{D_{sj}^2} D'_{sj} \right) \right]. \quad (77)$$

Finally, closure of the effective diffusion sensitivity terms is given by sensitivities of the binary diffusion coefficient

$$D'_{ij} = D_{ij} \left( \frac{3}{2} \frac{T'}{T} - \frac{\Omega'_{ij}}{\Omega_{ij}} - \frac{p'}{p} \right), \quad (78)$$

where

$$\Omega'_{ij} = - \left[ \frac{0.06606}{T^{*1.08742}} + \frac{0.57901}{T^{*1.84910}} \right] T^{*'}, \quad (79)$$

and

$$T^{*'} = \frac{T'}{\epsilon_{ij}}. \quad (80)$$

The sensitivity relations given by Eqs (71) - (80) along with the corresponding flux-sensitivity Jacobian terms have been added to a COIL version of the SENSE software. A simplified helium-iodine chemistry model has also been added to the SENSE package.

## 8.2 Sensitivities of Helium-Iodine Injection

The sensitivity analysis has been applied to the helium-iodine injection case described in Section 3.1. For this case the design variable was chosen to be the jet iodine density, *i.e.*,  $\beta = \rho_{I_2}^{jet}$ . Figures 23(a) and 23(b) show the iodine mass fractions from the GASP calculation and the iodine mass-fraction sensitivities,  $(\rho_{I_2}/\rho)'$  from SENSE. The iodine mass-fraction sensitivities at the injector face are imposed by the jet inflow densities and density sensitivities through the following relation

$$\left(\frac{\rho_{I_2}}{\rho}\right)' = \frac{1}{\rho} \left( \rho'_{I_2} - \frac{\rho_s}{\rho} \rho' \right). \quad (81)$$

The jet helium and mixture densities are  $\rho_{I_2} = 0.034737 \text{ Kg/m}^3$  and  $\rho = .082217 \text{ Kg/m}^3$ . The jet helium and mixture density sensitivities are unity for this case. Under these conditions Eq (81) gives a value of  $(\rho_{I_2}/\rho)' = 7.024$ ; the free-stream value observed in Fig 23(b). The iodine mass-fraction sensitivities are observed to have values larger than  $(\rho_{I_2}/\rho)' = 7.024$  near the injector side-wall regions. This indicates that the pressure-diffusion effects become more pronounced as the iodine density in the jet increases. To see that this is plausible, we analyze the leading pressure-gradient term in Eq (15),  $(\chi_{I_2} - \rho_{I_2}/\rho)$ . For a 5% increase in the design variable the absolute value of this term increases from  $|(\chi_{I_2} - \rho_{I_2}/\rho)| = 0.387750$  to a value of  $|(\chi_{I_2} - \rho_{I_2}/\rho)| = 0.397994$  (a 2.64% increase). As a result the pressure diffusion effects should become more pronounced. Figure 24(a) shows iodine mass fraction sensitivities along the  $i = 10$  grid line for both SENSE and a central difference approximation using GASP and a 5% change in design variable. The two profiles agree very well and both predict an increase in the iodine mass fraction near injector side wall. Figure 24(b) shows a close up of iodine mass fraction profiles for the baseline solution, a GASP solution for a 5% increase in  $\beta$ , and a Taylor's series projection using the baseline flow and the sensitivities from SENSE. The projected solution agrees very well with the "exact", GASP solution, except for the slight lag near the start of the large pressure-gradient region.

## 8.3 Sensitivities of Transverse Helium-Iodine Injection

The sensitivity analysis has also been applied to the transverse helium-iodine injection case described in Section 3.2. For this case the design variable was chosen to be the jet velocity, *i.e.*,  $\beta = V^{jet}$ . Figure 25(a) shows the iodine mass fractions from the GASP calculation and Fig 25(b) shows the iodine mass-fraction and velocity-vector sensitivities. The velocity-vector sensitivities indicate an increase in the jet velocity as well as deeper penetration of the helium-iodine mixture into the primary flow. The iodine mass-fraction sensitivities also indicate that the jet flow has penetrated further into the primary flow. The region of positive (and negative) sensitivities just above (and below) the jet indicate that the jet has shifted upward. The portion of the recirculation region with low iodine mass fractions has also shifted upward, as indicated by the positive sensitivities in this area.

## 8.4 Simple Power-On Test Case

Power-on flow simulations have been performed for a simplified geometry, but with flow conditions and optical parameters consistent with the RADICL laser. This test problem was used to debug and demonstrate the flow coupling with the laser optics resonator model. The same problem will be used to test the COIL sensitivity package and is described below.

Figure 26(a) shows the grid topology for the  $151 \times 51$  flow-solver mesh and the  $101 \times 51$  polar optics mesh. The number of grid points shown in this figure has been reduced to facilitate viewing. Notice that the x-direction stretching at the leading and trailing edges of the optics mesh is nearly identical to the flow solver mesh. The start of the aperture is at  $x = .06 \text{ m}$  and the aperture length is  $L_a = .05 \text{ m}$ . The aperture height is  $H_a = .028 \text{ m}$ . The distance between the curved mirror and the flat out-coupling mirror is  $D_m = 0.8 \text{ m}$  and the radius of curvature of the curved mirror is  $r_2 = 10.0 \text{ m}$ . The coefficients of reflectivity for the mirrors are  $R_1 = 0.90$  and  $R_2 = 0.99$ .

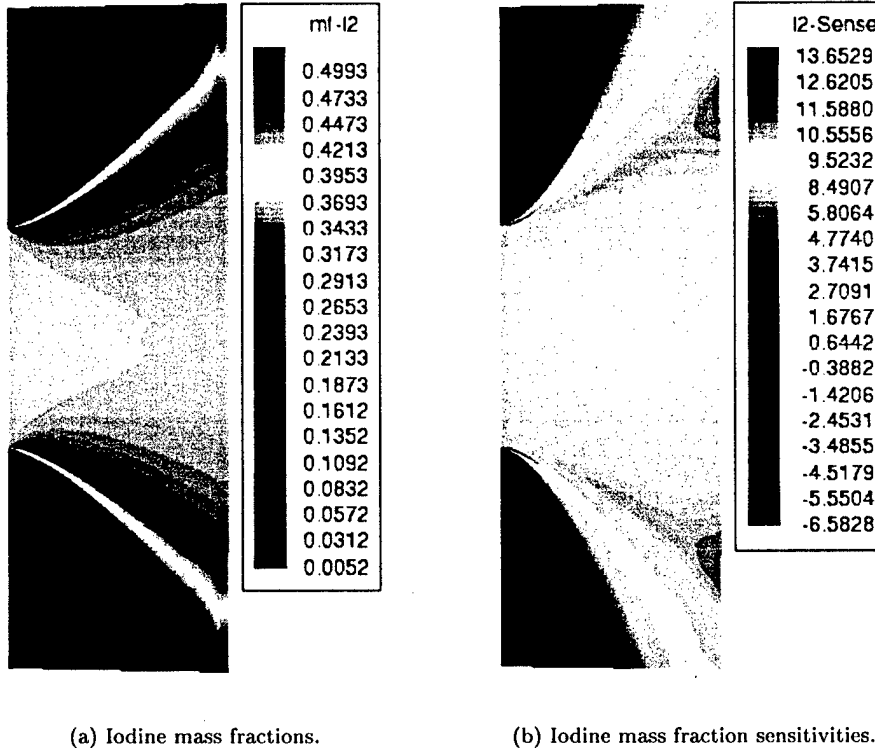


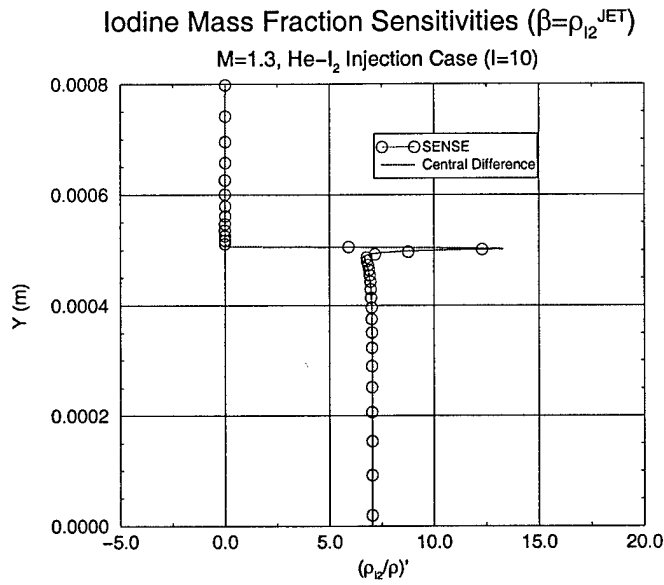
Figure 23: Sensitivities for Helium-iodine injection.

for the out-coupler and curved mirrors respectively. The gain length was taken as  $L_g = 0.25\text{ m}$ . Distributed losses in the gain medium and diffractive losses at the aperture were neglected. The inflow boundary was split into two portions; with the lower stream having a high concentration of  $I^*$  (high-gain region), and an upper stream with very little  $I^*$  and  $O_2(^1\Delta)$  (low-gain region). The low-gain region was designed to account for the region of low gain observed near the upper wall in the power-off RADICL simulations. The inflow conditions for the test case were chosen from actual conditions (upstream of the lasing cavity) for the power-off RADICL simulation, and are listed in Table 3.

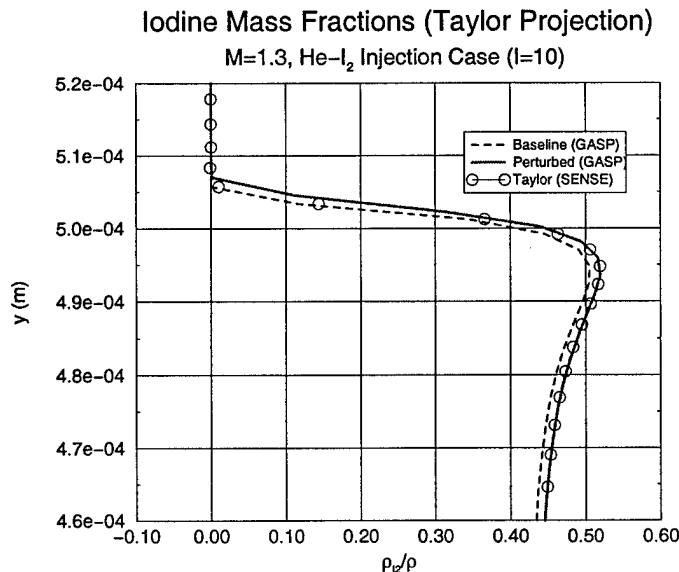
Figures 26(b) and 26(c) show the gain and intensity contours for this simulation. Values for the inflow gain in the high and low-gain regions are approximately  $\alpha = 1.065\text{ 1/m}$  and  $\alpha = 0.00751\text{ 1/m}$  respectively. The maximum gain occurs in the high-gain region just before the start of the aperture and has a value of  $\alpha_{max} = 1.308\text{ 1/m}$ . Past the start of the aperture, the gain is dramatically reduced through interaction with the lasing source terms. The maximum intensity occurs at the aperture leading and trailing edges with a value of  $I_{max} = 3.6 \times 10^9\text{ W/m}^2$ . The power output for this case converged after approximately 1000 iterations and was  $P = 13.1\text{ KW}$ .

#### 8.4.1 Power-Off Sensitivity Analysis

In this section we test the newly-implemented COIL chemistry and thermodynamics sensitivity models. We consider the simple geometry described above, but with the laser turned off. In this case, the design variable is the free-stream density of  $O_2(^1\Delta)$  in the lower stream. Figure 27(a) shows the gain contours along the lasing cavity. Figure 27(b) shows the gain distribution along the  $j = 10$  gridline (midway in the lower stream). The gain initially increases due to chemical reactions and reaches a peak value of  $\alpha = 1.32\text{ 1/m}$ . Because of the heat release of the chemical reactions, and because the flow is does not expand, the temperature increases causing the gain to decrease as the flow continues downstream. In our sensitivity analysis we seek to find out how the gain changes

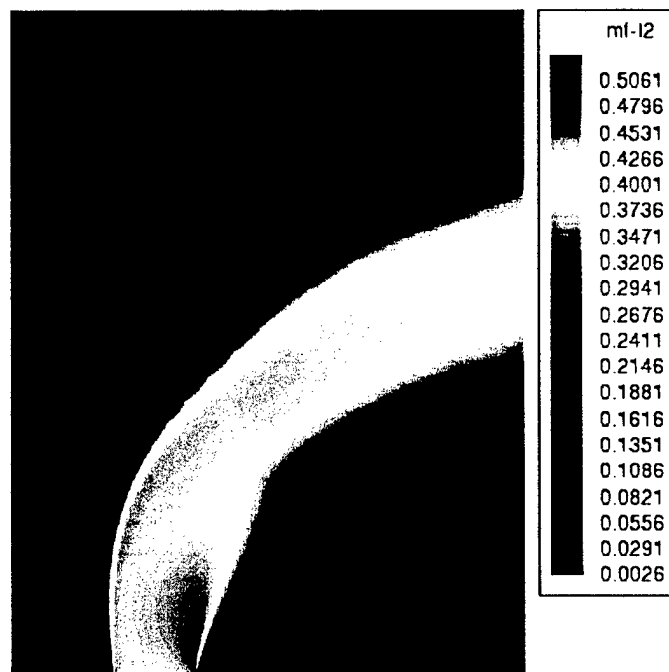


(a) Iodine mass fraction sensitivities (station I=10).

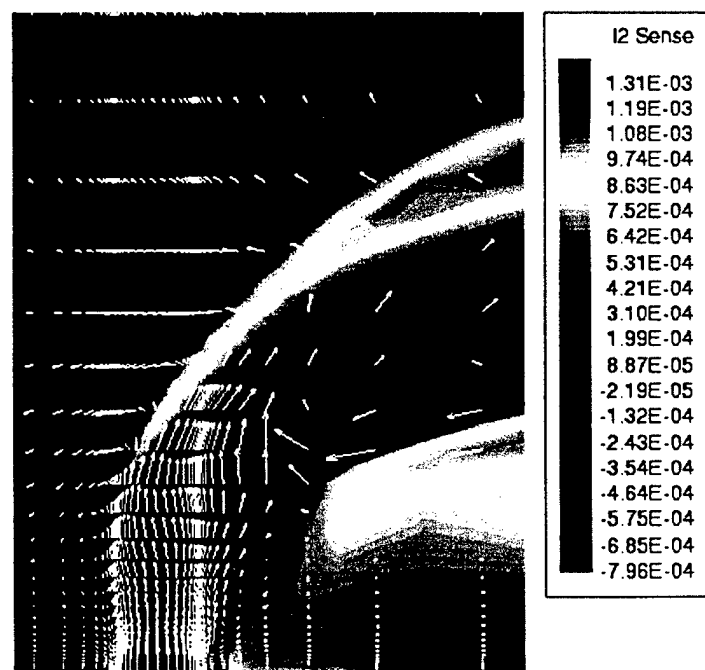


(b) Projected iodine mass fractions for 5% increase in  $\beta$  (Close up).

Figure 24: Sensitivities and Taylor projection for helium-iodine injection.

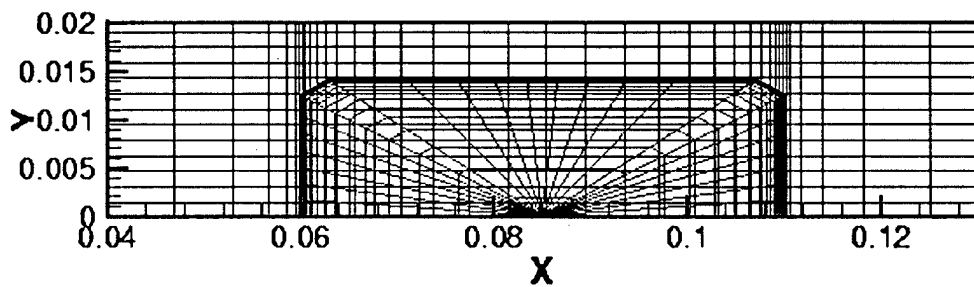


(a) Iodine mass fractions.

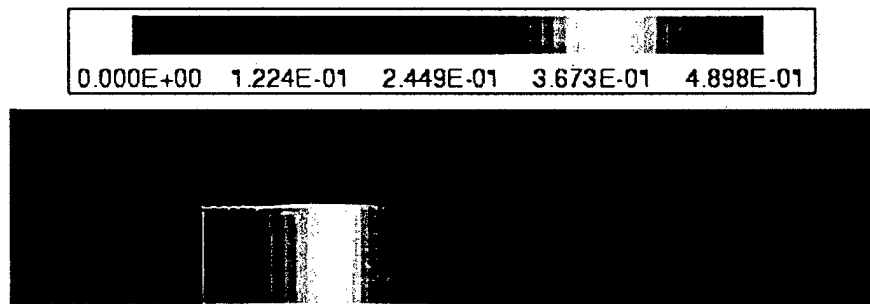


(b) Iodine mass-fraction and velocity-vector sensitivities.

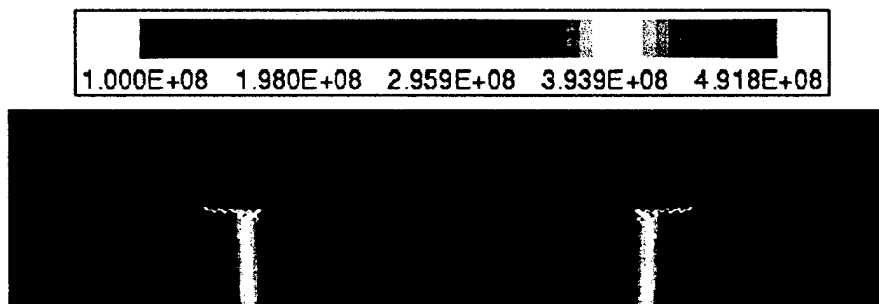
Figure 25: Sensitivities for transverse helium iodine injection.



(a) Coarsened flow-solver mesh and polar optics mesh.



(b) Gain contours ( $1/m$ ).



(c) Intensity contours ( $Watts/m^2$ ).

Figure 26: Simple test case grid system and gain ( $1/m$ ) and intensity ( $Watts/m^2$ ) contours.

No.	Reaction	$K_f (Kg - mole, m^3, s)$
10	$I_2 + I^* \rightarrow I_2^* + I$	$2.288 \times 10^{10}$
11	$I_2^* + O_2(^1\Delta) \rightarrow 2I + O_2(^3\Sigma)$	$1.807 \times 10^{11}$
20	$I^* + H_2O \rightarrow I + H_2O$	$1.204 \times 10^9$

Table 5: Partial reaction list, 10-species, 20-reaction COIL chemistry model

with an increase in the inflow density of  $O_2(^1\Delta)$  in the lower stream. Figure 27(c) shows the gain sensitivity distribution along the  $j = 10$  gridline for the SENSE code and for a central difference calculation using GASP v4. The CSEM results are in very good agreement with central difference.

#### 8.4.2 Power-Off Reaction Rate Sensitivity Analysis

In CFD simulations involving finite-rate chemistry, there always exists some question concerning the accuracy of the reaction-rate coefficients. Small variations in these coefficients can translate into significant changes in the thermo-chemical state of the flow, affecting distributions of temperature, pressure and other flow variables. In the COIL laser, chemical reactions affect the lasing-cavity temperature, which in turn affects the small-signal gain and lasing efficiency. Knowing *a priori* which reaction-rate coefficients have the largest effect on laser performance will allow chemists to prioritize and possibly narrow their refinement efforts. To study this effect, AeroSoft has implemented into SENSE the capability to compute flow-field sensitivities to the Arrhenius reaction-rate coefficients. The Arrhenius rates are given as

$$K_f = c T^\eta e^{-\epsilon/kT}. \quad (82)$$

In the new formulation any of the Arrhenius coefficients can be selected as the design variable. For instance, if the design variable were chosen to be the Arrhenius coefficient  $c$ , the source term,  $\mathbf{S}'$ , would include a term like

$$\frac{\partial K_f}{\partial \beta} = \left( \eta + \frac{\epsilon}{kT} \right) \frac{K_f}{T} T' + \frac{1}{c} K_f. \quad (83)$$

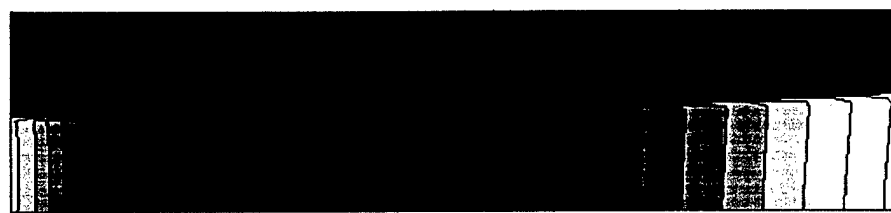
In this case the second term on the right-hand side of Eq (83) would drive the sensitivity problem and solutions to this system of equations will yield flow-field sensitivities to the Arrhenius coefficient  $c$ .

An analysis of each of the reactions in the COIL model for the simple test geometry shows that the  $c$  coefficient for reactions 10, 11, and 20 have the largest affect on the gain. The corresponding reactions are listed in Table 5. Figure 28 shows the gain sensitivity along the  $j = 10$  gridline for each of these reactions. Again the CSEM and central difference sensitivities are in good agreement.

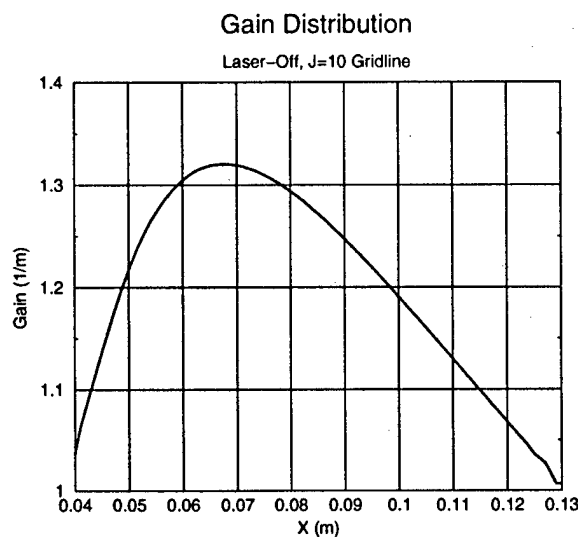
#### 8.4.3 Power-On Sensitivity Analysis (Constant Intensity)

The CFD/LOR coupling occurs through laser power extraction terms. Power extraction in the lasing cavity manifests itself in the form of source terms in the iodine species continuity equations, and in the global energy equation. The species continuity equations are affected because components at different energy states are represented as separate species. In a COIL laser, iodine in the excited,  $I(^2P_{1/2})$ , energy state is stimulated to emit photons (*i.e.*, stimulated emission). Upon emission of the photon, the iodine atom assumes the lower,  $I(^2P_{3/2})$ , energy state. As a result, power extraction affects the concentration of these two states. Power extraction also accounts for a net energy loss (through emission of photons) to the flow. The modified species continuity equation is given by Eq (23), where the last term on the right-hand side of the power-extraction source term. The source term is composed of the gain,  $\alpha$ , the *two-way* average intensity,  $\hat{I}$ , the molecular weight,  $M_s$ , and the energy of a photon,  $h\nu = 90956 \text{ J/g-mole}$ . The plus sign for the lasing source term in Eq (23) is used for the ground state of iodine and the minus sign is used for the excited state. No other species

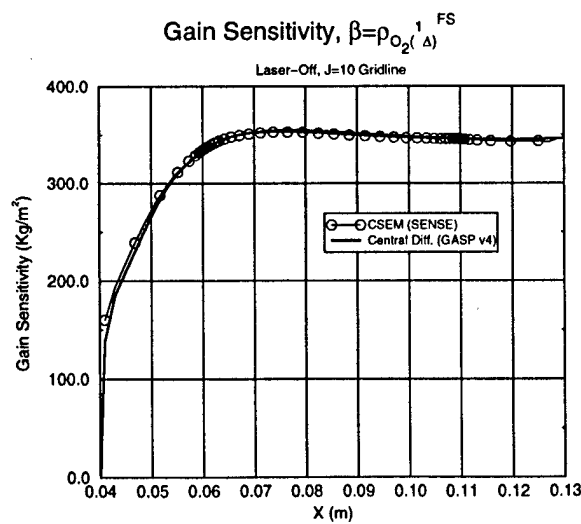
3.298E-02 3.426E-01 6.522E-01 9.618E-01 1.271E+00



(a) Gain contours ( $1/m$ ).



(b) Gain distribution ( $1/m$ ),  $j = 10$  gridline.



(c) Gain sensitivity profiles ( $kg/m^2$ ),  $j = 10$  gridline.

Figure 27: Gain and gain sensitivity profiles for the simple test case with power off.

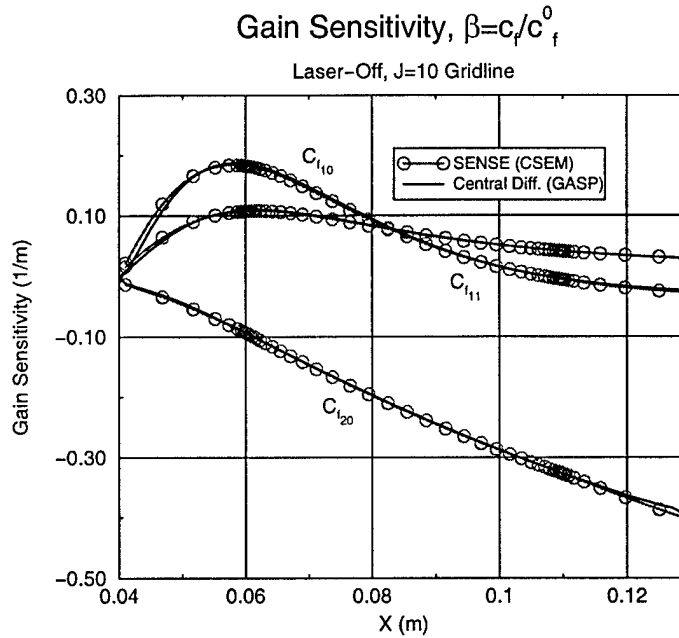


Figure 28: Gain sensitivity,  $j = 10$  gridline

in the model has a source term contribution from power extraction. The global energy equation has a similar source term,  $-\alpha I$ , to account for the energy removed from the flow.

Similarly, the power extraction sensitivity source terms take the form

$$\left( \frac{\alpha \hat{I} \hat{M}_s}{h\nu} \right)' = \frac{\alpha' \hat{I} \hat{M}_s}{h\nu} + \frac{\alpha \hat{I}' \hat{M}_s}{h\nu}. \quad (84)$$

In this section we test a portion of the new COIL source term sensitivities for the simple geometry described above. Here we assume the two-way intensity in the lasing cavity has a constant value of  $\hat{I} = 1.5 \times 10^8 \text{ Watts/m}^2$ . In this case, the second term on the right-hand-side of Eq (84) is identically zero.

Again, the design variable is the free-stream density of  $O_2(^1\Delta)$  in the lower stream. Figure 29(a) shows the gain contours along the lasing cavity. Figure 29(b) shows the gain distribution along the  $j = 10$  gridline. Past the start of the aperture, the gain is dramatically reduced through interaction with the lasing source terms. Figure 29(c) shows the gain sensitivity distribution along the  $j = 10$  gridline for the SENSE code with COIL source terms, and for a central difference calculation using GASP v4. The CSEM results are in very good agreement with central difference.

## 9 Coupled Sensitivity Analysis

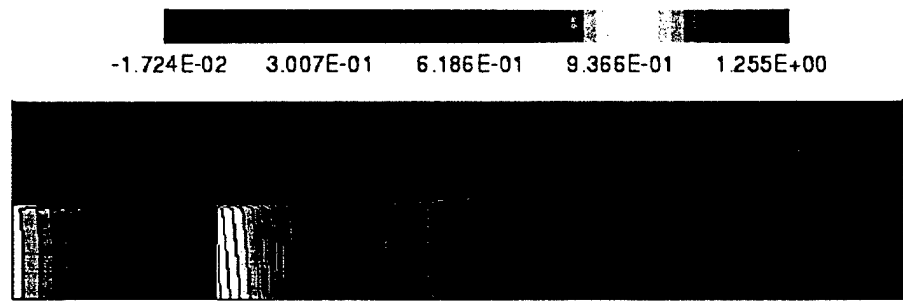
We now wish to extend the sensitivity analysis of the previous sections to fully include the coupled CFD/optics model. Specifically, we seek a solution methodology for the linear problem of Eq (66) when the residual, *i.e.*, Eq (65), is a coupled system involving several disciplines.

We begin with the implicitly-coupled system and generic design variable  $\beta$  as follows

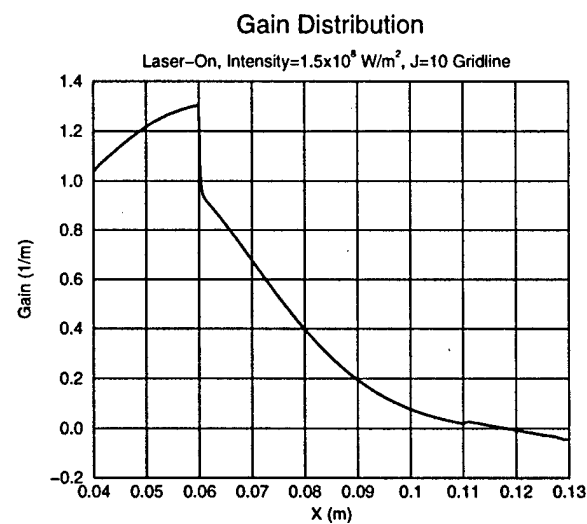
$$\mathcal{R}_f(u_f, u_p, \beta) = 0 \quad (85)$$

$$\mathcal{R}_p(u_f, u_p, \beta) = 0. \quad (86)$$

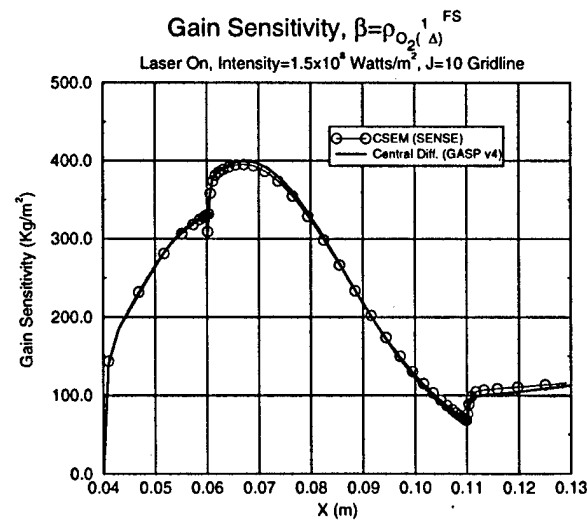
Here  $u_f$  variable describes the fluid *state* and the  $u_p$  variable describes laser-power *state*.



(a) Gain contours ( $1/m$ ).



(b) Gain profile ( $1/m$ ),  $j = 10$  gridline.



(c) Gain sensitivity profiles,  $j = 10$  gridline.

Figure 29: Simple test case gain and gain sensitivity for a constant intensity of  $\hat{I} = 1.5 \times 10^8$  Watts/m $^2$ .

The corresponding coupled sensitivity equation is described by the system

$$\begin{bmatrix} \frac{\partial \mathcal{R}_f}{\partial u_f} & \frac{\partial \mathcal{R}_f}{\partial u_p} \\ \frac{\partial \mathcal{R}_p}{\partial u_f} & \frac{\partial \mathcal{R}_p}{\partial u_p} \end{bmatrix} \cdot \begin{pmatrix} \frac{\partial u_f}{\partial \beta} \\ \frac{\partial u_p}{\partial \beta} \end{pmatrix} = - \begin{pmatrix} \frac{\partial \mathcal{R}_f}{\partial \beta} \\ \frac{\partial \mathcal{R}_p}{\partial \beta} \end{pmatrix}. \quad (87)$$

One approach to the coupled sensitivity problem builds on the existing SENSE software by employing a Jacobi or Gauss-Seidel iterative procedure to the coupled system (87).

An alternative formulation begins with an explicit representation of the laser field replacing (86) with

$$u_p = \mathcal{H}(u_f, \beta) \quad (88)$$

The laser optics resonator model can be viewed as a method for (approximately) evaluating the function  $\mathcal{H}$ . If this explicit representation is substituted into (136) we obtain

$$\mathcal{R}_f(u_f, \mathcal{H}(u_f, \beta), \beta) = 0. \quad (89)$$

This result can, in turn, be implicitly differentiated to yield the coupled flow-sensitivity equation

$$\left[ \frac{\partial \mathcal{R}_f}{\partial u_f} + \frac{\partial \mathcal{R}_f}{\partial u_p} \cdot \frac{\partial \mathcal{H}}{\partial u_f} \right] \cdot \frac{\partial u_f}{\partial \beta} + \left[ \frac{\partial \mathcal{R}_f}{\partial u_p} \cdot \frac{\partial \mathcal{H}}{\partial \beta} + \frac{\partial \mathcal{R}_p}{\partial \beta} \right] = 0. \quad (90)$$

Thus far, we have provided two forms for the sensitivity calculation: Eq (87) based on a general implicitly-coupled formulation; and, Eq (90) for a partially-explicit formulation. The structure suggested by the ray-tracing algorithm is an admixture of these.

Conceptually there are several distinct intensity fields represented in the optics model.

1. an *initial* intensity field represented by  $\hat{I}_0$ ,
2. a *return* intensity field represented by  $\hat{I}_R$ , and
3. a *two-way* intensity field represented  $\hat{I}$ .

The purpose of the optics model is the evaluation of the *two-way* intensity field, which represents the coupling to the flow code. The *initial* and *return* intensities are, in a sense, internal field variables used in the calculation. At convergence, these two internal fields have the same value. Specifically, the algorithm computes a *return* intensity field and ultimately a *two-way* intensity field based on the current gain field and an *initial* intensity field. The latter is computed by a relaxation method from the previous invocation of the routine. Thus, we suggest the abstract description

$$u_p^{n+1} = \mathcal{H}(u_f, u_p^n, \beta). \quad (91)$$

At convergence  $u_p^{n+1} = u_p^n$ . As a result, we use the following semi-explicit form for Eq (86)

$$\mathcal{R}_p(u_f, u_p, \beta) = u_p - \mathcal{H}(u_f, u_p, \beta). \quad (92)$$

With this structure the coupled sensitivity Eq (87) can be written as:

$$\begin{bmatrix} \frac{\partial \mathcal{R}_f}{\partial u_f} & \frac{\partial \mathcal{R}_f}{\partial u_p} \\ -\frac{\partial \mathcal{H}}{\partial u_f} & \left[ \mathcal{I}_p - \frac{\partial \mathcal{H}}{\partial u_p} \right] \end{bmatrix} \cdot \begin{pmatrix} \frac{\partial u_f}{\partial \beta} \\ \frac{\partial u_p}{\partial \beta} \end{pmatrix} = \begin{pmatrix} -\frac{\partial \mathcal{R}_f}{\partial \beta} \\ \frac{\partial \mathcal{H}}{\partial \beta} \end{pmatrix}, \quad (93)$$

where  $\mathcal{I}_p$  is the identity operator. Equation (93) is the approach that we have taken in the COIL sensitivity studies.

The present study assumes that the design parameter of interest (generically,  $\beta$ ) does not explicitly appear in the power-extraction module. As a practical matter this rules out cases where, for example, the geometry in the optical cavity depends on  $\beta$ . Mathematically, this assumption means that the function  $\mathcal{H}$  in Eq (92) does not depend explicitly on  $\beta$ . Our plan is to use an iterative

approach to solve the coupled linear system (93). For example, a Gauss-Seidel type implementation would be of the form

$$\left( \frac{\partial \mathcal{R}_f}{\partial u_f} \right) S_f^{n+1} = -\frac{\partial \mathcal{R}_f}{\partial \beta} - \frac{\partial \mathcal{R}_f}{\partial u_p} S_p^n \quad (94)$$

$$S_p^{n+1} = \frac{\partial \mathcal{H}}{\partial u_f} S_f^{n+1} + \frac{\partial \mathcal{H}}{\partial u_p} S_p^n, \quad (95)$$

where we have used  $S_f$  and  $S_p$  to denote the flow and laser-intensity state sensitivities, respectively. That is,

$$S_f \equiv \frac{\partial u_f}{\partial \beta}, \text{ and}$$

$$S_p \equiv \frac{\partial u_p}{\partial \beta}.$$

Equation (94) is solved using a modification of AeroSoft's SENSE code that includes the term  $\frac{\partial \mathcal{R}_f}{\partial u_p} S_p^n$ . This accounts for the effect of variations of the laser intensity on the source terms in the flow equations. The term is calculated pointwise throughout the flow field using the most recently calculated intensity sensitivity, which is communicated to the flow-sensitivity code in the same way the intensity field is communicated to the flow-solver.

The intensity sensitivity,  $S_p$ , is updated as shown in Eq (95). The procedure for implementing this calculation is realized in the new sensitivity module based in the geometric ray-tracing algorithm. At an abstract level the dependence of the map  $\mathcal{H}$  on the flow field is naturally decomposed into two stages: a map from the flow field to the gain field; followed by a map from the gain field to the intensity field. In symbols

$$\mathcal{H}(u_f, u_p) = \mathcal{M}(\mathcal{N}(u_f), u_p), \quad (96)$$

where  $\mathcal{N}$  maps the flow-field, pointwise, to the associated gain field, and  $\mathcal{M}$  maps the gain field, intensity field pair to the associated intensity field. The required Frechét derivative is calculated via the chain-rule

$$\frac{\partial \mathcal{H}}{\partial u_f} = \frac{\partial \mathcal{M}}{\partial u_g} \frac{\partial \mathcal{N}}{\partial u_f}, \quad (97)$$

where  $u_g$  represents the gain field.

The  $\mathcal{N}$  map, operating pointwise, is an ordinary function of the flow-field data. Flow-field sensitivity information, such as the sensitivity of the various number densities to the design parameter, is available from the modified SENSE code. Given the functional form for the gain and the chain rule we can explicitly calculate the gain-field sensitivity. The intermediate matrix in this chain-rule is our calculation of the term  $\frac{\partial \mathcal{N}}{\partial u_f}$ . As in the coupled flow-power calculation various grid systems must be reconciled. Eventually, we compute an array of gain sensitivities that represents the sensitivity of the gain field to changes in the design parameter.

The function  $\mathcal{M}$  maps the gain field and *initial* intensity field to a new intensity field as implemented in the ray-tracing code. This is represented symbolically in Eq (92). Our initial implementation of the Gauss-Seidel iteration for the sensitivity calculation will follow the approach used in the coupled flow solution. Specifically, the  $u_p$  variable in Eq (91) is identified with the *initial* intensity field, which at convergence, agrees with the *return* intensity field. The symbolic notation given by Eq (91) is implemented in the ray-tracing algorithm.

The implementation of the second Gauss-Seidel update, *i.e.*, Eq (95), proceeds as follows. The sensitivity of the *initial/return* intensity field will be computed as

$$\frac{\partial I_R(J)}{\partial \beta} = \frac{\partial I_O(J)}{\partial \beta} (R_1 R_2)^m e^s \prod_{p=1}^m (1 - \delta_p) + I_0(J) (R_1 R_2)^m \frac{\partial}{\partial \beta} (e^s) \prod_{p=1}^m (1 - \delta_p). \quad (98)$$

The  $\beta$ -parameter enters here through the gain field variable  $\bar{\alpha}_p$  which is computed from the stored gain field. The required expression is

$$\frac{\partial (e^s)}{\partial \beta} = 2 L_g e^s \sum_{p=1}^m \lambda \frac{\partial \bar{\alpha}_p}{\partial \beta}. \quad (99)$$

Since  $\bar{\alpha}_p$  is an average of the gain along a particular ray through the gain field, it is a linear function of the gain field array. Its  $\beta$ -derivative is this same linear function of the entries in the gain-sensitivity array. The  $\beta$ -derivative of the *two-way* intensity field is then computed. The *two-way* intensity sensitivity is communicated back to the flow sensitivity code SENSE in the same way that the *two-way* intensity field is communicated to the flow solver.

## 9.1 Power-On Sensitivity Analysis

In order to test this procedure, we will run the simple test problem with the newly-developed COIL sensitivity package that includes the optics resonator sensitivities. In this case the laser is turned on and the intensity sensitivities are utilized in the source terms. Again, the design variable is the free-stream density of  $O_2(^1\Delta)$  in the lower stream. Figure 30(a) shows the gain distribution along the  $j = 10$  gridline. Past the start of the aperture, the gain is dramatically reduced through interaction with the lasing source terms. Figure 30(b) shows the gain sensitivity distribution along the  $j = 10$  gridline for the SENSE code with the coupled optics sensitivity module, and for a central difference calculation using GASP v4. The CSEM results are in very good agreement with central difference. The power sensitivity predicted by the CSEM method was  $P' = 1.01948 \times 10^7$  while that predicted by the central difference procedure was  $P' = 1.01285 \times 10^7$ . This represents an error of approximately 0.65%. Figure 31 shows the power sensitivity convergence history for the global scheme.

# 10 Paraxial Wave Model

Commonly, laser optics are modeled by a ray-tracing process, wherein the path of a photon through the optical cavity is described as a sequence of straight line segments with specular reflection at the bounding mirrors. An excellent presentation of the ray tracing methodology is given in [20], while application to a COIL configuration is described in [2].

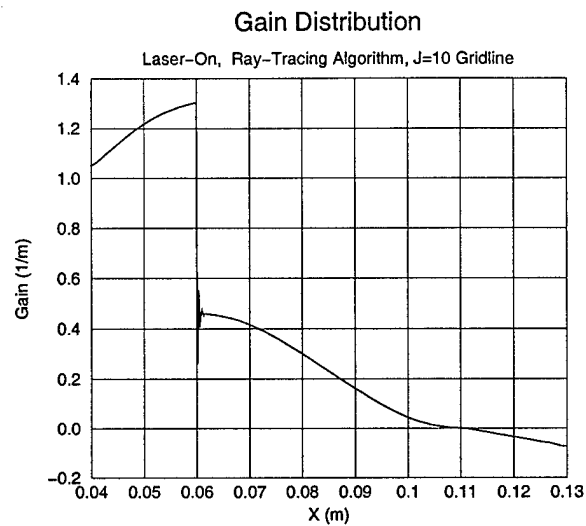
While it is convenient, a particle photon description does not completely suit our needs. Certain physical effects, such as diffusion (spreading of the light beam) and diffraction (the effects of non-uniform light speed) are not well described by these models. Moreover, for design purposes it is helpful to know the sensitivity of the laser performance to certain design parameters. Our goals in this effort were to develop continuum models describing laser intensity in the COIL optical cavity and to develop tools for calculating sensitivity to design parameters.

In the present effort the optical behavior is modeled in terms of a electric field (wave) propagating through the optical cavity (see Figure 32). We model the electric field as a *transverse electromagnetic wave* (TEM), essentially a perturbation of a plane wave with normal (almost) aligned with the optical ( $z$ ) axis of the optical cavity.

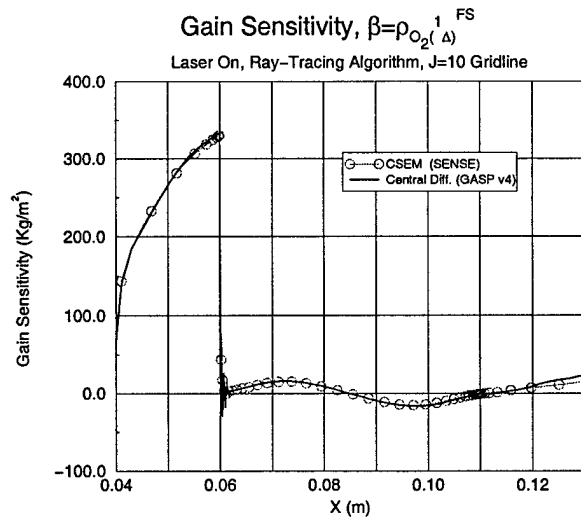
## 10.1 Paraxial Wave Optics and Gaussian Beams

As we are interested in the behavior of laser intensity throughout the optical cavity, we consider the physical system shown in Figure 33.

The schematic shown in Figure 33 depicts two mirrors separated by a distance  $D$ . The lower mirror ( $M_1$ ) is flat, while the upper mirror ( $M_2$ ) is spherical. Figure 33 also illustrates the region in which atomic gain is active. In the work presented here, we specify a real-valued atomic gain



(a) Gain profile ( $1/m$ ),  $j = 10$  gridline.



(b) Gain sensitivity,  $j = 10$  gridline.

Figure 30: Gain and gain sensitivity profiles for the simple test case with power on.

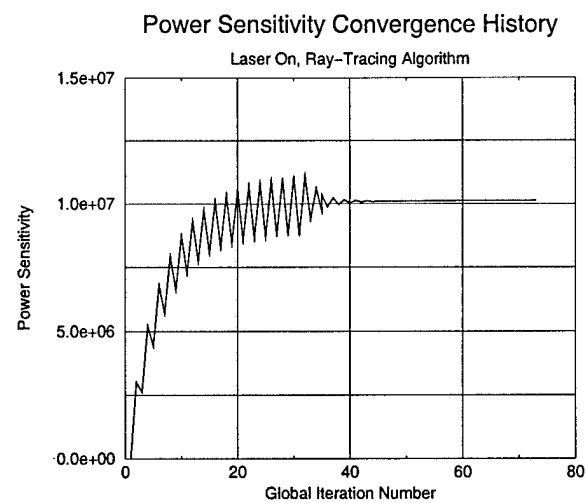


Figure 31: Simple test case power sensitivity convergence.

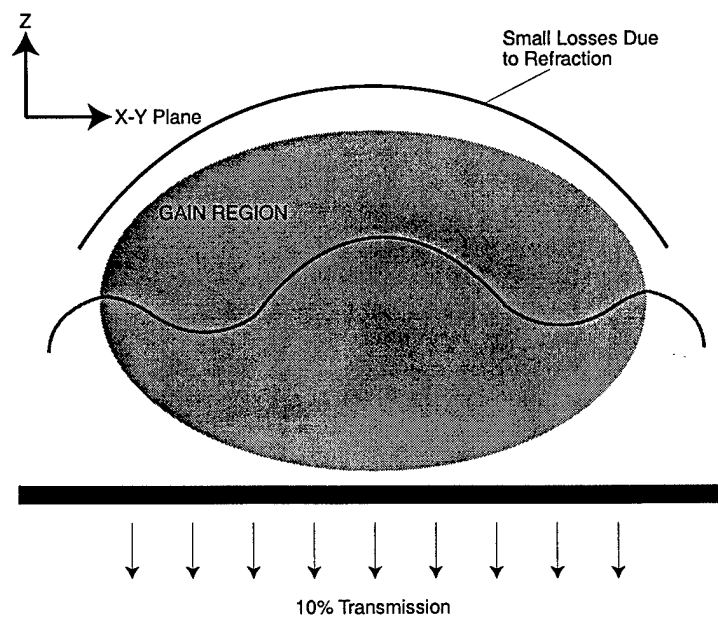


Figure 32: Propagating Wave Approach

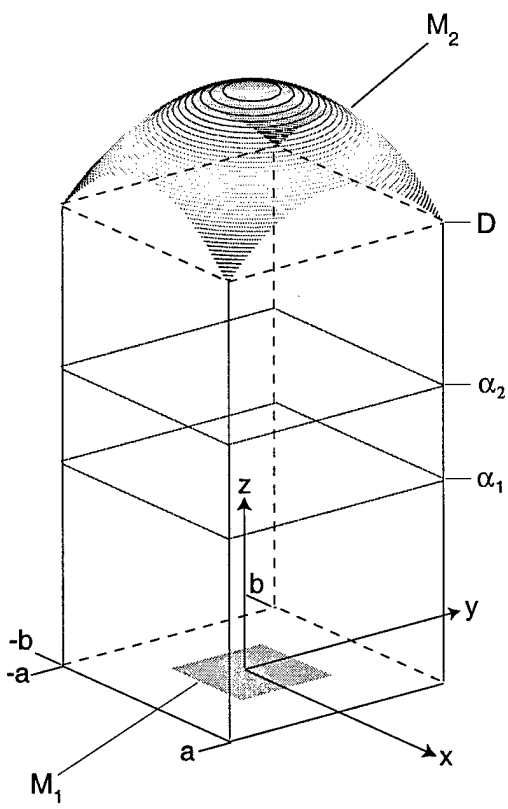


Figure 33: Optical Cavity Geometry

function  $\alpha(x, y, z)$  as

$$\alpha(x, y, z) = \begin{cases} f(x, y) & \text{if } z \in [\alpha_1, \alpha_2]; \\ 0, & \text{otherwise.} \end{cases} \quad (100)$$

In Section 10.5 we exploit the fact that the gain is a piecewise constant function of  $z$ .

The behavior of transverse electromagnetic waves is modeled by the paraxial wave equation

$$\frac{\partial u}{\partial z} = -\frac{i}{2k} \left( \frac{\partial^2 u}{\partial x^2} + \frac{\partial^2 u}{\partial y^2} \right) + [\alpha - ik(n-1)]u. \quad (101)$$

In equation (101),  $u(x, y, z)$  denotes the complex amplitude of the electric field; the net atomic gain is described by  $\alpha(x, y, z)$ ; and, the index of refraction in the optical cavity is given by  $n(x, y, z)$ . Finally, the constant  $k$  is the wave number:  $k > 0$  denotes a wave propagating toward increasing values of  $z$ , and conversely a negative value of  $k$  represents a wave moving toward decreasing values of  $z$ . The intensity  $I(x, y, z)$  is related to the modulus of the electric field according to  $I = |u|^2$ .

The partial differential equation given by (101) provides a convenient means of determining the electric field inside the optical cavity. At the bounding mirrors, however, a first principles treatment requires describing the evolution of the electric field on the mirror surface, as well as boundary conditions relating the interior and surface electric fields.

Fortunately, in most quantum electronic applications the optical beam can be approximated as a transverse electromagnetic wave and represented as a combination of Hermite-Gaussian beams. Reflection of these Hermite-Gaussian beams by spherical mirrors (as well as other common optical elements) is well understood. Excellent presentations of Hermite-Gaussian beam theory are given in [18], [20], and [21]. For the sake of completeness, we briefly describe the topics of the theory that we utilize in this work.

The Hermite-Gaussian modes comprise a family of solutions to the two-dimensional paraxial wave equation in free space. The Hermite-Gaussian mode  $\phi_n(x, z)$  of order  $n$  is of the form

$$\phi_n(x, z) = \left( \frac{2}{\pi} \right)^{\frac{1}{4}} \left( \frac{1}{2^n n! w_0} \right)^{\frac{1}{2}} \left( \frac{q_0}{q(z)} \right)^{\frac{1}{2}} \left[ \frac{q_0 q^*(z)}{q_0^* q(z)} \right]^{\frac{n}{2}} H_n \left( \frac{\sqrt{2}x}{w(z)} \right) \exp \left[ -i \frac{kx^2}{2q(z)} \right]. \quad (102)$$

In Equation (102),  $H_n$  is the Hermite polynomial of order  $n$ . The quantity  $w(z)$  is referred to as the spot size of the beam, and is a measure of the width of a Gaussian beam. The expression for  $w(z)$  is of the form

$$w(z) = w_0 \sqrt{1 + \left( \frac{z\lambda}{\pi w_0^2} \right)^2}, \quad (103)$$

where  $w_0$  is the minimum spot size, and  $\lambda$  is the wavelength of the light. The quantity  $q(z)$  in (102) is referred to as the complex beam parameter, and its evolution is given by:

$$q(z) = z + \frac{i\pi w_0^2}{\lambda} = z + q_0. \quad (104)$$

As can be seen from (102), (103), and (104), the Hermite-Gaussian modes are completely determined once values for  $w_0$  and  $\lambda$  are specified.

The Hermite-Gaussian modes given by (102) have several useful properties. The modes  $\phi_n(x, z)$  obey an orthonormality relation

$$\int_{-\infty}^{\infty} \phi_n^*(x, z) \phi_m(x, z) dx = \delta_{nm},$$

where  $\delta_{nm}$  is the Kronecker delta. Moreover, the Hermite-Gaussian modes provide a complete set of basis functions characterized by the single complex parameter  $w_0$  [19]. As a result, they can be used to expand a solution  $u(x, y, z)$  of the free space paraxial wave equation as

$$u(x, y, z) = \sum_n \sum_m c_{nm}(z) \phi_n(x, z) \phi_m(y, z). \quad (105)$$

Multiplying both sides of (105) by  $\phi_n^*(x, z)\phi_m^*(y, z)$  and integrating over the transverse plane yields

$$c_{nm}(z) = \int_{-\infty}^{\infty} \int_{-\infty}^{\infty} u(x, y, z)\phi_n^*(x, z)\phi_m^*(y, z)dx dy. \quad (106)$$

Thus, a solution  $u(x, y, z)$  of the paraxial wave equation, characterized by  $w_0$ , can be expanded as in (105) where the coefficients used in the expansion are given by (106). If  $u(x, y, z)$  is a solution to the free-space paraxial wave equation, then the coefficients  $c_{nm}(z)$  will be independent of  $z$ .

The spherical mirror transforms the complex beam parameter  $q(z)$  used in the construction of the Hermite-Gaussian modes. The transformation law for a spherical mirror is given by

$$\frac{1}{q_2} = \frac{1}{q_1} - \frac{2}{r}, \quad (107)$$

where  $r$  is the mirror radius. In (107), the quantity  $q_1$  is the value of  $q(z)$  of the wave incident on the curved mirror, while the value of the complex beam parameter for the wave reflecting from the curved mirror is given by  $q_2$ .

The influence of the spherical mirror can be obtained by expanding a solution of the paraxial wave equation in terms of the Hermite-Gaussian modes at the curved mirror, transforming the modes, and then reconstructing the wave consisting of the transformed modes. In the following section, we utilize the properties of Gaussian beams to formulate a continuum model describing the electric field inside the optical cavity of the COIL. More generally, the effect of other optical elements on Hermite-Gaussian beams can be described by so-called *ABCD* transformation rules [18, see Chapter 20] applied to the complex beam parameter,  $q$ .

## 10.2 Optical Cavity Model

We are interested in laser intensity after one round-trip through the optical cavity. Thus, we specify an initial electromagnetic wave profile at  $z = 0$ , moving upwards from the outcoupling mirror ( $M_1$ , see Figure 33). The solution is propagated through increasing  $z$  until the wave reaches the spherical mirror,  $M_2$ . At the spherical mirror, the propagating wave is reflected, and the wave propagates towards decreasing values of  $z$  until it arrives at the horizontal mirror again. Upon arriving at the outcoupling mirror, a portion of the wave energy is extracted due to energy transmission through the mirror. In the RADICL device (a research and development version of COIL, [17, see Chapter 1]) approximately ten percent of the wave energy is transmitted through the outcoupling mirror, while roughly ninety percent of the energy is reflected back into the optical cavity.

We are now in a position to describe a continuum model for the electric field inside the optical cavity. Since we start with an initial condition at  $z = 0$  and propagate the solution toward the spherical mirror, the first part of our model describes wave propagation toward increasing values of  $z$ .

### 10.2.1 Propagation Toward Increasing $z$

The first part of our model describes wave propagation from  $M_1$  to  $M_2$ , toward increasing values of  $z$ . As a result, wave behavior is modeled by

$$\frac{\partial u}{\partial z} = -\frac{i}{2k} \left( \frac{\partial^2 u}{\partial x^2} + \frac{\partial^2 u}{\partial y^2} \right) + [\alpha - ik(n-1)]u, \quad (k > 0). \quad (108)$$

An initial condition is specified at the horizontal mirror. Care must be taken in specifying the initial condition. Our aim is to utilize the properties of Gaussian-beam reflection at the spherical mirror. Recall that the Hermite-Gaussian basis functions presented in the previous section depend on the beam spot size  $w(z)$ . In this work, we specify that the minimum spot size  $w_0$  is located at the outcoupling mirror initially. We use what is known as the 99% rule to initially specify  $w_0$  at

the flat mirror  $M_1$ . This rule is used as a design criterion in determining proper aperture size. An aperture of half-length  $a_r$  will pass just over 99% of the energy of a Gaussian beam if  $a_r$  satisfies

$$a_r = \frac{\pi}{2}w, \quad (109)$$

where  $w$  is the spot size at the aperture.

The relationship given in (109) is the 99% rule. We utilize (109) by specifying the half-length of the outcoupling mirror  $M_1$ , and then determine  $w_0$  according to

$$w_0 = \frac{2M_r}{\pi}, \quad (110)$$

where  $M_r$  is the half-length of the flat mirror. We then specify an initial condition of the form

$$u(x, y, 0) = u_0(x, y, w_0), \quad (111)$$

where  $w_0$  is the spot size resulting from the 99% rule. In the event that the half-lengths of the flat mirror are unequal in the  $x$  and  $y$  directions, we utilize (110) and specify the spot sizes in the  $x$  and  $y$  directions separately.

While, in principle the wave diffuses to great distances in the transverse directions, in practice the energy of the propagating wave is confined near the optical axis. Thus, we specify  $a$  to be several multiples of the half-length of  $M_1$  in the  $x$  direction, and  $b$  to be several multiples of the half-length of  $M_1$  in the  $y$  direction. The outcoupling mirror is then located in the *interior* of the region  $[-a, a] \times [-b, b]$ . Choosing  $a$  and  $b$  sufficiently large allows us to specify that the electric field remain at zero along the transverse boundary. In addition, due to the geometry of the COIL apparatus, we assume that the electric field is symmetric about  $y = 0$ . The resulting boundary conditions we prescribe are of the form

$$u(-a, y, z) = u(a, y, z) = u(x, b, z) = 0, \quad (112)$$

$$\text{and } \frac{\partial u(x, 0, z)}{\partial y} = 0. \quad (113)$$

The partial differential equation model above is applied for wave propagation from the horizontal mirror to  $z = D$ .

### 10.2.2 Mirror Transformation

Upon arriving at  $z = D$ , the propagating wave encounters the spherical mirror. Recall that a spherical mirror transforms the complex beam parameter  $q(z)$  used in the construction of the Hermite-Gaussian modes. In order to incorporate the appropriate transformation into our model, we expand the solution  $u(x, y, D)$  in terms of the Hermite-Gaussian basis functions. That is, we expand  $u(x, y, D)$  as

$$u(x, y, D) = \sum_n \sum_m c_{nm} \phi_n(x, D) \phi_m(y, D), \quad (114)$$

where  $\phi_n$  and  $\phi_m$  are the Hermite-Gaussian modes given by (102, 103, 104). Recall that the coefficients used in the expansion are computed according to (106), *viz.* :

$$c_{nm} = \int_{-\infty}^{\infty} \int_{-\infty}^{\infty} u(x, y, D) \phi_n^*(x, D) \phi_m^*(y, D) dx dy.$$

If we denote the value of the complex beam parameter at  $z = D$  by  $q(D) = q_1$ , then, by utilizing (107), the transformed beam parameter  $q_2$  due to reflection is given by

$$\frac{1}{q_2} = \frac{1}{q_1} - \frac{2}{r}, \quad (115)$$

where  $r$  is the radius of the spherical mirror,  $M_2$ . The transformed Hermite-Gaussian modes are of the form

$$\tilde{\phi}_n(x, z) = \left(\frac{2}{\pi}\right)^{\frac{1}{4}} \left(\frac{1}{2^n n! w_0}\right)^{\frac{1}{2}} \left(\frac{q_0}{q_2}\right)^{\frac{1}{2}} \left[\frac{q_0 q_2^*}{q_0^* q_2}\right]^{\frac{n}{2}} H_n\left(\frac{\sqrt{2}x}{w_2(z)}\right) \exp\left[-i\frac{kx^2}{2q_2}\right]. \quad (116)$$

Recombining the transformed Hermite-Gaussian modes yields the transformed solution  $\tilde{u}(x, y, D)$  due to reflection. The resulting expression for  $\tilde{u}(x, y, D)$  is of the form

$$\tilde{u}(x, y, D) = \sum_n \sum_m c_{nm} \tilde{\phi}_n(x, D) \tilde{\phi}_m(y, D). \quad (117)$$

### 10.2.3 Propagation Toward Decreasing $z$

After reflection at  $z = D$ , the transformed wave then propagates toward decreasing values of  $z$ . Thus, wave propagation after reflection is described by the downward paraxial wave equation of the form

$$\frac{\partial g}{\partial z} = \frac{i}{2|k|} \left( \frac{\partial^2 g}{\partial x^2} + \frac{\partial^2 g}{\partial y^2} \right) + [\alpha(x, y, z) + i|k|(n - 1)]g, \quad (k < 0). \quad (118)$$

The transformed solution at  $z = D$  is used as the initial data for (118). That is, we specify that

$$g(x, y, D) = \tilde{u}(x, y, D). \quad (119)$$

As in the case of upward propagation, we require that the electric field remain at zero along the transverse boundary. Moreover, we assume that the electric field is symmetric about  $y = 0$  and impose the boundary conditions (112), (113).

### 10.2.4 Energy Extraction

After reflecting from the spherical mirror, the wave propagates through decreasing  $z$  values until it arrives back at the outcoupling mirror  $M_1$ . The modulus of the electric field incident on the outcoupling mirror is given by  $|g(x, y, 0)|$ . In order to completely describe wave behavior for one round-trip through the optical cavity, we now model the extraction/reflection of wave energy that occurs at the outcoupling mirror. As noted above, in the RADICL device approximately ten percent of the wave energy is transmitted through the outcoupling mirror, so that roughly ninety percent of the wave energy is reflected from the outcoupling mirror back into the optical cavity.

Recall that wave reflection from a spherical mirror transforms the complex beam parameter  $q(z)$  used in the specification of the Hermite-Gaussian modes. As can be seen from (107), the parameter  $q(z)$  is unchanged in the case of reflection from a mirror with infinite radius of curvature. As a result, to determine the wave profile after one round-trip through the optical cavity, we simply decompose  $g(x, y, 0)$  into two parts. The first part is that portion of  $g(x, y, 0)$  that is incident on the outcoupling mirror. The second part is the portion of  $g(x, y, 0)$  that misses the flat mirror.

To incorporate the transmission of energy through the outcoupling mirror, define the energy  $\mathcal{E}_u(z)$  associated with a wave profile  $u(x, y, z)$  according to

$$\mathcal{E}_u(z) = \int_{-b}^b \int_{-a}^a |u(x, y, z)|^2 dx dy. \quad (120)$$

Define the function  $g_M(x, y, 0)$  by

$$g_M(x, y, 0) = \begin{cases} g(x, y, 0) & \text{if } (x, y) \in \mathcal{D}(M_1); \\ 0, & \text{otherwise,} \end{cases}$$

where  $\mathcal{D}(M_1)$  is the subset of the region  $[-a, a] \times [0, b]$  occupied by the flat mirror. In a similar fashion, define  $g_R(x, y, 0)$  according to

$$g_R(x, y, 0) = \begin{cases} g(x, y, 0) & \text{if } (x, y) \notin \mathcal{D}(M_1); \\ 0, & \text{otherwise.} \end{cases}$$

For the sake of simplicity, we assume that energy not incident on the outcoupling mirror is absorbed by the optical cavity wall. As a result, the energy associated with  $g_R(x, y)$  is completely absorbed, and none of its energy is reflected back into the optical cavity.

The requirement that ten percent of the energy of the wave profile incident on  $M_1$  is transmitted through the mirror results in the specification that

$$\int_{-\infty}^{\infty} \int_{-\infty}^{\infty} |u_R(x, y, 0)|^2 dx dy = 0.9 \int_{-\infty}^{\infty} \int_{-\infty}^{\infty} |g_M(x, y, 0)|^2 dx dy,$$

where  $u_R(x, y, 0)$  is the wave profile after one round-trip through the optical cavity. The 90% reflection requirement is applied pointwise, so that the round-trip solution  $u_R(x, y, 0)$  is found according to

$$u_R(x, y, 0) = \sqrt{0.9} g_M(x, y, 0).$$

### 10.3 Numerical Implementation

In order to obtain numerical solutions to the initial boundary value problem presented in the previous section, we construct a uniform finite difference grid on the physical domain represented in Figure 33. The step-size in the  $z$  direction is denoted by  $\Delta z$ . The step-size in the  $x$  and  $y$  directions is denoted by  $h$ . Evaluation points in the  $x$  direction are in the interval  $[-a, a]$ . Similarly,  $y$  values are in the interval  $[0, b]$ .

#### 10.3.1 Propagation Toward Increasing $z$

As we are first interested in propagation toward increasing values of  $z$ , our finite difference scheme for upward propagation must approximate the initial boundary value problem given by (108), (111)-(113). To this end, the first order derivative in the  $z$  direction is approximated as

$$\frac{\partial}{\partial z} u(\cdot, \cdot, z) \approx \frac{u(\cdot, \cdot, z + \Delta z) - u(\cdot, \cdot, z)}{\Delta z}. \quad (121)$$

The second order derivatives in the transverse directions are approximated by

$$\frac{\partial^2}{\partial x^2} u(x, \cdot, \cdot) \approx \frac{u(x - h, \cdot, \cdot) - 2u(x, \cdot, \cdot) + u(x + h, \cdot, \cdot)}{h^2}, \text{ and} \quad (122)$$

$$\frac{\partial^2}{\partial y^2} u(\cdot, y, \cdot) \approx \frac{u(\cdot, y - h, \cdot) - 2u(\cdot, y, \cdot) + u(\cdot, y + h, \cdot)}{h^2}. \quad (123)$$

In order to simplify the resulting finite difference approximation, we introduce the quantities  $\nu$  and  $c_{i,j}^n$  given by

$$\nu = \frac{i\Delta z}{2kh^2}, \text{ and} \quad (124)$$

$$c_{i,j}^n = \Delta z (\alpha_{i,j}^n - i k (n_{i,j} - 1)). \quad (125)$$

The resulting finite difference scheme we utilize at each evaluation point  $(x_i, y_j, z_n)$  is a Crank-Nicholson scheme of the form

$$\begin{aligned} [\nu u_{i-1,j}^{n+1} + \nu u_{i+1,j}^{n+1} + (2 - 4\nu - c_{i,j}^{n+1})u_{i,j}^{n+1}] + [\nu u_{i,j-1}^{n+1}] + [\nu u_{i,j+1}^{n+1}] = \\ [-\nu u_{i-1,j}^n - \nu u_{i+1,j}^n + (2 + 4\nu + c_{i,j}^n)u_{i,j}^n] - [\nu u_{i,j-1}^n] - [\nu u_{i,j+1}^n]. \end{aligned} \quad (126)$$

Convergence properties of (126) are given in [14].

The symmetry condition given by (113) is incorporated into (126) in the case of  $j = 0$ . That is, for  $j = 0$ , the scheme given by (126) becomes

$$\begin{aligned} [\nu u_{i-1,0}^{n+1} + \nu u_{i+1,0}^{n+1} + (2 - 4\nu - c_{i,0}^{n+1})u_{i,0}^{n+1}] + 2[\nu u_{i,1}^{n+1}] = \\ [-\nu u_{i-1,0}^n - \nu u_{i+1,0}^n + (2 + 4\nu + c_{i,0}^n)u_{i,0}^n] - 2[\nu u_{i,1}^n]. \end{aligned} \quad (127)$$

Iterations for upward propagation are done using (126) and (127). The iterations are started using the initial condition  $u_0(x_i, y_j, 0)$ .

### 10.3.2 Mirror Transformation Implementation

Utilizing the Crank-Nicholson scheme of the previous section, one obtains a numerical solution to the initial boundary value problem describing upward wave propagation. At an axial distance of  $z = D$ , the propagating wave encounters the spherical mirror  $M_2$ . Thus, we now transform the solution at  $z = D$  in order to incorporate the properties of Gaussian beam reflection into the numerical approximation. That is, we expand the solution  $u(x_i, y_j, D)$  in terms of the Hermite-Gaussian modes as

$$u(x_i, y_j, D) = \sum_{n=0}^{N_m} \sum_{m=0}^{N_m} c_{nm} \phi_n(x_i, D) \phi_m(y_j, D), \quad (128)$$

where  $N_m$  is the order of the highest order mode used in the expansion.

In order to utilize the orthonormality properties of the Hermite-Gaussian modes, we reflect the numerical solution about  $y = 0$  to get a numerical solution with support on the rectangle  $[-a, a] \times [-b, b]$ . The expansion coefficients  $c_{nm}$  are then found according to

$$c_{nm} = \int_{-b}^b \int_{-a}^a u(x, y, D) \phi_n^*(x, D) \phi_m^*(y, D) dx dy. \quad (129)$$

The integral in (129) is approximated via a double Riemann sum.

Having obtained the coefficients  $c_{nm}$  needed in the expansion, the Hermite-Gaussian modes are transformed according to Equation (116). Recombining the transformed Hermite-Gaussian modes yields a transformed numerical solution  $\tilde{u}(x_i, y_j, D)$  of the form

$$\tilde{u}(x_i, y_j, D) = \sum_{n=0}^{N_m} \sum_{m=0}^{N_m} c_{nm} \tilde{\phi}_n(x_i, D) \tilde{\phi}_m(y_j, D), \quad (130)$$

where  $\tilde{\phi}_n$  is the transformed mode of order  $n$ .

### 10.3.3 Propagation Toward Decreasing $z$

We now shift our attention to the propagation of the reflected wave back to the outcoupling mirror. The numerical scheme needed for downward propagation is easily obtained by reversing the sign of  $k$ , and results in a Crank-Nicholson scheme of the form

$$\begin{aligned} [-\nu g_{i-1,j}^{n+1} + \nu g_{i+1,j}^{n+1} + (2 + 4\nu - c_{i,j}^{n+1})g_{i,j}^{n+1}] - [\nu g_{i,j-1}^{n+1}] - [\nu g_{i,j+1}^{n+1}] = \\ [\nu g_{i-1,j}^n + \nu g_{i+1,j}^n + (2 - 4\nu + c_{i,j}^n)g_{i,j}^n] + [\nu g_{i,j-1}^n] + [\nu g_{i,j+1}^n]. \end{aligned} \quad (131)$$

Convergence properties of (131) are discussed in [14].

As before, the symmetry condition specified by (113) is incorporated into (131) for the case of  $j = 0$ . That is, in the case of  $j = 0$ , (131) becomes

$$\begin{aligned} [-\nu g_{i-1,0}^{n+1} + \nu g_{i+1,0}^{n+1} + (2 + 4\nu - c_{i,0}^{n+1})g_{i,0}^{n+1}] - 2[\nu g_{i,1}^{n+1}] = \\ [\nu g_{i-1,0}^n + \nu g_{i+1,0}^n + (2 - 4\nu + c_{i,0}^n)g_{i,0}^n] + 2[\nu g_{i,1}^n]. \end{aligned} \quad (132)$$

The remaining iterations are done with (131) and (132). The transformed numerical solution  $\tilde{u}(x_i, y_j, D)$  due to reflection is used as initial data.

### 10.3.4 Energy Extraction Implementation

In order to obtain the wave profile after one round-trip through the optical cavity, we decompose  $g(x_i, y_j, 0)$  into two parts, as described in Section 10.2.4. The round-trip solution  $u_R(x_i, y_j, 0)$  is then found according to

$$u_R(x_i, y_j, 0) = \sqrt{0.9} g_M(x_i, y_j, 0), \quad (133)$$

where  $g_M(x_i, y_j, 0)$  is that portion of  $g(x_i, y_j, 0)$  incident on the flat mirror.

### 10.3.5 Average Two-Way Intensity

Source terms in the reacting flow model require an intensity field in the optical cavity. Since the flow model is based on a *unit-cell* approximation, it is appropriate to supply an intensity field that is averaged (in the  $z$  direction). For this purpose we select a number of  $z$ -planes and compute the average two-way intensity field as:

$$I_{\text{avg}}(x_i, y_j) = \frac{1}{N_p} \left( \sum_{l=1}^{N_p} |u_{i,j}^{k(l)}|^2 + |g_{i,j}^{k(l)}|^2 \right), \quad (134)$$

where  $\{k(l) \mid l = 1, \dots, N_p\}$  is the index set labelling the  $z$  planes, and  $u$  ( $g$ ) is the upward (*resp.* downward) electric field solution.

## 10.4 The Coupled Model

As previously noted, analyses codes for continuous wave chemical lasers can be viewed as coupled fluid mechanics and laser power extraction codes. In the present study we have used AeroSoft's *GASPv4* code to solve for the flow field ( $u_f$ ), given the *average two-way intensity* ( $u_i$ ) in the optical cavity. The calculations described in Section 10.3 were implemented in a C++ code so that an initial electric field at the flat outcoupling mirror was propagated one round-trip through the optical cavity. As part of this calculation we store a new *average two-way intensity* in the optical cavity [see Equation (134)]. With a slight abuse of notation we write the system abstractly as:

$$u_i - \mathcal{H}_i(u_f, u_i) = 0, \quad (135)$$

$$\mathcal{R}_f(u_f, u_i) = 0 \quad (136)$$

In the COIL application the variable  $u_i$  is interpreted as a pair of fields: the initial electric field at the outcoupling mirror, and the average two-way intensity in the active gain region. The residual for the chemically reacting flow (136) depends on the latter of these fields.

### 10.4.1 Model Problem

In order to study solution procedures for coupled systems of the form (135, 136) we constructed a model problem based on one-dimensional gas dynamics with heat addition [12]. This model problem was also used to study sensitivity calculations for such coupled systems.

### 10.4.2 Numerical Results

Two numerical implementations of the coupled COIL system (135, 136) were studied. At AeroSoft Inc. calculations were based on the *GASPv4* reacting flow code coupled to a ray-tracing optics model described by Crowell [2].

The numerical studies at ICAM were based on *GASPv4* loosely coupled to our C++ implementation of the paraxial optics model. At the end of the effort there were unresolved issues in the coupled codes so that no converged results are available. Figure 34 shows a typical twoway intensity field after several iterations. It appears that the beam parameters used to define the Hermite-Gaussian beam family are not appropriate and attempts to tune these parameters have not yet been successful.

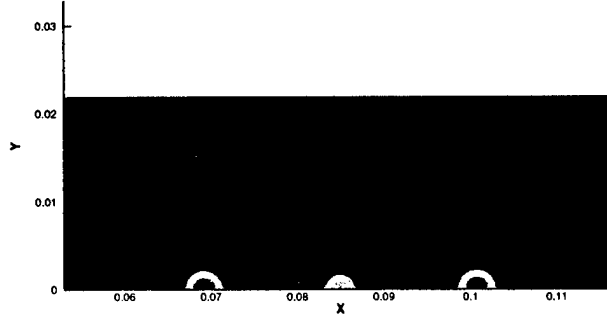


Figure 34: Two Way Intensity Field

## 10.5 Semigroup Formulation

From a mathematical point of view the partial differential equation system given by Equations (108, 111, 112, 113) is a *formal* model since it is not precisely stated what regularity an initial function must have or what regularity the solution will have. For example, given the solution at station  $\hat{z}$  does the energy expression (120) have a finite value? The analysis in Camphouse's PhD thesis [14] provides a framework and answers for these questions. Here we reproduce some of the material from Camphouse's work [14, see Chapter 3, 26 - 31]. The presentation is slightly altered in a way that suggests an alternative numerical treatment.

Consider the rectangular domain  $\Omega = [-a, a] \times [-b \times b]$  and let  $\mathcal{H} = L_2(\Omega)$ , the square integrable functions on the specified domain. Consider the upward wave model (108) with  $\alpha \equiv 0$  and  $n \equiv 1$  and define the operator  $A_0 : \mathcal{D}(A_0) \subset \mathcal{H} \mapsto \mathcal{H}$  by

$$A_0 u = -\frac{i}{2k} \left( \frac{\partial^2 u}{\partial x^2} + \frac{\partial^2 u}{\partial y^2} \right). \quad (137)$$

From [14, Theorem 3.1.1] we have The operator  $A_0$  defined by (137) generates a  $C_0$ -group of unitary operators  $\{\mathcal{S}_0(z) | -\infty < z < \infty\}$  on the space  $\mathcal{H}$ . In simple terms, for some fixed  $\hat{z}$ , the *group element*  $\mathcal{S}_0(\hat{z})$  is the solution operator that takes an initial electric field  $u_0(x, y)$  at  $z = 0$  and maps it to the (unique) solution to the boundary value problem (108, 111-113) at  $z = \hat{z}$ . The utility of the semigroup formulation is that it establishes that there is a unique solution to the boundary value problem and that the solution depends continuously in the initial data. Note that  $A_0$  models the free-space behavior of the paraxial waves.

If the gain is non-zero or the index of refraction is not unity then there is an additional term in the paraxial wave equation (108). For this purpose we require that the complex-valued function

$$g(x, y) = \alpha(x, y) - ik(n(x, y) - 1)$$

be in  $\mathcal{H}$  and define the operator  $A_1$  on  $\mathcal{D}(A_1) = \mathcal{D}(A_0) \subset \mathcal{H} \mapsto \mathcal{H}$  by

$$A_1 u = A_0 u + g u, \quad (138)$$

where, as expected,  $g u$  means pointwise multiplication. From [14, Theorem 3.1.2] we have The operator  $A_1$  defined by (138) generates a  $C_0$ -semigroup of operators  $\{\mathcal{S}_1(z) | 0 < z < \infty\}$  on  $\mathcal{H}$ . Moreover, the semigroup action is given by

$$\mathcal{S}_1(z)u = \exp(g z)\mathcal{S}_0(z)u. \quad (139)$$

The representation (139) means that we can find a solution to the problem with gain by first finding the solution with no gain and multiplying the resulting field pointwise by the value  $\exp[g(x, y) z]$ . This idea can be used as a basis for an alternative numerical formulation. The calculations we have in mind here are very similar to those reported in [19].

## **11 Personnel Supported**

Key personnel during the Phase-I effort are Dr. William Eppard, Dr. Andrew Godfrey and Dr. Michael Applebaum at Aerosoft and Dr. Eugene Cliff, Dr. John Burns and Dr. Chris Camphouse with ICAM at Virginia Tech.

## **12 Publications**

Reference [4] and [3] above.

## **13 Interactions/Transitions**

### **13.1 Participation/Presentations at Meetings**

Presentations at the 31<sup>st</sup> Plasmadynamics and Lasers Conference in Denver (19-22 of June 2000) and the 33<sup>rd</sup> AIAA Plasmadynamics and Lasers Conference in Maui (20-23 of May).

### **13.2 Transitions**

The improved modeling capabilities in GASP will provide an immediate impact on COIL analysis efforts at AFRL/DE. TRW and the Schafer Corp. are also using GASP for chemical laser analysis.

## **14 New Discoveries, Inventions, or Patent Disclosures**

None.

## **15 Honors/Awards**

None.

## References

- [1] R. C. Buggeln, S. Shamroth, A. I. Lampson, and P. G. Crowell. "Three-Dimensional (3-D) Navier-Stokes Analysis of the Mixing and Power Extraction in a Supersonic Chemical Oxygen Iodine Laser (COIL) With Transverse  $I_2$  Injection". AIAA Paper 94-2435, 25<sup>th</sup> *Plasmadynamics and Lasers Conference*, July, 1993.
- [2] P. G. Crowell. "A Stable Resonator Geometric Optics Model for Gain Saturation and Power Extraction in COIL Devices". Contract F29601-93-C-0028, CDRL A005, *Phillips Laboratory*, February, 1995.
- [3] W. M. Eppard, W. D. McGrory, and M. P. Applebaum. "The Effect of Water-Vapor Condensation and Surface Catalysis on COIL Performance". AIAA Paper 2002-2132, 33<sup>rd</sup> *AIAA Plasmadyanmics and Lasers Conference*, May 20-23, 2002.
- [4] W. M. Eppard, W. D. McGrory, A. G. Godfrey, E. M. Cliff, and J. T. Borggaard. "Recent Advances in Numerical Techniques for the Design and Analysis of COIL Systems". AIAA Paper 2000-2576, 31<sup>st</sup> *AIAA Plasmadyanmics and Lasers Conference*, June 19-22, 2000.
- [5] A. G. Godfrey and E. M. Cliff. "Direct Calculation of Aerodynamic Force Derivatives: A Sensitivity Equation Approach". AIAA Paper 98-0393, 36<sup>th</sup> *AIAA Aerospace Sciences Meeting and Exhibit*, January 12-15, 1998.
- [6] A. G. Godfrey, W. M. Eppard, and E. M. Cliff. "Using Sensitivity Equations for Chemically Reacting Flows". AIAA Paper 98-4805, 7<sup>th</sup> *AIAA/USAF/NASA/ISSMO Symposium on Multidisciplinary Analysis and Optimization*, September 2-4, 1998.
- [7] J. O. Hirschfelder, C. F. Curtiss, and R. B. Bird. **Molecular Theory of Gases and Liquid**. John Wiley and Sons, Library of Congress CCN 54-7621, 1954.
- [8] M. Hishida, N. Azami, K. Iwamoto, W. Masuda, H. Fujii, T. Atsuta, and M. Mura. "Flow and Optical Fields in a Supersonic Flow Chemical Oxygen-Iodine Laser". AIAA Paper 97-2391, 28<sup>th</sup> *Plasmadynamics and Lasers Conference*, June 23-25 1997.
- [9] T. J. Madden. "Personal Communication", January 2001.
- [10] W. Masuda, M. Satoh, and H. Yamada. "Effects of Water Vapor Condensation on Performance of Supersonic Flow Chemical Oxygen-Iodine Laser". *JSME Int. J.*, **39**(2):273, 1996.
- [11] J. T. Borggaard, E.M. Cliff and W. M. Eppard. "Working Notes on Sensitivity Modifications to stable.F" *ICAM Report 01-04-00*. VPI & SU, Blacksburg, VA, April, 2000.
- [12] J.T. Borggaard and E.M. Cliff. "Sensitivity Analysis for Chemical Laser Design: A Model Problem." *ICAM Report 01-06-00*. VPI & SU, Blacksburg, VA, June, 2000.
- [13] R. C. Buggeln and S. Shamroth and A. I. Lampson and P. G. Crowell. "Three-Dimensional (3-D) Navier-Stokes Analysis of the Mixing and Power Extraction in a Supersonic Chemical Oxygen Iodine Laser (COIL) With Transverse  $I_2$  Injection." *AIAA Paper 94-2435*. June 1994.
- [14] R. Chris Camphouse. *Modeling and Numerical Approximations of Optical Activity in the Chemical Oxygen-Iodine Laser*. PhD Thesis, Department of Mathematics, VPI & SU, Blacksburg, VA, July 2001.
- [15] P.G. Crowell. A Stable Resonator Geometric Optics Model for Gain Saturation and Power Extraction in COIL Devices, Phillips Laboratory, Contract F29601-93-C-0028, CDRL A005.
- [16] Andrew G. Godfrey, William M. Eppard, Eugene M. Cliff. "Using Sensitivity Equations for Chemically Reacting Flows." *AIAA Paper 98-4805* . 7th AIAA/USAF/NASA/ISSMO Symposium on Multidisciplinary Analysis and Optimization. St. Louis, Missouri. 2-4 September, 1998.

- [17] Timothy J. Madden. *Computational Fluid Dynamics Methodologies for Simulation of Chemical Oxygen-Iodine Laser Flowfields*. PhD Thesis, Department of Aeronautical and Astronautical Engineering, University of Illinois at Urbana-Champaign, 1997.
- [18] Anthony E. Siegman. *Lasers*. University Science Books, Mill Valley, CA, 1986.
- [19] Anthony E. Siegman, Edward A. Sziklas. "Mode Calculations in Unstable Resonators with Flowing Saturable Gain. 1: Hermite-Gaussian Expansion." *Applied Optics*. Vol. 13, No. 12. December, 1974.
- [20] Joseph T. Verdeyen. *Laser Electronics*, Third Edition, Prentice Hall, 1995.
- [21] Amnon Yariv. *Introduction to Optical Electronics*. Holt, Rinehart and Winston, 1976.